January 2009

Plume formation in strongly temperature-dependent viscosity fluids: Application to early Mars

Yun Ke
Washington University in St. Louis

Recommended Citation

Ke, Yun, "Plume formation in strongly temperature-dependent viscosity fluids: Application to early Mars" (2009). *All Theses and Dissertations (ETDs)*. 178.
https://openscholarship.wustl.edu/etd/178

WASHINGTON UNIVERSITY

Department of Earth and Planetary Sciences

Dissertation Examination Committee:
Slava Solomatov, Chair
Ramanath Cowsik
Frédéric Moynier
Douglas Wiens
Michael Wysession
Ernst Zinner

PLUME FORMATION IN STRONGLY TEMPERATURE-DEPENDENT VISCOSITY FLUIDS: APPLICATION TO EARLY MARS

by

Yun Ke

A dissertation presented to the
Graduate School of Arts and Sciences
of Washington University in
partial fulfillment of the
requirements for the degree
of Doctor of Philosophy

August 2009

Saint Louis, Missouri

Acknowledgements

This work that I present here would not be possible without the long term support from my advisor, Slava Solomatov. He has been a wonderful mentor with a lot of patience, encouragement, and support. Most importantly, he teaches me how to do research and how to write scientific paper. I would not be able to achieve these without his guidance.

In the last two years, I have been spending most of my time in the business school for my MBA degree. The intern experience that I had during that time was the first real job experience in my life. It makes me feel that doing research at school is way better than working in a company.

I would like to thank my wife, Zhen Liu, and my parents. My wife has supported me financially and mentally, especially in this last period of time. Although my parents do not understand what my research is about, they did not give me any pressure to find a job. My thanks are extended to my colleagues in the department, especially Chris Orth, Garrett Euler, David Heeszel, and Erica Emry. I have spent a wonderful time with them, and wish them great success in their research.

Contents

List of Figures

List of Tables

ABSTRACT OF THE DISSERTATION

Plume formation in strongly temperature-dependent viscosity fluids: Application to early Mars

by

Yun Ke

Doctor of Philosophy in Earth and Planetary Sciences

Washington University in St. Louis, 2009

Professor Slava Solomatov, Chairperson

One of the most prominent features of Mars is the hemispherical dichotomy. The Martian surface consists of a heavily cratered elevated southern hemisphere and a resurfaced depressed northern hemisphere. The dichotomy seems to have formed very early in the history of the planet. Another interesting feature is a remnant magnetization of the crust, which suggests that early Mars had a magnetic field. Investigation of the origin of these features provides insights into the early history of Mars as well as other terrestrial planets including Earth. We develop a hypothesis that the dichotomy is caused by an early transient superplume produced by a hot Martian core. At first glance, the superplume hypothesis seems unlikely because the number of plumes in typical fluids heated from below is very large and the plumes are relatively small. However, solid rocks are rather unusual fluids whose viscosity varies with temperature by many orders of magnitude. Plume formation in such fluids is a complex and poorly understood phenomena. Thus, we begin with a systematic two-dimensional numerical and theoretical investigation of plume formation in strongly temperature-dependent viscosity fluids. Then we extend both the numerical calculations and the theory to fully three-dimensional geometry. We find the conditions under which a single transient superplume forms. One of the most important conditions is the requirement that the core was at least several hundred degrees Kelvin hotter than the mantle. Geophysical data and theoretical models of core formation suggest that this is likely to be the case. We find that the superplume can easily satisfy the timing constraints on the formation of the dichotomy. In the last part we consider the coupled core-mantle thermal evolution and investigate the cooling of the initially superheated core and the generation of the magnetic field on early Mars. We show that the core cooling is sufficiently rapid to induce convection inside the core and allow the operation of the magnetic dynamo. In our models, the magnetic field exists for millions to hundreds of millions of years after planetary formation, which is consistent with observations.

Chapter 1

Introduction

1.1 The interior structure of Mars

1.1.1 Bulk composition

Mars, the fourth planet from the Sun, has a planetary mass of $6.4 \cdot 10^{23}$ kg and a mean radius of 3390 km [*Schubert et al.*, 1992], which yields a mean density of 3934 kg m^{-3} [*Spohn et al.*, 1998]. The mean density suggests that within the first-order approximation Mars has an interior structure similar to other terrestrial planets. Figure 1.1 shows a possible interior structure of Mars and the relative sizes and interior structures of other terrestrial planets and the Moon. A widely accepted composition model is *Dreibus and Wänke* (DW hereafter) model [1985] which is based on data for Martian meteorites. The K/Th ratio calculated from DW model agrees with the observed surface K/Th ratio by the gamma ray spectrometer on Mars Odyssey [*Taylor et al.*, 2007].

1.1.2 Crust

The crustal thickness is an important parameter of the interior structure. Unfortunately, without seismic data, it has to be determined indirectly. There are many studies utilizing different techniques to achieve reasonable estimates. Global gravity and topography admittance studies expand the observed gravity and topography by spherical harmonic degree and calculate gravity/topography admittance. A set of theoretical admittance values is calculated at different crustal thicknesses under the assumption of simple Airy isostasy (uniform crustal density). By matching the observed value with the theoretical values, the mean crustal thickness falls between 50 and 200 km [*Bills and Nerem*, 1995; *Yuan et al.*, 2001]. The biggest challenge for this type of study is the assumption of uniform crustal density. Moreover, global admittance studies do not consider that the topography might be supported by different mechanisms at different areas.

Local gravity and topography admittance studies can estimate the crustal thickness at different locations. One technique is to apply a windowing function to both gravity and topography. *McGovern et al.* [2002] studies several local areas, including Noachis Terra and Hellas basin, and suggests that the mean crustal thickness varies from 8 to 68 km depending on the sites, and the best fit is 50 km. Another technique is to use line-of-sight data to find the transfer function Z between the topography $\bar{h}$ and free air gravity $\Delta\bar{g}$ ($\Delta\bar{g} = Z\bar{h}$ when both are small) [*McKenzie et al.*, 2002]. The transfer function Z can be theoretically calculated with different effective elastic thicknesses. Similar to global admittance studies, the best match between the observation and the theoretical calculation generates the estimate of the effective elastic thickness. *McKenzie et al.* [2002] reveals that the effective elastic thickness T_e varies from 14.5 km to 70 km under the southern hemisphere and Tharsis, respectively. However, the relationship between the crustal thickness and the effective elastic thickness is not clearly defined [*Wieczorek and Zuber*, 2004].

Global crustal thickness inversion by using Bouguer gravity anomalies [*Zuber et.*

al., 2000] finds that the mean crustal thickness should be greater than 32 km [see *Wieczorek and Zuber*, 2004 for the correction] if the minimum crustal thickness is 3 km beneath Isidis. Considering the true crustal thickness beneath Isidis might be larger, this inversion can only give the lower limit of the mean crustal thickness.

There are several other methods to estimate the mean crustal thickness. Using viscous relaxation model, *Nimmo and Stevenson* [2001] estimates that the upper limit of the mean crustal thickness to be less than 100 km. However, viscous relaxation of surface topography greatly depends on mantle temperature and mantle viscosity. Geochemical mass balance calculation based on chemical composition model can also provide constraints on the crustal thickness. *McLennan* [2001] suggests a maximum crustal thickness 65 km based on the concentrations of long-lived heat-producing elements (K, Th, and U).

1.1.3 Mantle

Adopting DW model, *Bertka and Fei* [1997] determined the mineralogy by performing high-temperature high-pressure experiments. The upper mantle consists of olivine, clinopyroxene, orthopyroxene, and garnet up to 9 GPa. A transition zone of spinel and majorite almost reaches the core-mantle boundary. The existence of a phase transition from spinel to perovskite and magnesiowüstite near the CMB depends on the size of the core. Only when mantle pressure reaches 23 GPa, which means the core radius has to be less than $\sim$ 1550 km, this phase transition appears and a layer of perovskite and magnesiowüstite sits on top of the CMB (Figure 1.2) Numerical simulations suggest that this phase transition can strongly affect the style of mantle convection by promoting a convective pattern with one mantle plume, which might explain the formation of Tharsis volcanic center [*Harder and Christensen*, 1996].

Mantle temperature is an important parameter that determines whether the mantle is liquid, solid, or partially molten. Mantle solidus and liquidus temperatures have been determined by melting experiments on anhydrous mantle peridotite at 5 to 22.5 GPa [*Zhang and Herzberg*, 1994] (Figure 1.3). Initial mantle temperature is likely to be slightly below the solidus temperature because vigorous convection can cool the mantle very fast and decrease mantle temperature to below solidus [*Williams and Nimmo*, 2004].

Another important parameter is mantle rheology. It strongly affects mantle dynamics and evolution. The two main creep mechanisms are diffusion creep and dislocation creep. At a low stress level, rock deformation is controlled by the diffusion of point defects within crystal lattice. Diffusion creep leads to a Newtonian fluid behavior of crystalline solids (the strain rate is linearly related to the stress). When the stress level is high, the migration of dislocations dominates. For dislocation creep, the strain rate has a power-law dependence on the stress [*Turcotte and Schubert*, 2002]. The transition from one creep mechanism to another depends on various factors such as composition and grain size. On Earth, diffusion creep probably dominates [*Karato and Wu*, 1993]. In our study we only consider diffusion creep.

1.1.4 Core

Two outstanding questions are the state and the size of the core. The state of the core can be inferred from several approaches. A lower k_2 Love number from tidal observations means a higher planetary rigidity, which suggests a more solid core. The possibility of a completely solid iron core has been ruled out by the observation of a sufficiently large k_2 Love number [*Yoder et al.*, 2003]. Another approach is to utilize high-pressure high-temperature experimental melting data. The composition of the core is mainly iron with a small amount of light elements, such as sulfur. According to the melting data, at the CMB pressure the iron–sulfur system has a relatively low melting temperature ($\sim 1400 - 1600$ K) with any reasonable amount of sulfur (Figure 1.4) [*Boehler*, 1996; *Fei and Bertka*, 2005; *Chudinovskikh and Boehler*, 2007]. The mantle temperature at the CMB is estimated to be $1600 - 1920$ K [*Zharkov and Gudkova*, 2000]. Assuming the core is hotter than the mantle, the temperature of the core at the CMB will be higher than the melting temperature, so that the core is at least partially liquid. Furthermore, if there is a solid inner core, the solidification of the inner core, in theory, can power a dynamo [*Stevenson et al.*, 1983]. Such a dynamo will generate a global magnetic field which currently does not exist [*Acũna et al.*, 1999]. Therefore, it is generally believed that the Martian core is liquid.

The radius of the core is inferred to range from 1520 and 1840 km. The uncertainty comes from mantle composition, mantle temperature, and the crustal thickness. For instance, partial melt in the mantle may reduce the radius of the core [*Yoder et al.*, 2003]. In this work, we choose the core radius of 1700 km so that the ratio of the core radius to the planet radius is close to 0.5.

1.2 The hemispheric dichotomy on Mars

The hemispheric dichotomy refers to the fundamental differences between the southern and northern hemispheres on Mars. The dichotomy has three characteristics. First, the southern highlands (covering $\sim 60\%$ surface area) are on average ~ 3 km higher than the remaining northern lowlands, and the maximum elevation difference is ~ 6 km [*Smith et al.,* 1999] (Figure 1.5). According to isostasy, the topographic difference has to be compensated by a thicker crust beneath the southern highlands than the crust beneath the northern lowlands if the crustal density is uniform. Gravity/topography admittance studies indicate that the crust thins progressively from south to north [*Zuber et al.*, 2000] (Figure 1.6). Second, the southern highlands are heavily cratered, while the northern lowlands have been resurfaced and are less cratered. This observation suggests that the surface of the southern hemisphere is older because more craters usually means older age. However, recently discovered Quasi-Circular Depressions (QCDs), which are buried in the northern lowlands, suggest the lowlands might be as old as the highlands [*Frey et al.*, 2002; *Frey*, 2006] (Figure 1.7). Third, the remnant crustal magnetism in the southern hemisphere is much stronger than that in the northern hemisphere [*Acuña, et. al.*, 1999] (Figure 1.8).

The formation time of the dichotomy is determined mainly by using crater chronology. Using lunar crater statistics and age information from lunar samples, we can infer the crustal age through crater size frequency distribution (SFD), and the dichotomy is estimated to form ~ 3.9 Gyr ago [*Hartmann and Neukum*, 2001].

1.3 The origin of the dichotomy

Two different types of mechanisms, exogenic and endogenic, have been proposed to explain the formation of the dichotomy. Impact(s) have long been considered the only exogenic process that may create the dichotomy. The debate within the impact hypothesis is whether a single mega-impact [*Wilhelms and Squyres*, 1984] or several large impacts [*Frey and Schultz*, 1988] caused the dichotomy. *Wilhelms and Squyres* [1984] proposed the existence of the largest basin on Mars, Borealis basin, and suggested that this basin was the result of a mega-impact that produced the dichotomy. *Frey and Schultz* [1988] questioned the existence of the Borealis basin and argued that if the Borealis basin is the largest one on Mars there would be more large basins based on the statistics of size-frequency distribution. However, those large basins are not observed. They suggested that the dichotomy was produced by several large impacts instead of one mega-impact. Recently, a series of papers were published in favor of mega-impact hypothesis. *Andrews-Hanna et al.* [2008] refined the dichotomy boundary by using new gravity and topography data and removing the effect of Tharsis. Their result shows that the dichotomy boundary could be best fit by an ellipse, which indicates a giant impact origin. Moreover, numerical simulations using two different techniques [*Marinova et al.*, 2008; *Nimmo et al.*, 2008] show that it is possible to have a mega-impact which can create the dichotomy without destroying the planet if the impact satisfies a set of conditions (e.g. impact velocity, impact angle).

For endogenic processes, different models have been proposed. *Wise et al.* [1979] proposed a mantle overturn or first-order convection (one-cell convection/degree-1 convection) model that might create the northern lowlands through subcrustal erosion (thinning). They also suggested that the Tharsis volcanoes are long-lived thermal effects of the convection cell. However, they did not explain how the orientation of the convection cell changes from pole region to equatorial region. *McGill and Dimitriou* [1990] proposed a similar mechanism. Early plate tectonics on Mars [*Sleep*, 1994] may also explain the thinner northern crust as a younger crust generated by seafloor spreading. Recently discovered magnetic lineations in Meridiani is a strong evidence of early plate tectonics on Mars [*Connerney et al.*, 2005]. *Zhong and Zuber* [2001] found that if there is a weak asthenosphere (100 times weaker than the mantle), degree-1 mantle convection can happen within a relatively short time scale (~ 100 Myr) due to Rayleigh-Taylor instability in the 2-D axisymmetric model. Mantle overturn caused by fractional crystallization can also generate degree-1 mantle flow that creates the dichotomy through crustal thinning [*Elkins-Tanton et al.*, 2003, 2005a]. Based on *Zhong and Zuber*'s model, *Roberts and Zhong* [2006] uses a more realistic rheology and generalizes the model to a 3-D geometry. After comparing this viscosity layering models with the models with an endothermic phase transition near the CMB [*Harder and Christensen*, 1996; *Harder*, 1998, 2000], they point out that the model of phase transition can generate degree-1 mantle convection only when the rheology is weakly temperature-dependent, while viscous layering can generate degree-1 convection.

1.4 The transient superplume hypothesis

The hypothesis that we develop here [*Ke and Solomatov*, 2004, 2006, 2009] suggests that the hot core of early Mars produces a transient superplume that generates large amounts of melt and created a thick crust in one hemisphere of Mars.

Although fluid dynamics of plume formation has been extensively studied [*Loper and Stacy*, 1983; *Griffiths*, 1986; *Hansen et al.*, 1990; *Manga and Weeraratne*, 1999; *Manga et al.*, 2001; *Lithgow-Bertelloni et al.*, 2001], plume formation is not well understood for very large viscosity contrasts which is relevant to the terrestrial planets. On the present-day Earth, a temperature contrast of 1000 to 2000 K across the thermal boundary layer at the core-mantle boundary and a strongly temperature-dependent mantle rheology [*Karato and Wu*, 1993; *Yamazaki and Karato*, 2001], suggest that the viscosity contrast across the boundary layer exceeds 10^4. This viscosity contrast might be even larger in early history because the temperature contrast is likely to be larger as suggested by thermal evolution models [*Stevenson et al.*, 1983].

Plume formation at such large viscosity contrasts is quite complicated. In particular, it involves an intermediate step, small-scale convection in the thermal boundary layer [*Yuen and Peltier*, 1980; *Christensen*, 1984; *Olson et al.*, 1987; *Thompson and*

Tackley, 1998]. Previous studies only reached the critical viscosity when small-scale convection starts but did not investigate this regime. The first stage of plume formation, small-scale convection in the thermal boundary layer, was systematically studied by *Solomatov and Moresi* [2002]. The second stage, large-scale instability of the thermal boundary layer, is studied in Chapter 2. A set of scaling laws is derived to calculate the instability growth rate, the onset time of plume formation, and the thickness of the TBL when plume forms. Two-dimensional numerical simulations are performed to verify the scaling laws.

In Chapter 3, we expand our 2-D model to 3-D spherical shell geometry and apply the 3-D model to early Mars. We find that within a likely range of parameters degree-1 mode is the most unstable mode and leads to the formation of an early transient superplume. We formulate the hypothesis that the dichotomy is caused by an early transient superplume produced by an early superheated core. We also discuss the arguments for the superheated Martian core.

In Chapter 4, we develop our hypothesis further. We take into account core cooling and study the coupled core-mantle thermal evolution. We combine parameterized convection calculations with finite element simulations. We show that the superheated core is cooled rapidly by the superplume and that a dynamo can be sustained for a short-period of time in the early history of Mars.

We summarize our work in Chapter 5 and point out possible future directions that can improve our understanding of the early evolution of Mars.

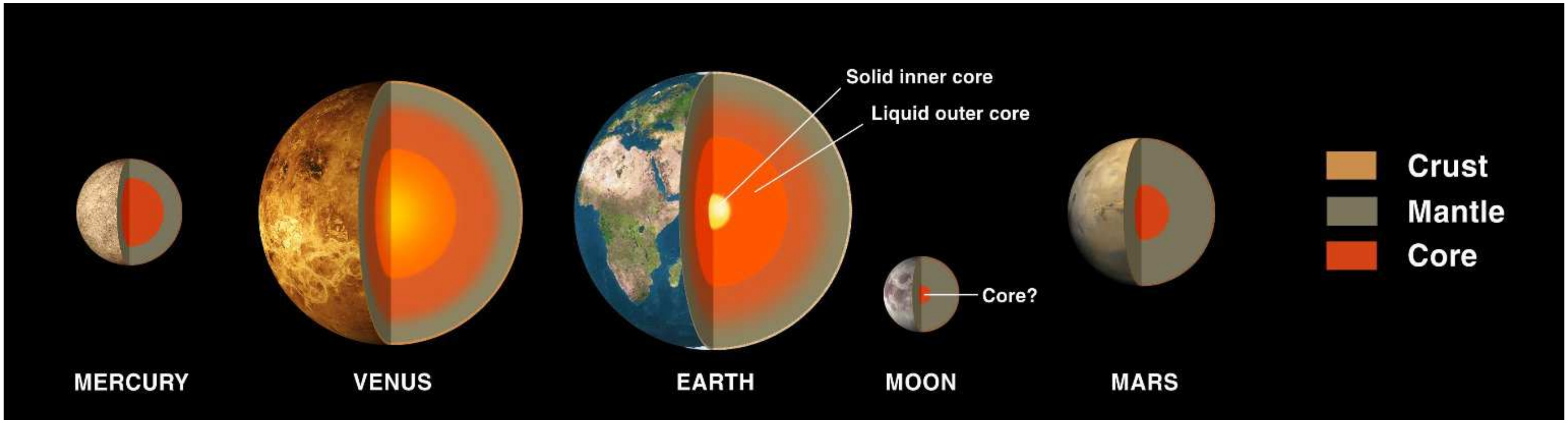

Figure 1.1: The interior structures of terrestrial planets. Photo is from NASA.

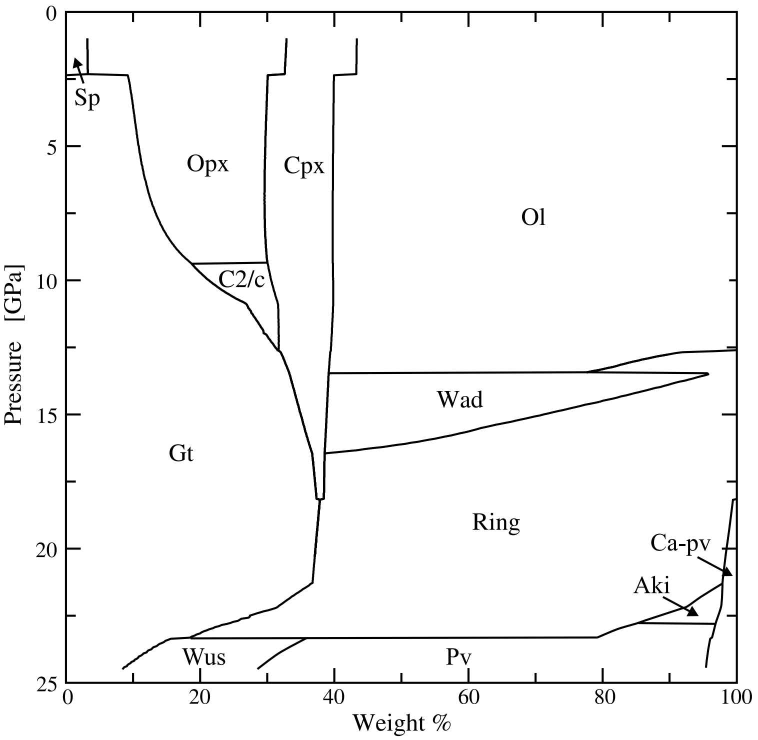

Figure 1.2: Computed model mineralogy for the Martian mantle based on the *Dreibus Wänke* [1985] composition model and the areotherm of *Bertka and Fei* [1997]. Aki: akimotoite, Ca-pv: calcium perovskite, Cpx: clinopyroxene, C2/c: pyroxene, Gt: garnet, Ol: olivine, Opx: orthopyroxene, Pv: perovskite, Ring: ringwoodite, Sp: spinel, Wad: wadsleyite, Wus: magnesiowustite. After *Khan and Connolly* [2008], copyright by AGU.

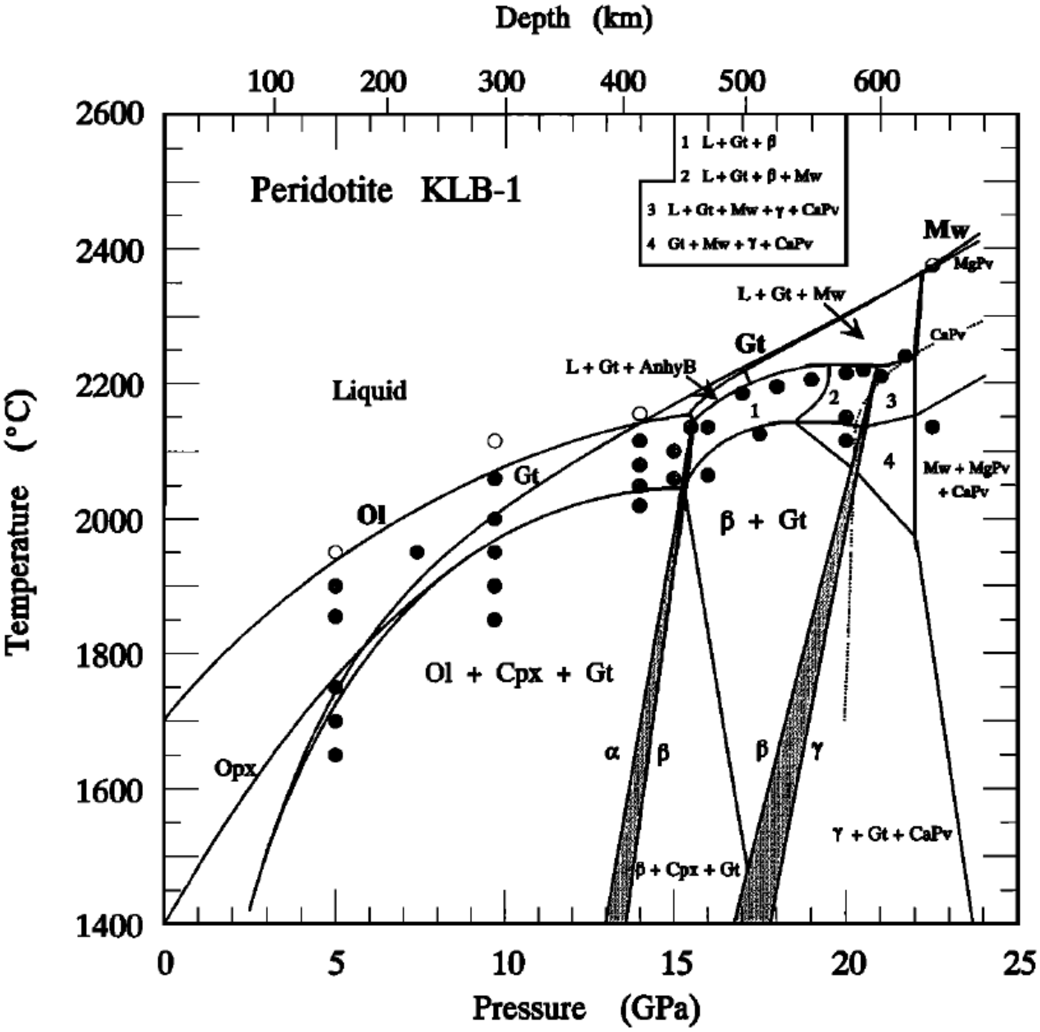

Figure 1.3: Phase diagram for anhydrous peridotite KLB-1: all crystalline (solid circles), crystals plus liquid (cross-hatched circles), all liquid (open circles), and precise liquidus determination at 2375°C and 22.5 GPa (half open and half cross-hatched circle). After *Zhang and Herzberg* [1994], copyright by AGU.

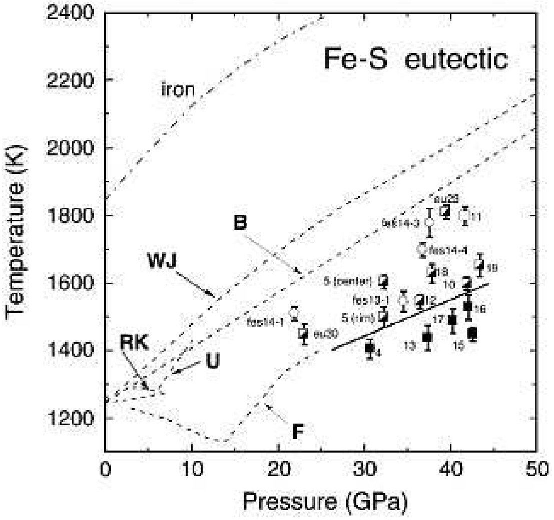

Figure 1.4: Pressure dependence of the eutectic temperature of the Fe-rich portion of the Fe-S system. Observations from recovery experiments: solid square - no melt features; mixed symbols - melt features together with solid phases; open squares: mainly quench textures recrystallized from liquid. Open circles: melting observed by in situ laser-speckle method. Solid line is the present solidus boundary. Dashed lines are previous eutectic measurements from different studies. After *Chudinovskikh and Boehler* [2007], copyright by Elsevier.

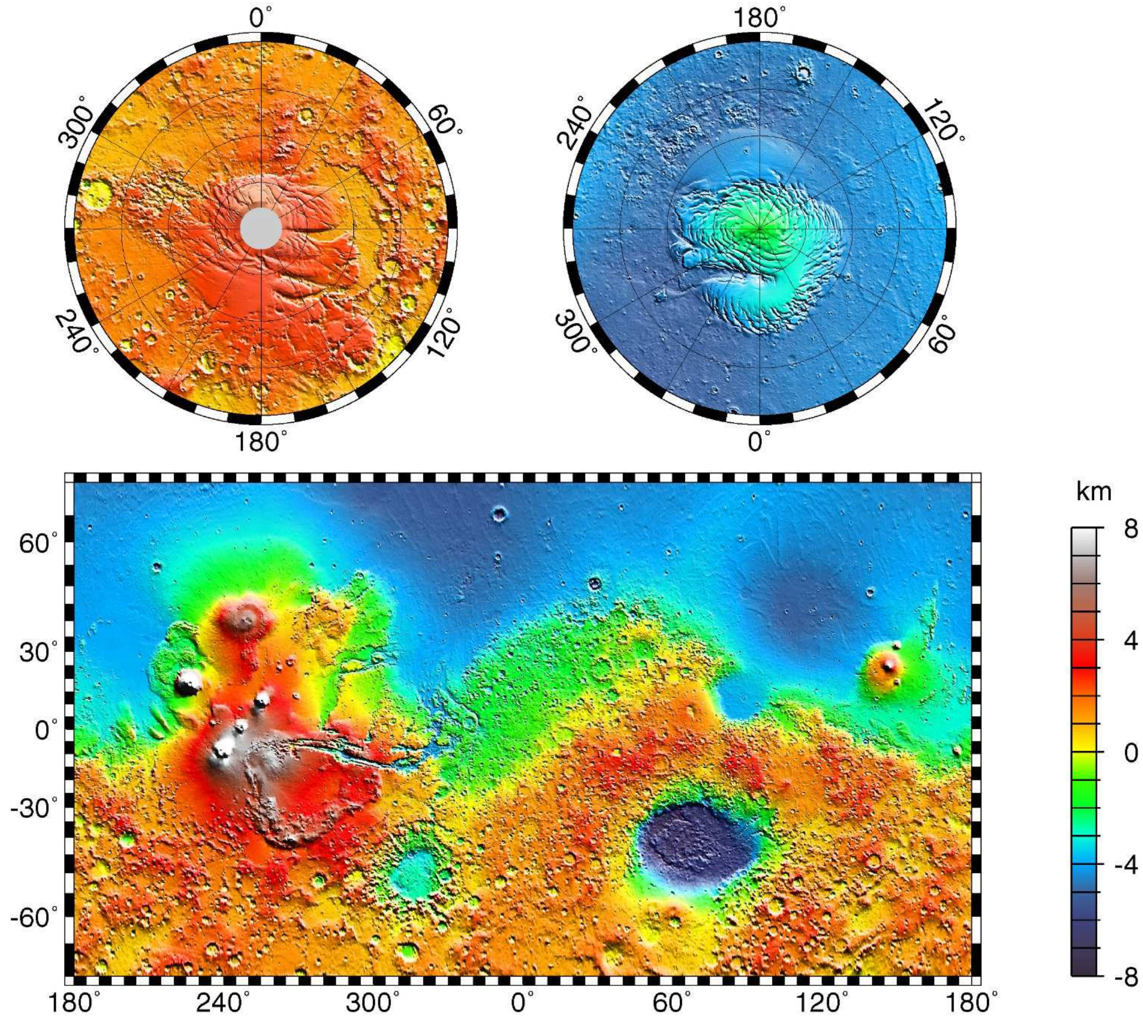

Figure 1.5: Maps of Mars global topography, obtained by Mars Orbiter Laser Altimeter (MOLA) on Mars Global Surveyor (MGS). Photo is from NASA.

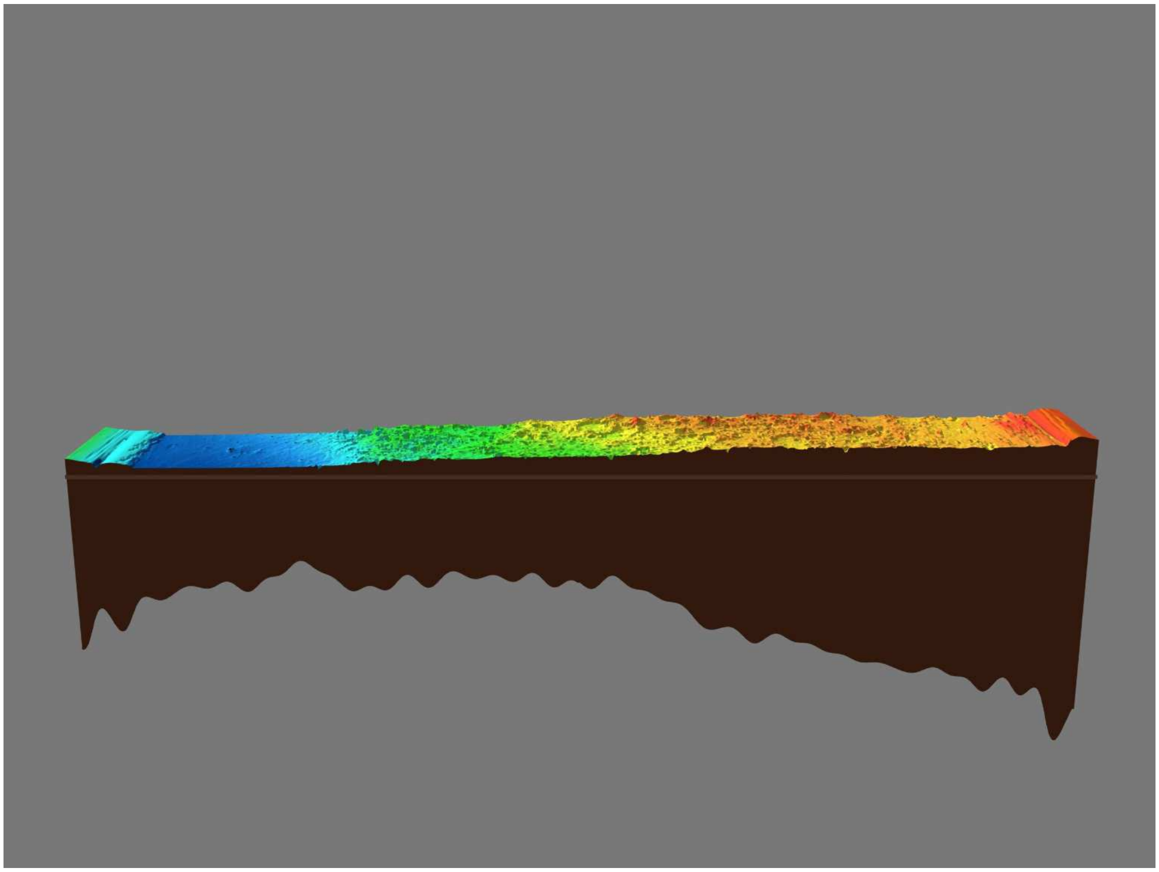

Figure 1.6: Model of Mars crustal thickness. It shows the downward slope of the topography from South to North, compensated by a thicker crust under the southern hemisphere. Photo is from NASA/Goddard Space Flight Center Scientific Visualization Studio.

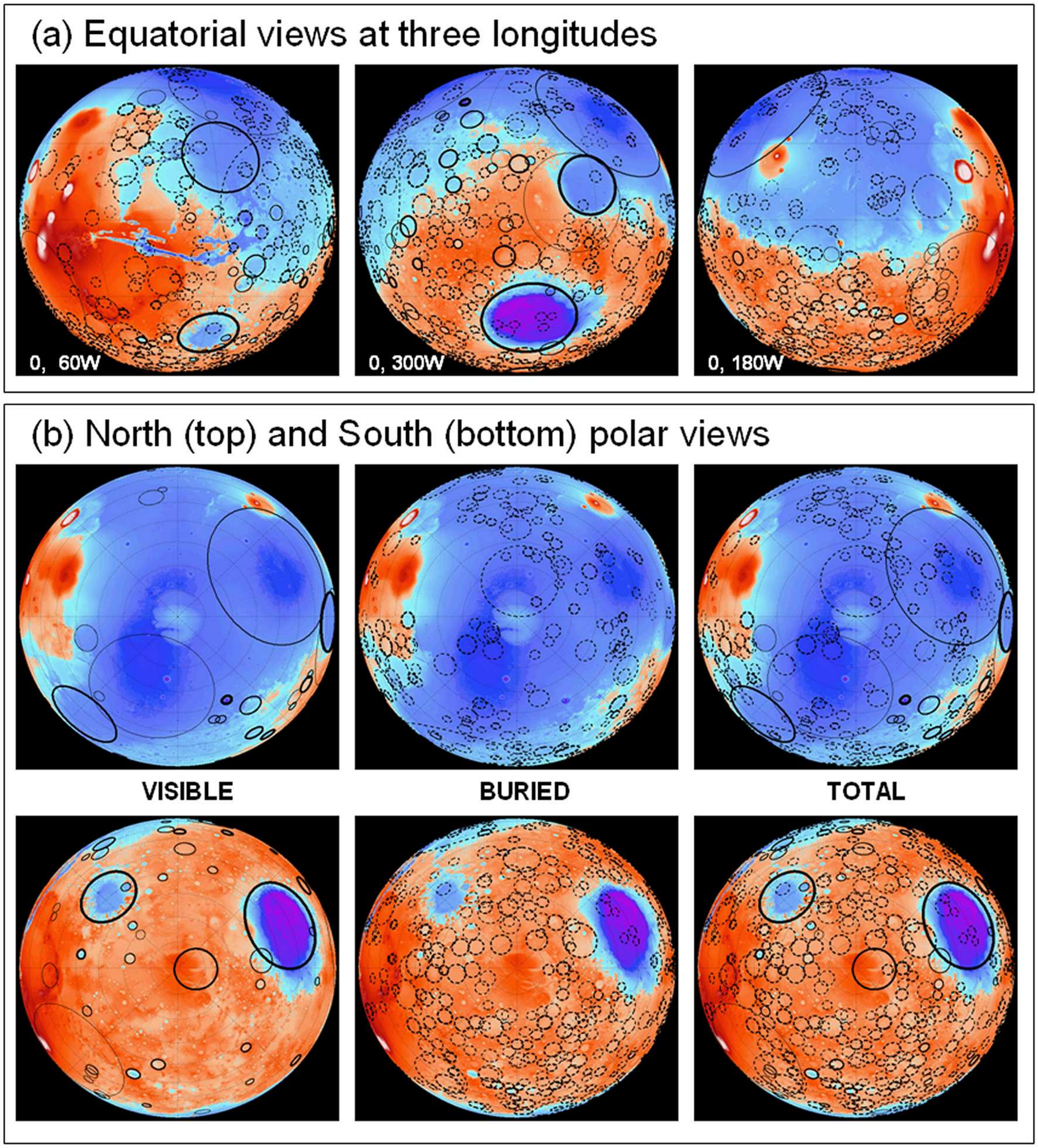

Figure 1.7: QCDs on Mars (> 200 km in diameter) over colored MOLA topography. Blues are lowlands, and reds are highlands. Solid circles show "visible" features known to be impact basins. Dashed circles represent features not visible on images and are believed to be buried impact basins. (a) Equatorial views at 60° W, 300°W, and 180°W. (b) Polar views. Buried features outnumber visible basins by a factor 6 in the highlands and a factor 20 in the lowlands. Note the greater density of QCDs in the Southern Hemisphere, corresponding to the cratered highlands. After *Frey* [2006], copyright by AGU.

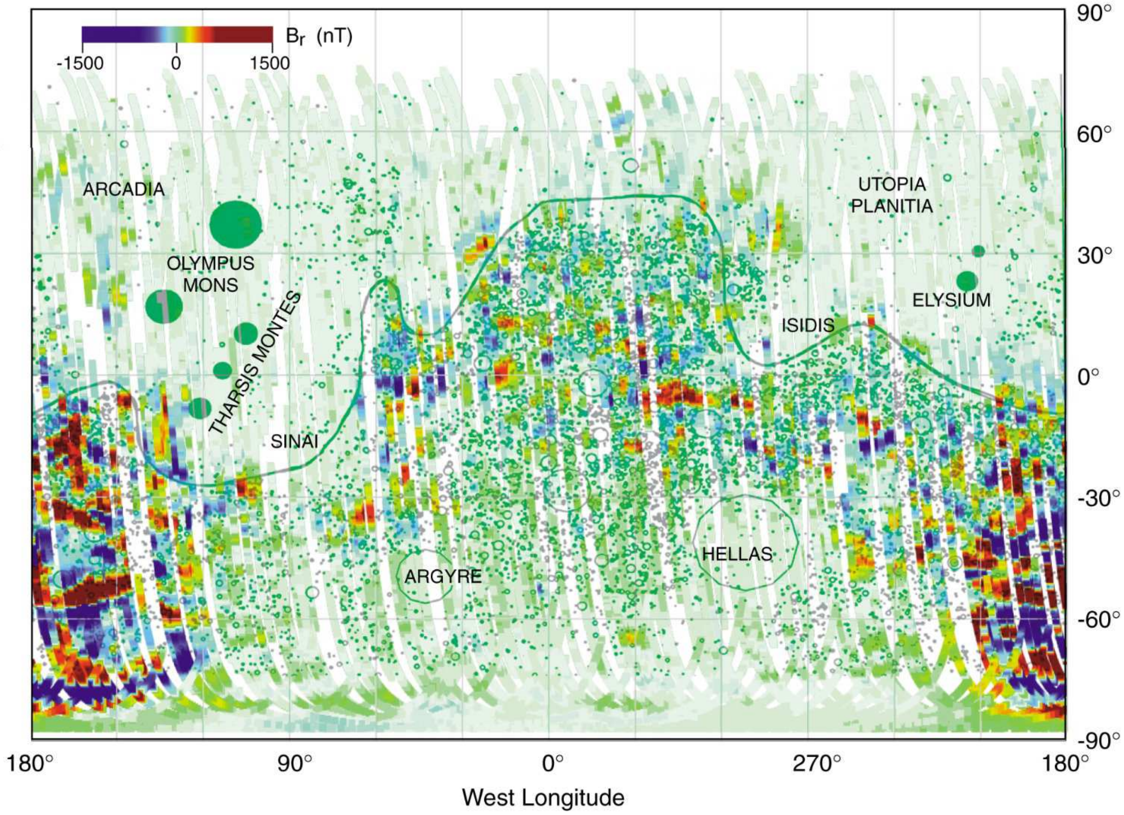

Figure 1.8: Map showing the distribution of crustal magnetic field sources superimposed on a map showing the distribution of craters greater than 15 km in diameter and the dichotomy boundary (solid line). The spacecraft tracks below 200-km altitude have been projected onto the surface as light green thick lines to illustrate the orbital coverage. The thickness of the subsatellite tracks has been chosen to approximate the equivalent "pixel" size for the observations. The measured radial (vertical) component of the magnetic field associated with the crustal sources is illustrated using a color scale that reveals the location of significant magnetic sources detected regardless of intensity. Note the high correlation between the region where magnetic crustal sources appear and high crater densities (ancient terrain) and the absence of magnetic imprints within the Hellas, Argyre, and Isidis impact basins. No magnetic signatures have been found over Elysium, Olympus Mons, or Tharsis Montes. After *Acũna et al.* [1999]. Photo is from NASA.

Chapter 2

Plume formation in strongly temperature-dependent viscosity fluids over a very hot surface

Yun Ke and Slava Solomatov

Physics of Fluids, 16, 1059-1063, 2004.

Plume formation in a strongly temperature-dependent viscosity fluid placed on a very hot surface involves an intermediate step – small-scale convection in the thermal boundary layer. We perform numerical simulations and suggest a simple analysis of this process using the stagnant lid convection theory and Canright and Morris' theory of Rayleigh-Taylor instability of two layers with different viscosities. We show that plume formation can approximately be predicted from the requirement that the growth of the large-scale instability becomes faster than the growth of the convecting thermal boundary layer.

2.1 Introduction

Plumes are important features of mantle dynamics on the Earth and other planets. They are thought to be responsible for volcanic "hotspots" such as Hawaii and Yellowstone and for gigantic flood basalts events in the past history of the Earth [*Morgan*, 1971; *Richards, et al.*, 1989; *Loper*, 1998]. They also remove heat from the Earth's interior and provide an efficient cooling of the core which is required for the generation of the magnetic field [*Stevenson et al.*, 1983]. They might play a significant role in global climate and mass extinctions [*Renne et al.*, 1995; *Loper*, 1998].

Although plume dynamics has been extensively studied in various regimes including high Rayleigh numbers and variable viscosity [*Loper and Stacy*, 1983; *Griffiths*, 1986; *Hansen et al.*, 1990; *Mange and Weeraratne*, 1999; *Manga et al.*, 2001; *Lithgow-Bertelloni et al.*, 2001]. it is not well understood at very large viscosity contrasts which is relevant to the Earth's mantle. Plumes presumably form as a result of instabilities of the thermal boundary layer at the base of the mantle. A temperature contrast of 1000 to 2000 K across the thermal boundary layer [*Williams*, 1998; *Boehler*, 2000] and a strong dependence of the mantle viscosity on temperature [*Yamazaki and Karato*, 2001] suggest that the viscosity contrast across this boundary layer is larger than 10^4. It was observed that at such high viscosity contrasts, plume formation involves an intermediate step – small-scale convection in the thermal boundary layer [*Yuen and Peltier*, 1980; *Christensen*, 1984; *Olson et al.*, 1987; *Thompson and Tackley*, 1998]. Previous investigators only reached the critical viscosity when small-scale convection appears but did not investigate this regime. The first stage of plume formation, small-scale convection in the thermal boundary layer, was systematically investigated by *Solomatov and Moresi* [2002]. The goal of this study is to understand the second stage, large-scale instability.

2.2 Model

We consider an idealized two-dimensional box $H \times L$ with the initial temperature $T_0 = 0$. This box is subject to instantaneous heating from below caused by a sudden increase of the bottom temperature from T_0 to $T_b > T_0$ at time $t = 0$. The horizontal and vertical boundaries are free-slip. The side boundaries are thermally insulated.

Convection in a cell with a fixed temperature difference ΔT between the boundaries and with free-slip boundary conditions is described by the following equations:

$$\nabla \cdot \mathbf{u} = 0, \tag{2.1}$$

$$0 = -\nabla p + \alpha \rho g T \mathbf{n} + \nabla \cdot [\mu(\nabla \mathbf{u} + \{\nabla \mathbf{u}\}^T)], \tag{2.2}$$

$$\frac{\partial T}{\partial t} + \mathbf{u} \cdot \nabla T = \nabla^2 T, \tag{2.3}$$

where $\mathbf{u}$ is the velocity vector, T is the temperature, p is the pressure perturbations, α is the thermal expansion, g is the acceleration due to gravity, $\mathbf{n}$ is a unit vector in the direction of gravity, $\kappa = k/\rho c_p$ is the coefficient of thermal diffusion, ρ is the density, k is the thermal conductivity, c_p is the heat capacity at constant pressure, μ is the viscosity and $\{\}^T$ is the transpose operator. The viscosity is assumed to be an exponential function of temperature:

$$\mu = \mu_0 \exp(-\gamma T) \tag{2.4}$$

where γ is a constant.

To non-dimensionalize the problem, we choose H as the length scale, $t_0 = H^2/\kappa$ as the time scale, and $\Delta T = T_b - T_0$ as the temperature scale. The two non-dimensional parameters are the Rayleigh number

$$Ra_0 = \frac{\alpha \rho_0 g \Delta T H^3}{\kappa \mu_0} \tag{2.5}$$

where μ_0 is the viscosity at $T = T_0$, and the parameter

$$\theta = \gamma \Delta T \tag{2.6}$$

which determines the total viscosity contrast $\exp(\theta)$ across the layer.

To initiate small-scale convection small sinusoidal perturbations are added at the very bottom of the layer. Small-scale convection is not sensitive to the exact perturbation function because the cell size is self-regulated and increases during the growth of the convective boundary layer [*Solomatov and Moresi*, 2002].

Once developed, small-scale convection generates perturbations which, theoretically, can cause large-scale instability and produce a plume. However, at the Rayleigh numbers that we can reach the growth rate of these, very short wavelength perturbations is so small that the convective boundary layer propagates through the entire layer without producing plumes. Thus, to initiate the large-scale instability, we need to impose large-scale perturbations. An obvious choice would be to use random perturbations and determine the fastest growing mode. However, as we explain later, there is a broad range of wavelengths at which the growth rate is approximately constant. Instead of one fastest growing mode there is a range of modes growing at about the same rate. Under such conditions, the results would be difficult to analyze. Therefore, we systematically investigate the dependence of the growth rate on the wavelength using single mode temperature perturbations:

$$\delta T(x, z) = \varepsilon \cos(2\pi x/\lambda) \sin[\pi(1 - z)], \tag{2.7}$$

where $\varepsilon = 0.001$ is the amplitude of the perturbation and $\lambda = 2L$ is the wavelength.

2.3 Numerical simulations

The numerical simulations are performed using the finite element code CITCOM [*Moresi and Solomatov*, 1995]. The viscosity contrast is $\exp(\theta) = 10^6$. Two values of the Rayleigh number Ra_0 are considered: 3×10^3 and 10^4. These values are sufficiently high to ensure that the instability occurs when the thickness of the convecting thermal boundary layer is substantially smaller than the thickness of the entire layer (otherwise we would get a different regime in which small-scale convection propagates through the entire layer without generating a plume). On the other hand, these values are low enough to obtain accurate solutions with 128 finite elements in the vertical direction.

The aspect ratio of the numerical domain varies from 0.5×1 to 32×1 (the number of finite elements varies from 64×128 to 4096×128 respectively). This corresponds to λ from 1/4 to 16. All cases studied are in the regime in which the characteristic length scale of small-scale convection is much smaller than the length scale of large-scale instabilities. Figure 2.1 shows an example of plume formation in a 1×1 box for $\mathrm{Ra}_0 = 10^4$. This example clearly shows the development of small-scale convection in the thermal boundary layer followed by plume formation as a result of large-scale instability of the thermal boundary layer. Other cases are very similar and are not shown (besides, cases with large aspect ratios are difficult to visualize).

For the purpose of constraining the onset of plume formation, the simulations need to be run only long enough to reach the initial stage of plume formation. To do so we traced the height d_1 and the growth rate $\dot{d}_1$ of the convective thermal boundary layer. This interface is defined by an isotherm $T = T_\mathrm{L}$. The value of T_L can be chosen as the isotherm $T_\mathrm{L} = 1 - 3.7\theta^{-1} \approx 0.73$ defining the boundary of the actively convecting region (θ^{-1} is the scale for the typical temperature variations in the convective region and the coefficient 3.7 is estimated numerically and experimentally in previous studies [*Solomatov and Moresi*, 2002]. However, the fluctuations in the position of this isotherm are substantial because of the time-dependent character of small-scale convection. We choose $T_\mathrm{L} = 0.6$ instead and notice that the results are not very sensitive to the value of T_L as long as it remains within the sharp thermal front just above the convective thermal boundary layer.

We also calculated the growth of the large-scale instability. The amplitude w of the instability is defined as the average separation between the average left half and the average right half positions of the interface. This definition is chosen to minimize the effect of fluctuations (the difference in the positions of the boundary points of the interface turns out to be a less robust definition because of the fluctuations in the convective boundary layer). The growth rate of the instability is defined as $\dot{w}$. Temporal variations of d_1 and w for 1×1 box are shown in Fig. 2.2.

2.4 Analysis of the numerical results

2.4.1 Growth of the convective boundary layer

After the onset of small-scale convection, both the bottom heat flux and the growth rate of the convective boundary layer remain approximately constant (Fig. 2.2) – in agreement with stagnant lid convection theory [*Solomatov and Moresi*, 2002]:

$$\dot{d}_1 = \frac{F}{T_1} \tag{2.8}$$

where T_1 is the internal temperature of the convective boundary layer.

2.4.2 Large-scale instability of the thermal boundary layer

The thermally induced density contrast between the convecting boundary layer and the layer above it is the driving force for the large-scale instability of the whole system. It occurs simultaneously with the growth of the convecting boundary layer. This process is similar to the Rayleigh-Taylor instability in chemically and rheologically stratified layers.

To interpret the large-scale instability in terms of Rayleigh-Taylor instability consider the thermal structure of the layer in Fig. 2.3. The temperature profile is characterized by two nearly isothermal regions separated by a sharp interface (this structure was described in detail by *Solomatov and Moresi*, [2002]. The viscosity of the lower layer can be considered approximately constant because the convective mixing in this region maintains a nearly uniform temperature such that $1 - T_1 \sim \theta^{-1}$ [*Solomatov and Moresi*, 2002]. In our simulations, $T_1 \approx 0.908$ (independent of the Rayleigh number). The effective viscosity of the lower layer (the convective thermal boundary layer) is $\mu_1 = \mu_0 \exp(-\theta T_1)$ The thickness of the lower layer is d_1. The upper layer has the temperature $T_0 = 0$ and the viscosity μ_0 which are approximately constant because of the uniform initial conditions. The thickness of the upper layer is $d_0 = 1 - d_1$.

Thus, the large-scale instability can approximately be modeled as a Rayleigh-

Taylor instability in a system consisting of two uniform layers (Fig. 2.4). The viscosity contrast between the layers is $V = \mu_0/\mu_1$, the thickness ratio is $\beta = d_0/d_1$ and the (dimensional) density difference between the layers is $\Delta\rho = \alpha\rho_0(T_1 - T_0)$. An important difference between our case and Rayleigh-Taylor instability is that in the latter case the density contrast between the layers is compositional while in our case it is thermal and thus, can, in principle, be eroded by thermal diffusion. However, after the onset of small-scale convection thermal diffusion is unimportant because it becomes much slower than both the growth of the thermal boundary layer and the large-scale instability.

Applying the analytical solution for Rayleigh-Taylor instability of two compositionally distinct layers with different viscosities [*Canright and Morris*, 1993] to the growth of large-scale instability, we obtain

$$w(t) = w_0 e^{\sigma(t-t_{\mathrm{ss}})} \tag{2.9}$$

where t_{ss} is the time when small-scale convection starts (when the two-layer structure described above forms), w_0 is the amplitude of the perturbation at $t = t_{\mathrm{ss}}$, σ is the growth rate of the instability,

$$\sigma = \frac{Ra_0 V d_0 T_1}{\beta}\tilde{\sigma}, \tag{2.10}$$

and $\tilde{\sigma}$ is defined as follows [*Canright and Morris*, 1993]:

$$\tilde{\sigma} = \frac{1}{\tilde{k}} \frac{\left(S - \tilde{K}\right)(c-1) + V\left(s - \tilde{k}\right)(C-1)}{\left(S - \tilde{K}\right)\left(s + \tilde{k}\right) + 2V\left(Cc - 1 + \tilde{K}\tilde{k}\right) + V^2\left(S + \tilde{K}\right)\left(s - \tilde{k}\right)}, \tag{2.11}$$

where $\tilde{k} \equiv 2kd_1$, $\tilde{K} \equiv 2kd_0$, $c \equiv \cosh(\tilde{k})$, $C \equiv \cosh(\tilde{K})$, $s \equiv \sinh(\tilde{k})$, $S \equiv \sinh(\tilde{K})$

and $k \equiv 2\pi/\lambda$ is the wavenumber.

The growth rate depends on three dimensionless parameters: the viscosity contrast V, the thickness ratio β, and the non-dimensional wavenumber $\tilde{k}$. Canright and Morris' analysis [*Canright and Morris*, 1993] of the above equation shows that for $\beta \gg 1$ and $V \gg \beta^3$ (which applies to our case) there is a plateau, $(\beta/V)^{1/2} \ll \tilde{k} \ll \beta^{-1}$, where the growth rate of perturbations is almost independent of the wavenumber:

$$\tilde{\sigma} \approx \frac{\beta}{4V}. \tag{2.12}$$

Assuming that $\gamma \gg 1$ so that $T_1 \approx 1$, we obtain

$$\sigma \approx \frac{1}{4} Ra_0. \tag{2.13}$$

It is interesting to note that in this regime the large-scale instability is controlled by the viscous stresses in the upper layer and is not affected by the dynamics of the lower layer.

Figures 2.5 and 2.6 show a good agreement between the theoretical predictions and the numerical simulations. They also show that in agreement with the theory, instead of a sharp peak, there is a broad plateau where the dependence on the wavenumber is very weak.

2.4.3 Onset of plume formation

Eventually the thickness of the convecting boundary layer reaches a critical value at which the large-scale instability becomes faster than the growth rate of the convecting boundary layer and the system becomes unstable. This time is defined as the onset time, t_{pl}, of plume formation and is calculated from the requirement that

$$\dot{w} = \dot{d}_1. \tag{2.14}$$

Since $\dot{w} = w_0 \sigma e^{\sigma(t - t_{\mathrm{ss}})}$ we obtain

$$t_{\mathrm{pl}} = t_{\mathrm{ss}} + \frac{\ln(\delta_0/w_0)}{\sigma} \tag{2.15}$$

where

$$\delta_0 = \frac{F}{\sigma T_1}. \tag{2.16}$$

The thickness of the thermal boundary layer at the onset time is

$$\delta_{\mathrm{pl}} = 0.74 t_{\mathrm{ss}}^{1/2} + \frac{F}{T_1}(t_{\mathrm{pl}} - t_{\mathrm{ss}}) \tag{2.17}$$

where the coefficient 0.74 is the theoretical coefficient calculated from the conductive growth of the thermal boundary layer whose boundary is defined by the isotherm $T = T_{\mathrm{L}}$.

The theoretical predictions for the time t_{pl}, Eq. (2.15), and the thermal boundary layer thickness δ_{pl} at the onset of plume formation, Eq. (2.17), with σ defined by Eqs. (2.10)-(2.11) are in good agreement with the numerical results (Fig. 2.7 and 2.8).

2.5 Conclusion

We performed numerical simulations of plume formation in the regime of very large viscosity contrasts. In this regime, plumes form after an extended period of small-scale convection in the thermal boundary layer. A simple analysis based on the stagnant lid convection theory [*Solomatov and Moresi*, 2002] and the Rayleigh-Taylor instability theory [*Canright and Morris*, 1993] suggests that plume formation can approximately be described as a Rayleigh-Taylor instability of the two-layer system consisting of the vigorously convecting thermal boundary layer and a nearly isothermal layer above it. Plumes form when the growth rate of the large-scale instability of this two-layer system exceeds the growth rate of the convective thermal boundary layer. In the future it would be very interesting to investigate plume formation caused by perturbations associated with small-scale convection itself. This is a challenging problem which involves a strong interaction between the two scales of convection.

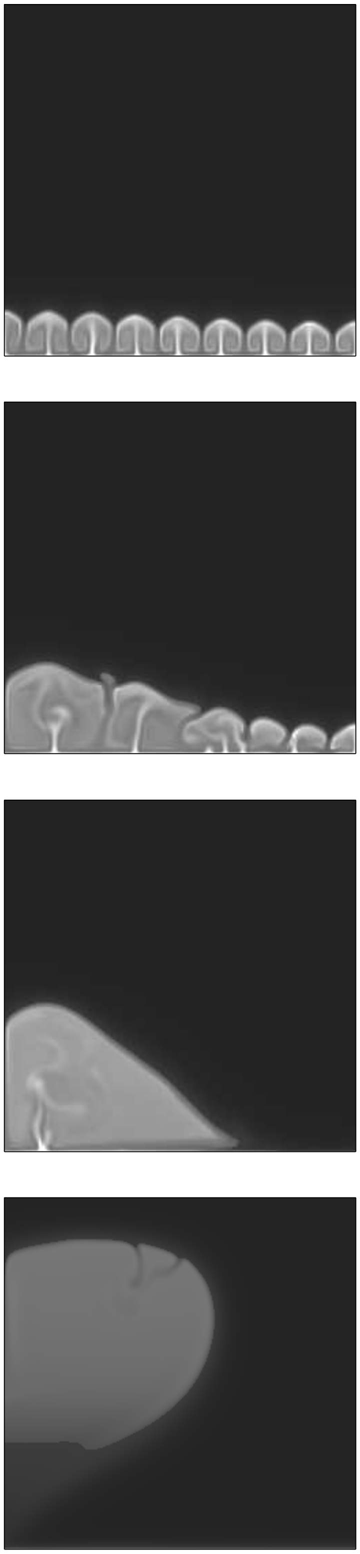

Figure 2.1: A sequence of snapshots showing plume formation at large viscosity contrasts in a 1×1 box and $\mathrm{Ra}_0 = 10^4$ (time increases downward).

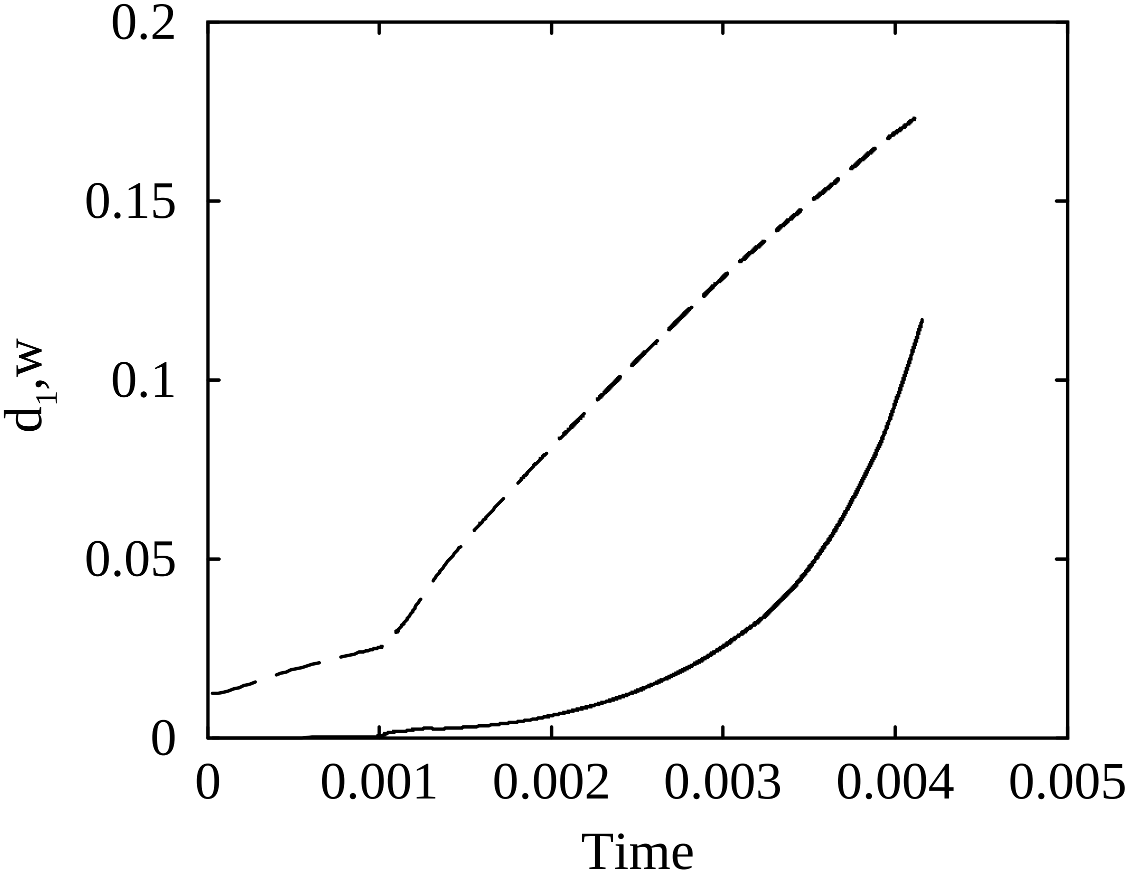

Figure 2.2: Thickness, d_1, of the thermal boundary layer (dashed line) and the amplitude, w, of the large-scale instability (solid line) for the 1×1 case at $\mathrm{Ra}_0 = 10^4$. The abrupt increase in the growth rate of the thermal boundary layer is caused by the onset of small-scale convection.

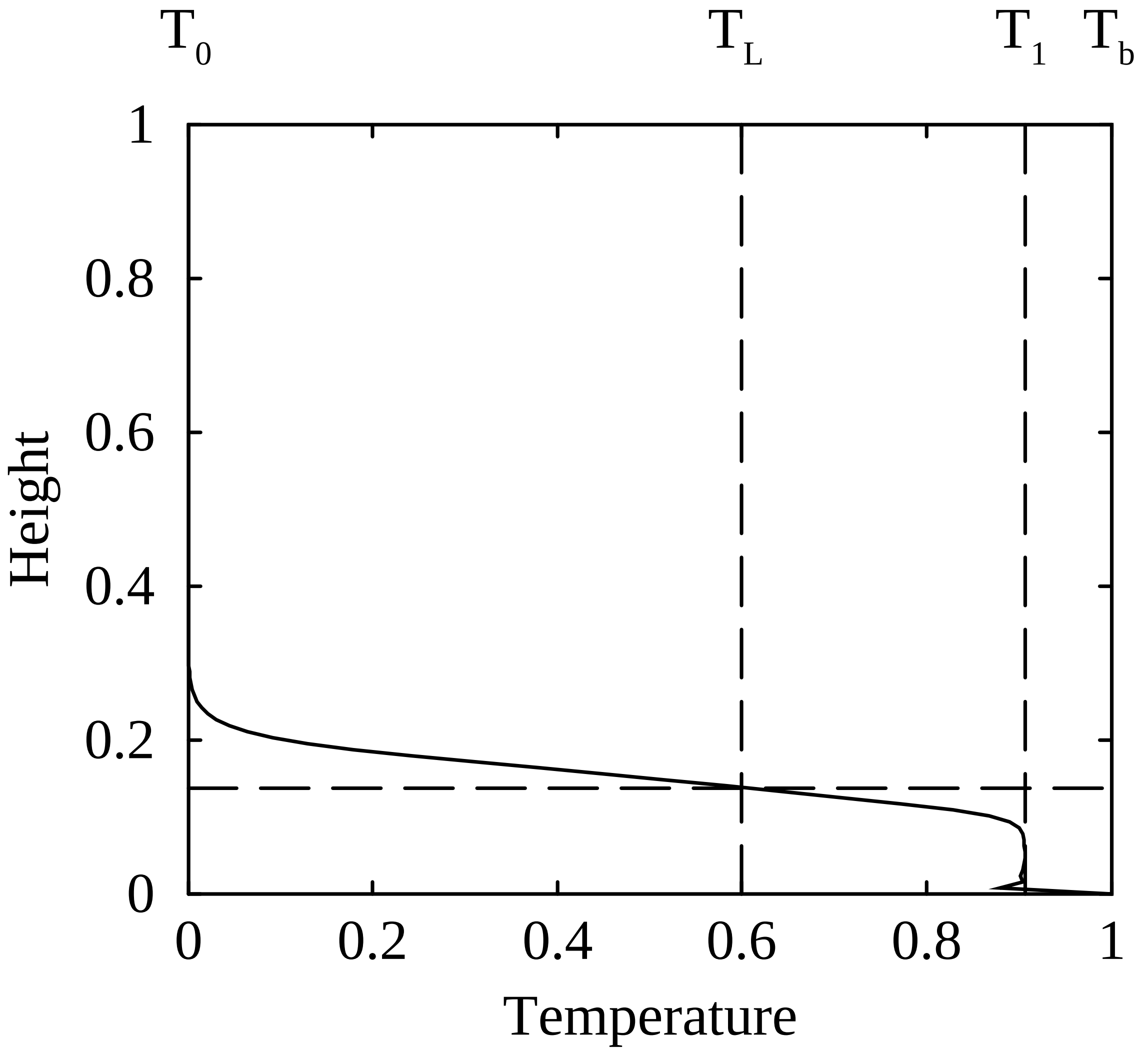

Figure 2.3: The temperature profile of the layer. The bottom temperature is $T_b = 1$. The surface temperature is $T_0 = 0$. Temperature in convective region is T_1. The interface between the upper and lower layers is determined by an isotherm $T = T_L$.

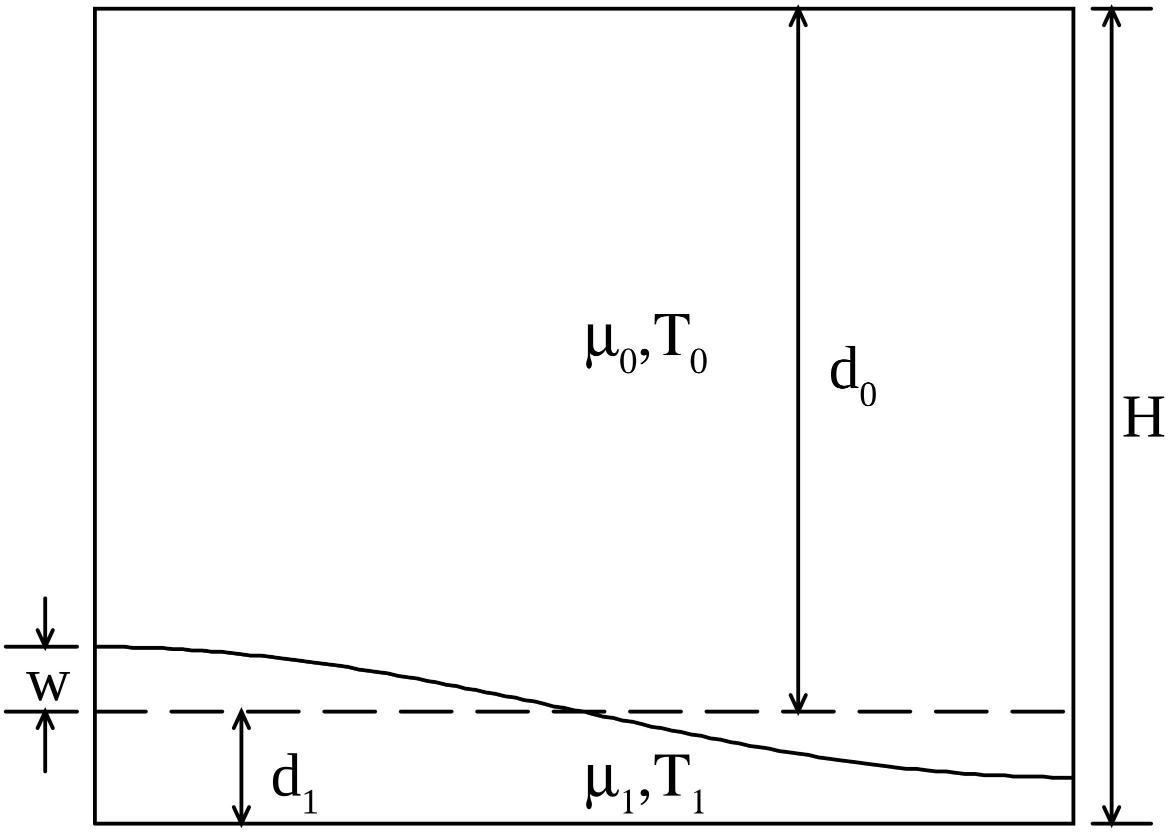

Figure 2.4: Interpretation of the large-scale instability in terms of Rayleigh-Taylor instability.

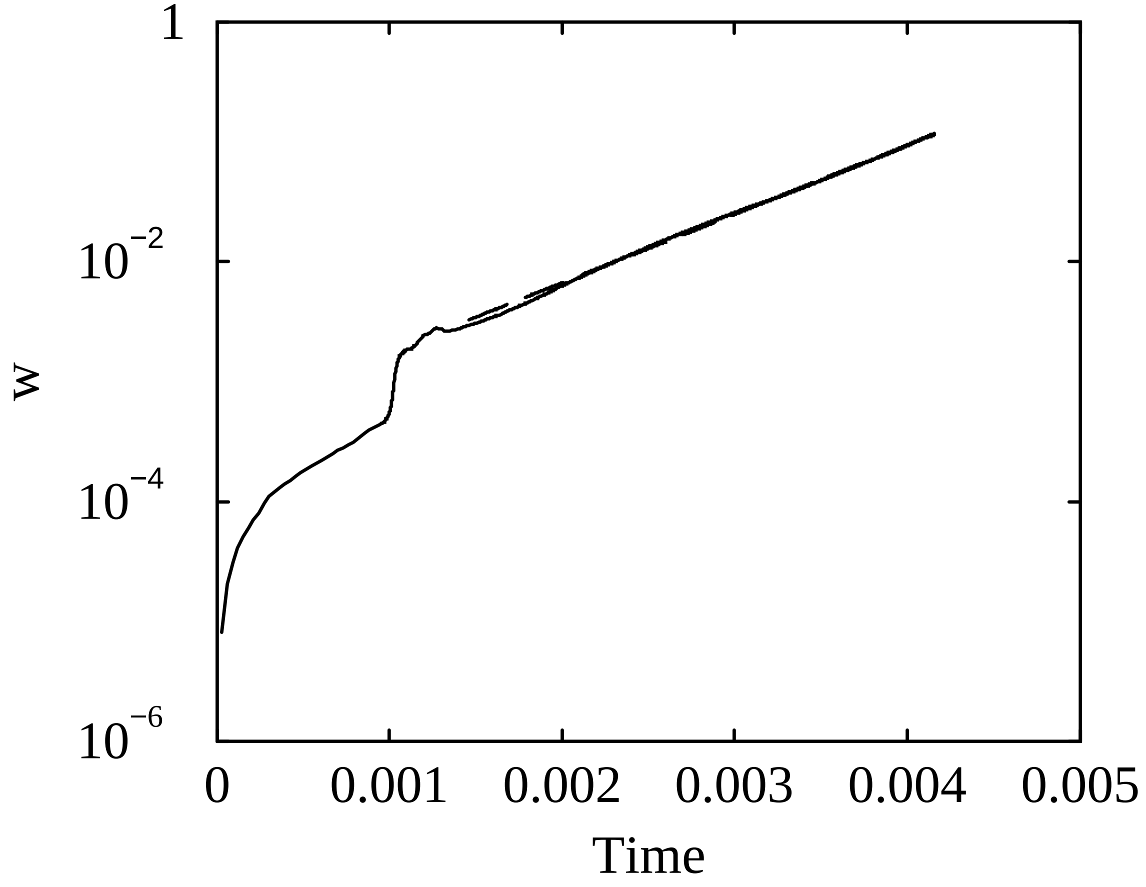

Figure 2.5: An example of exponential fit (dashed line) to the growth of the large-scale instability (solid line) (1×1 box, $\mathrm{Ra}_0 = 10^4$).

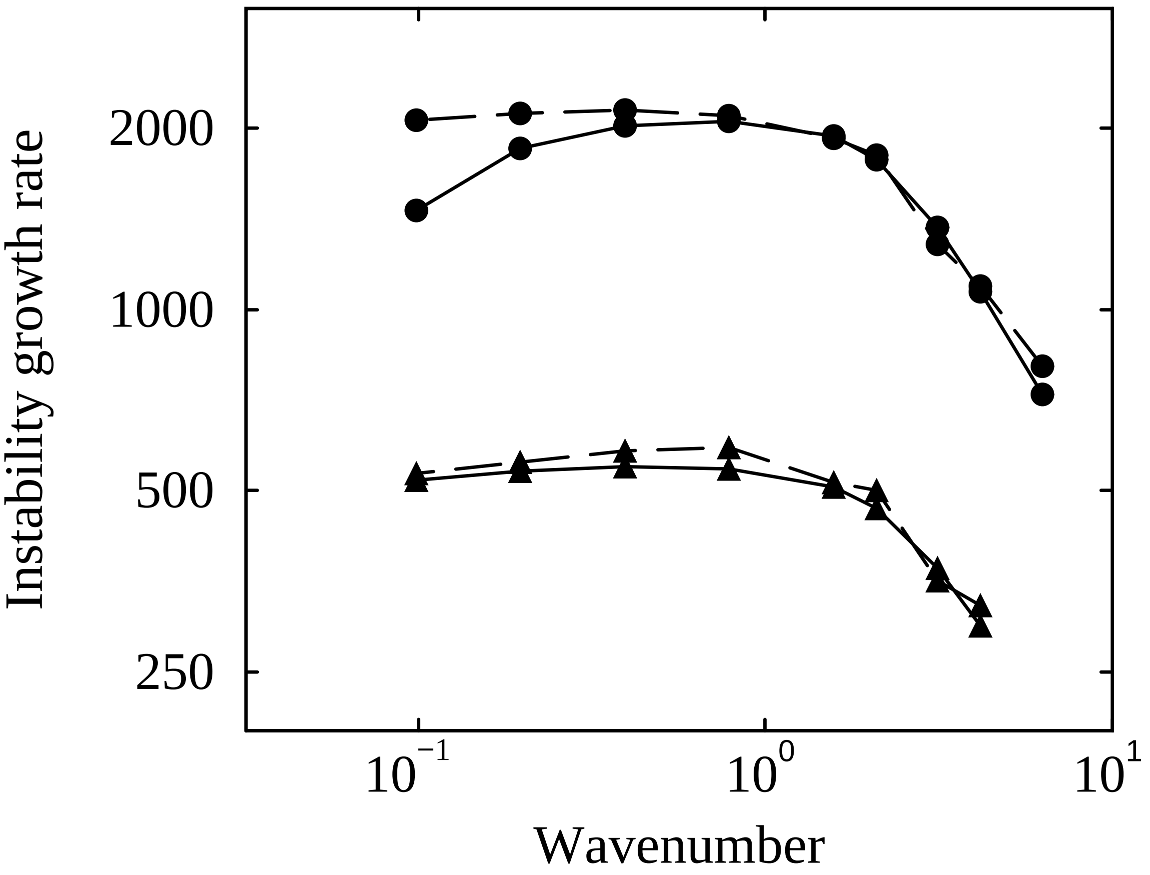

Figure 2.6: Theoretical predictions (solid lines) versus numerical results (dashed lines) for the instability growth rate as a function of wavenumber. Triangles correspond to $Ra = 3 \times 10^3$; circles correspond to $Ra = 10^4$.

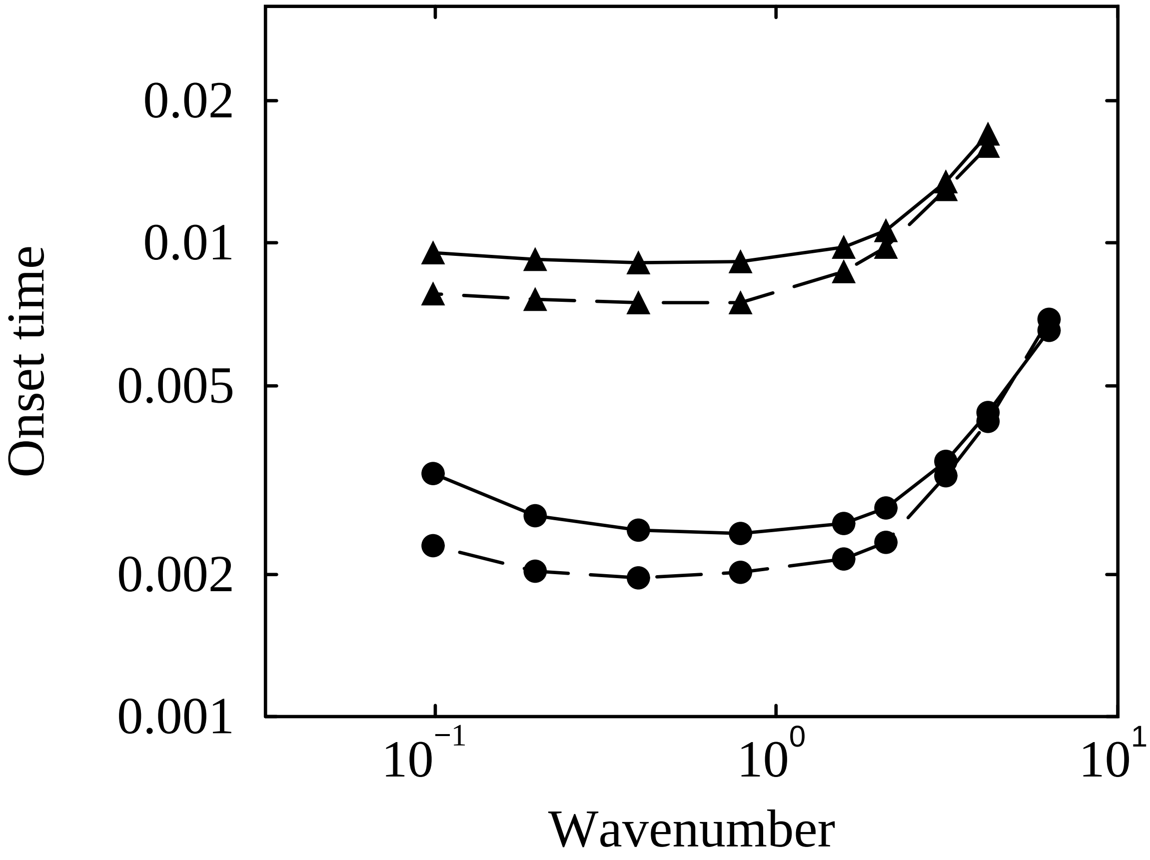

Figure 2.7: Theoretical predictions (solid lines) versus numerical results (dashed lines) for the growth rate of large-scale instability. Triangles correspond to $Ra = 3 \times 10^3$; circles correspond to $Ra = 10^4$.

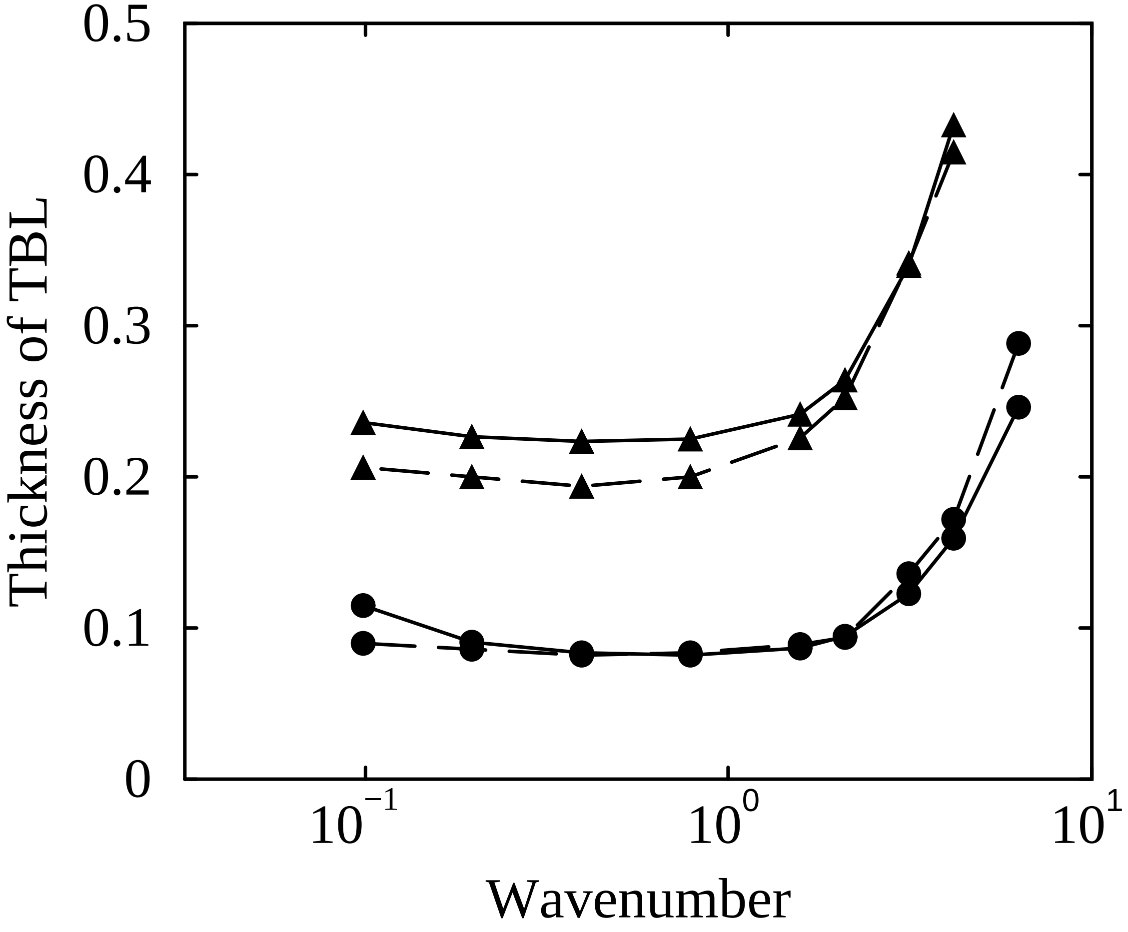

Figure 2.8: Theoretical predictions (solid lines) versus numerical results (dashed line) for the thickness of the thermal boundary layer at the onset time of plume formation. Triangles indicate $Ra = 3 \times 10^3$; circles indicate $Ra = 10^4$.

Chapter 3

Early transient superplumes and the origin of the Martian crustal dichotomy

Yun Ke and Slava Solomatov

Journal of Geophysical Research, 111, E10001, doi:10.1029/2005JE002631.

The large temperature difference between the core and mantle of Mars at the end of planetary accretion creates a hot, internally convecting thermal boundary layer at the base of the mantle, whose viscosity is several orders of magnitude lower than the viscosity of the mantle above it. Theoretical analysis and numerical simulations of the instability of this thermal boundary layer show that it is likely that only one large plume forms. This superplume may play a role in the formation of crustal dichotomy and generation of the magnetic field in the early history of Mars.

3.1 Introduction

The surface of Mars consists of a heavily cratered elevated southern hemisphere which occupies about 60% of the planet and a resurfaced depressed northern hemisphere which covers the remaining 40%. The southern hemisphere of Mars is several kilometers higher than the northern one with a small north to south slope and the maximum elevation difference of $\sim$ 6 km [*Smith et al.*, 1999]. Crustal models constrained by gravity and topography data indicate that the crust thins progressively from south to north [*Zuber et al.*, 2000]. Although the northern lowlands are not as heavily cratered as the southern highlands, the similarity between the size-frequency distribution of buried craters in the resurfaced northern lowlands and that of craters in the southern highlands suggests that both regions are roughly the same age and that resurfacing of only about 1 to 2 km thick layer took place later in planetary evolution [*Frey et al.*, 2002]. This implies that the dichotomy formed very early although the absolute age is uncertain. *Hartmann and Neukum* [2001] estimate an age of $\sim$ 3.9 Gyr, that is about $\sim$ 600 Myr after planetary accretion. The proposed mechanisms for the origin of crustal dichotomy include impacts [*Wilhelms and Squyres*, 1984; *Frey and Schultz*, 1988], mantle convection [*McGill and Dimitrou*, 1990; *Zhong and Zuber*, 2001], mantle overturn upon crystallization of a magma ocean [*Elkins-Tanton et al.*, 2005], and plate tectonics [*Sleep*, 1994; *Lenardic et al.*, 2004].

We propose a hypothesis that the dichotomy is caused by an early superplume produced by a hot Martian core. A classical plume theory based on constant viscosity models [e.g., *Whitehead and Luther*, 1975; *Campbell et al.*, 1990] would have difficulties in explaining the rapid formation of single plumes as it did in the case of Tharsis [*Schubert et al.*, 1990; *Harder and Christensen*, 1996; *Harder*, 1998; *Harder*, 2000; *Breuer et al.*, 1998; *Wenzel et al.*, 2004].

The factor which can play an important role is temperature-dependent viscosity which is known to substantially affect plume dynamics [*Loper and Stacey*, 1983; *Weinberg*, 1997; *Kellogg and King*, 1997; *van Keken*, 1997; *Schaeffer and Manga*, 2001; *Lithgow-Bertelloni et al.*, 2001]. In this paper, we focus on the regime where the viscosity contrast across the thermal boundary layer (TBL) at the base of the mantle is very large. This regime is transient in the sense that the large viscosity contrast across the bottom boundary layer can only occur when convection is not in thermal equilibrium, that is when heating is not in balance with cooling. In thermal equilibrium, the temperature difference in the bottom boundary layer of temperature-dependent viscosity fluids is controlled by the viscosity law in such a way as to maintain the viscosity contrast across the boundary layer at a factor of ~ 3 [*Morris and Canright*, 1984; *Fowler*, 1985]. For a terrestrial planet, this temperature difference is ~ 100 K.

Because the temperatures of the Martian core and mantle are established during planetary accretion and core formation, there is no reason for the initial temperature difference between the core and mantle be close to this value. When the temperature difference between the core and the mantle is so large that the viscosity contrast across the TBL exceeds $\sim 10^4$, instabilities develop within the boundary layer [*Yuen and Peltier*, 1980; *Christensen*, 1984; *Olson et al.*, 1987; *Thompson and Tackley*, 1998]. This regime has been described quantitatively by *Solomatov and Moresi* [2002] and *Ke and Solomatov* [2004], who demonstrated that the internally convecting TBL is separated from the upper region by a relatively sharp rheological boundary forming effectively a two-layer system. Plumes form as a result of Rayleigh-Taylor-like instability of the TBL, which tends to produce fewer and larger plumes. The goal of this study is to extend the 2-D analysis of *Ke and Solomatov* [2004] to 3-D spherical shell geometry and discuss the implications of this type of behavior for the origin of

Martian crustal dichotomy.

3.2 Model

We consider the mantle to be a spherical shell of density ρ_0, viscosity μ_0, and thickness $H = R_0 - R_c$, where R_c is the inner radius (the radius of the core-mantle boundary – CMB) and R_0 is the outer radius (planetary surface) (Fig. 3.1a). The boundaries are stress-free. Although the planetary surface is a stress-free boundary, the stiff lithosphere can make it effectively a no-slip boundary. On the other hand, an asthenosphere may decouple the lithosphere and the mantle making it effectively a stress-free boundary. In either case, the exact conditions near the planetary surface are not very important to the early stages of plume development.

Initially, the mantle has a constant temperature T_m and the CMB is held at $T_c = T_m + \Delta T$. At time $t > 0$, a TBL is developed at the bottom of the mantle. We assume that the viscosity contrast across the TBL is larger than $\sim 10^4$ so that convection begins within the TBL [*Solomatov and Moresi*, 2002].

When small-scale convection starts, the temperature distribution inside the TBL changes from a conductive profile to a convective profile [*Solomatov and Moresi*, 2002]. In the first approximation it can be considered as a nearly isothermal and isoviscous layer. The mantle can then be approximated as two uniform layers with different viscosities and densities (Fig. 3.1a).

With these simplifications, large-scale instability of the mantle behaves essentially as a Rayleigh-Taylor instability, except that the boundary between the layers propagates upward. The amplitude ξ_0 of a small initial perturbation of the interface would grow exponentially with time:

$$\xi = \xi_0 \exp{(st)}\,, \tag{3.1}$$

where s is the growth rate, eventually forming plumes (Fig. 3.1b).

3.3 Viscosity

The viscosity is assumed to be controlled by diffusion creep and is described by an Arrhenius function of temperature [*Karato and Wu*, 1993]:

$$\mu = \frac{G}{2A}\left(\frac{h}{b^*}\right)^m \exp\left(\frac{Q}{RT}\right), \tag{3.2}$$

where A is a constant, G is the shear modulus, b^* is the Burgers vector, R is the universal gas constant and Q is the activation enthalpy. The activation enthalpy is estimated from $Q = E^* + P_c V^*$ where E^* is the activation energy, V^* is the activation volume, and P_c is the hydrostatic pressure at the core-mantle boundary.

3.4 Nondimensional parameters

To non-dimensionalize the problem, we choose the thickness $H = R_0 - R_c$ of the mantle (including the TBL) as the length scale, $t_0 = H^2/\kappa$ as the time scale, $u_0 = H/t_0$ as the velocity scale, and $\Delta T = T_c - T_m$ as the temperature scale, where $\kappa = k/\rho_0 c_p$ is the thermal diffusion coefficient, k is the thermal conductivity, and c_p is the isobaric specific heat.

It is convenient to introduce two Rayleigh numbers: the mantle Rayleigh number

$$Ra_0 = \frac{\alpha \rho_0 g \Delta T H^3}{\kappa \mu_0}, \tag{3.3}$$

and the Rayleigh number at the core-mantle boundary:

$$Ra_1 = \frac{\alpha \rho_0 g \Delta T H^3}{\kappa \mu_c}, \tag{3.4}$$

where α is the thermal expansion coefficient, g is the acceleration due to gravity, and μ_c is the bottom viscosity (at the core-mantle boundary temperature T_c).

Other dimensionless parameters are: the ratio $c = R_c/R_0$ between the core radius and the planetary radius, and the ratio $\epsilon = h/R_c$ between the thickness of the TBL and the core radius.

3.5 Small-scale convection

According to the half space heating model [*Turcotte and Schubert*, 2002] the nondimensional temperature gradient at the core-mantle boundary changes with time as $(\pi t)^{-1/2}$. The corresponding thickness of the TBL is:

$$d = (\pi t)^{1/2}. \tag{3.5}$$

Small-scale convection starts when the TBL reaches the critical thickness d_{cr} (Fig. 3.2a) [*Stengel et al.*, 1982; *Solomatov*, 1995]:

$$d_{cr}^3 = \frac{20.9\theta^4}{Ra_1}, \tag{3.6}$$

where

$$\theta = \gamma \Delta T, \tag{3.7}$$

and

$$\gamma = \frac{Q}{RT_c^2}. \tag{3.8}$$

This gives the time t_{ss} at the onset of small-scale convection:

$$t_{ss} = \pi^{-1} d_{cr}^2 = 2.4 \left(\frac{\theta^4}{Ra_1} \right)^{2/3}. \tag{3.9}$$

The initial thickness of the convective sublayer is (Fig. 3.2b) [*Stengel et al.*, 1982]

$$h_0 = \left(\frac{8}{\theta} \right) d_{cr} = 22 \left(\frac{\theta}{Ra_1} \right)^{1/3}. \tag{3.10}$$

Thus the initial thickness ratio ϵ_0 is (for $c \approx 0.5$)

$$\epsilon_0 = \frac{h_0}{R_c} = 22 \left(\frac{\theta}{Ra_1} \right)^{1/3}. \tag{3.11}$$

The temperature of the convective layer is [*Solomatov and Moresi*, 2002]

$$T_1 = 1 - \frac{1.1}{\theta}, \tag{3.12}$$

and the viscosity contrast between the layers is

$$\Delta\mu = \frac{\mu_0}{\mu_1} = \exp\left[\frac{Q(T_1 - T_m)}{RT_m T_1} \right]. \tag{3.13}$$

After the onset of small-scale convection, the heat flux at the bottom is

$$F = a\theta^{-4/3} Ra_1^{1/3}, \tag{3.14}$$

where the coefficient $a \sim 0.4 - 0.7$ depends on the geometry and the heating mode

[*Solomatov and Moresi*, 2000, 2002; *Reese et al.*, 2005]. We will use $a = 0.5$. This value was suggested by numerical simulations of a similar problem in 2-D [*Solomatov and Moresi*, 2000] and is also in agreement with the 3-D simulations described below.

The convecting TBL grows at an approximately constant rate [*Solomatov and Moresi*, 2002]:

$$\dot{h} = v_h = \frac{F}{T_1}. \tag{3.15}$$

3.6 Large-scale instability

In a previous study [*Ke and Solomatov*, 2004] we obtained scaling relationships for large-scale instability in a two-dimensional Cartesian geometry. Our results show that at large viscosity contrasts the plume formation can approximately be described as Rayleigh-Taylor instability.

Similar scaling relationships for a spherical shell can be obtained using (i) the scaling laws for small-scale convection in a spherical shell and (ii) the solution for Rayleigh-Taylor instability in a spherical shell. Scaling laws for 2D and 3D small-scale convection are very similar [*Solomatov and Moresi*, 2000; *Reese et al.,* 2005] but the solutions for Rayleigh-Taylor instability in a spherical shell geometry appear very different from those in a two-dimensional box. Below we analyze the 3-D solutions for Rayleigh-Taylor instability to relate 2-D and 3-D solutions and obtain scaling laws for plume formation in a spherical shell geometry.

3.6.1 Ribe and De Valpine's [1994] solution

The analytical solution for Rayleigh-Taylor instability in a spherical shell geometry was obtained in the "thin layer" limit ($\epsilon l \ll 1$) by *Ribe and De Valpine* [1994]. The non-dimensional instability growth rate is

$$s = \frac{H^2}{\kappa}\frac{\Delta\rho g h}{\mu_1}\tilde{s} = \left(\frac{c\epsilon\Delta\mu}{1-c}\right) Ra_0\tilde{s}, \tag{3.16}$$

where $\tilde{s}$ is

$$\tilde{s} = \frac{\epsilon l(l+1)(F_1 + \epsilon\Delta\mu F_2)}{c(\Delta\mu F_3 + \epsilon F_4 + \epsilon^3\Delta\mu^2 F_5)}, \tag{3.17}$$

l is the spherical harmonic degree of the perturbation, and the coefficients F_i are algebraic functions of $c = R_c/R_0$ and l [*Ribe and De Valpine*, 1994]. For each l there are $2l+1$ degenerate modes ($m = -l, ..., -1, 0, +1, ..., l$).

Figure 3.3 shows the growth rate as a function of spherical harmonic degree at different viscosity contrasts for $c = 0.5$ and $\epsilon = 0.05$. As the viscosity contrast increases, the lower harmonic degree perturbations grow faster. However, one can see that the difference in growth rates between $l = 1$ and $l = 2$ is small. This suggests that the initial amplitude of the perturbation may control how many plumes will be formed.

3.6.2 Comparison of linear regimes between 2-D and 3-D

To compare 2-D and 3-D solutions, we first compare the non-dimensional parameters of the 3-D model with those of the 2-D model in Table 3.1. For $1 \ll l \ll \epsilon^{-1}$, using normalized wavenumber $K_s = 2\epsilon l$, Eq. (3.17) can be simplified as

$$\tilde{s} = \frac{3K_s + \Delta\mu {K_s}^2}{12\Delta\mu + 12K_s + \Delta\mu^2 {K_s}^3}. \tag{3.18}$$

For the perturbations with short wavelength ($K_s \gg max(\epsilon, \Delta\mu^{-1/3})$), the motion of interface is vertical and the growth of the instability is limited by the normal stresses

Table 3.1: Comparison of controlling parameters in 2-D and 3-D

Parameters	2-D	3-D
Viscosity contrast	μ_0/μ_1	μ_0/μ_1
Thickness ratio *	$\beta = \frac{H-h}{h}$	$\frac{H-h}{h} \approx \epsilon^{-1}$
Perturbation wavelength	λ	$\lambda_s = 2\pi R_c/l$
Perturbation wavenumber	$k = 2\pi/\lambda$	$k_s = l/R_c$
Normalized wavenumber	$K = 2kh$	$K_s = 2k_s h = 2\epsilon l$

---

* $\frac{H-h}{h} = \left(\frac{1-c}{c}\right)\epsilon^{-1} - 1 \approx \epsilon^{-1}$, when $c \approx 0.5$ and $\epsilon \ll 1$.

in the more viscous upper layer. The growth rate $\tilde{s} \approx 1/\Delta\mu K_s$, which decreases with increasing wavenumber (Regime III in Fig. 3.4b). This regime also includes the region $l > \epsilon^{-1}$.

In another regime ($\Delta\mu^{-1} \ll K_s \ll \Delta\mu^{-1/3}, 1 \ll \Delta\mu \ll \epsilon^{-3}$), the wavelength of the perturbation is long compared to the bottom layer, thus the primary motion of the interface is horizontal and limited by shear stresses. The conductive region is relatively immobile and the shear in the bottom layer limits the growth rate $\tilde{s} \approx {K_s}^2/12$ (Regime II in Fig. 3.4b).

In the last regime ($\epsilon \ll K_s \ll \Delta\mu^{-1}$), the slight resistance of the upper layer gives a small shear gradient across the bottom layer, which can balance the buoyancy and give the growth rate $\tilde{s} \approx K_s/4\Delta\mu$ (Regime I in Fig. 3.4b).

The regime diagram for the spherical shell geometry (Fig. 3.4b) is similar to the top-right part ($\Delta\mu > 1$, $K > \beta^{-1}$) of the 2-D regime diagram (Fig. 3.4a). The asymptotic growth rates including the numerical coefficients are also the same. This similarity makes the extension of the 2-D scaling laws to 3-D spherical geometry relatively straightforward.

3.6.3 The fastest growing mode

In linear theory, the fastest growing mode determines how many plumes are generated. The spherical harmonic degree l of this mode is equal to the number of plumes. When $\Delta\mu > \epsilon^{-3}$, the growth rate of the instability decreases monotonically with increasing harmonic degree l (Fig. 3.4b). In this case, the degree-1 mode (one plume) is the fastest growing mode. When $\Delta\mu < \epsilon^{-3}$, the instability growth rate increases with l in regimes I and II, and decreases in regime III. Therefore, the mode with the maximum growth rate is located on the boundary separating regimes II and III (Fig. 3.4b), which can be used to determine the number of plumes for $\Delta\mu < \epsilon^{-3}$. Thus, the general formula for the spherical harmonic degree of the fastest growing mode (the number of plumes) is

$$l_{max} = \begin{cases} 1 & \text{if } \Delta\mu > \epsilon^{-3}, \\ \epsilon^{-1}\Delta\mu^{-1/3} & \text{if } 1 < \Delta\mu < \epsilon^{-3}. \end{cases} \tag{3.19}$$

For the fastest growing mode equations (3.16) and (3.17) give

$$s = \left(\frac{c}{1-c}\right)\frac{Ra_0}{2l_{max}}. \tag{3.20}$$

3.6.4 Plume formation

The onset time of plume formation is defined by the requirement that [*Ke and Solomatov*, 2004]

$$\dot{\xi} = v_h. \tag{3.21}$$

From Eq. (3.1) the onset time of plume formation is

$$t_p = t_{ss} + \tau \ln\left(\frac{\delta}{\xi_0}\right), \tag{3.22}$$

where τ is the time scale for plume formation,

$$\tau = s^{-1} = \frac{2l_{max}}{Ra_0}, \tag{3.23}$$

and δ is a characteristic thickness

$$\delta = \frac{v_h}{s} = \frac{2l_{max}F}{Ra_0 T_1}. \tag{3.24}$$

The thickness of the convecting TBL at the time when plumes form is

$$h_p = h_0 + v_h(t_p - t_{ss}) = h_0 + \delta \ln\left(\frac{\delta}{\xi_0}\right). \tag{3.25}$$

3.7 Summary of scaling relationships in dimensional form

The large viscosity contrast regime of plume formation involves small-scale convection in the TBL, growth of the TBL, and large-scale instability of the TBL. This regime takes place when the viscosity contrast across the TBL satisfies the condition:

$$\frac{\mu_0}{\mu_c} = \exp\left(\frac{Q\Delta T}{RT_m T_c}\right) > 10^4. \tag{3.26}$$

Small-scale convection begins when the TBL reaches the critical thickness

$$d_{cr} = 2.75\theta^{4/3}\left(\frac{\kappa\mu_c}{\alpha\rho_0 g\Delta T}\right)^{1/3}, \tag{3.27}$$

and occurs at time

$$t_{ss} = \pi^{-1} d_{cr}^2 \tag{3.28}$$

The thickness of the convecting TBL at the onset of small-scale convection is

$$h_0 = 22\theta^{1/3} \left(\frac{\kappa \mu_c}{\alpha \rho_0 g \Delta T} \right)^{1/3}, \tag{3.29}$$

and the interior temperature in the convecting TBL is

$$T_1 = T_m + \left(1 - \frac{1.1}{\theta} \right) \Delta T. \tag{3.30}$$

The heat flux at the CMB is

$$F = 0.5 k \gamma^{-4/3} \left(\frac{\alpha \rho_0 g}{\kappa \mu_c} \right)^{1/3}. \tag{3.31}$$

The boundary of the convective region propagates upward with the velocity

$$v_h = \frac{F}{\rho c_p (T_1 - T_m)} \tag{3.32}$$

The spherical harmonic degree of the fastest growing mode (the number of plumes) is

$$l_{max} = \begin{cases} 1 & \text{if } \Delta\mu > \epsilon_p^{-3}, \\ \epsilon_p^{-1} \Delta\mu^{-1/3} & \text{if } 1 < \Delta\mu < \epsilon_p^{-3}, \end{cases} \tag{3.33}$$

where $\epsilon_p = h_p / R_c$ and its growth rate is (for $c = R_c / R_0 \approx 0.5$):

$$s \approx \frac{\alpha \rho_0 g \Delta T H}{2 l_{max} \mu_0}. \tag{3.34}$$

The onset time of plume formation is

$$t_p = t_{ss} + \tau \ln \left(\frac{\delta}{\xi_0} \right), \tag{3.35}$$

where $\tau = s^{-1}$ and $\delta = v_h \tau$ and the thickness of the convecting TBL at $t = t_p$ is

$$h_p = h_0 + v_h (t_p - t_{ss}). \tag{3.36}$$

Below we perform numerical simulations and compare the numerical results with the predictions of our scaling theory.

3.8 Numerical simulations

The goal of the numerical simulations presented in this section is to test the linear theory that describes the large-scale instability. The mathematical formulation is exactly the same as described earlier. Some of the simulations extend well beyond the linear stage. Although they help to visualize the plume structure, they are not designed to study long-term dynamics such as plume-lithosphere interaction (note that the cold thermal boundary layer is absent in the model because the surface temperature, $T_s = 0$, is the same as the initial temperature of the mantle) or to study multiple plume events (the model does not take into account core cooling or radiogenic heating which are important in long-term evolution).

The nondimensional equations of thermal convection in the Boussinesq approximation are

$$\nabla \cdot \mathbf{u} = 0, \tag{3.37}$$

$$0 = -\nabla p + \alpha \rho g T \mathbf{n} + \nabla \cdot [\mu(\nabla \mathbf{u} + \{\nabla \mathbf{u}\}^T)], \tag{3.38}$$

$$\frac{\partial T}{\partial t} + \mathbf{u} \cdot \nabla T = \nabla^2 T. \tag{3.39}$$

where $\mathbf{u}$ is the velocity vector, p and T are the pressure and temperature perturbations, $\mathbf{n}$ is a unit vector in the direction of gravity, and $\{\}^T$ is the transpose operator.

The numerical simulations are performed using parallelized finite element code CITCOMS [*Zhong et al.*, 2000]. The spherical shell has 64 elements in the radial direction with finite elements approximately equidimensional near the core-mantle boundary. The total number of elements is 64 × 64 × 64 × 12. This is half the resolution of our 2-D simulations [*Ke and Solomatov*, 2004] (128 elements in the vertical direction).

The viscosity is an exponential function of temperature (Frank-Kamenetskii approximation) and the viscosity contrast across the bottom TBL is $\Delta\mu = 10^6$. Although this is very different from the Arrhenius function, the scaling laws depend only on the viscosity contrast $\Delta\mu$ and the Frank-Kamenetskii parameter θ.

To resolve small-scale convection, the Rayleigh number $Ra_0 = 1.25 \cdot 10^3$ is lower than used by *Ke and Solomatov* [2004]. Note that despite the spherical geometry we define the Rayleigh number by Eq. (3.3) so that it can approximately be compared with its 2-D counterpart. The Rayleigh number which is more appropriate for characterizing small-scale convection inside the TBL is $Ra_{\mathrm{TBL}} = Ra_1 h^3 = \Delta\mu Ra_0 h^3$. It varies from $\sim 10^5$ during the linear plume growth to $\sim 10^9$ in the well developed stage.

To initiate large-scale instability we impose a temperature perturbation in the form of a single spherical harmonic function of degree l with $m = l$ and amplitude 1%, multiplied by a sine function in radial direction, so that the perturbation vanishes at the boundaries. The perturbation with $m = l$ produces plumes along the equator.

The snapshots of our numerical simulations for $l = 1$ and 2 are shown in Fig. 3.5. The thickness of the convecting TBL (defined by the isotherm $T_L = 0.6$) and the amplitude of the instability for $l = 1$, 2, 3, 4 and 5 are shown in Fig. 3.6. The propagation speed of the convective layer is approximately constant (it would eventually slow down because of the spherical geometry) while the instability grows exponentially with time.

Figure 3.7a shows the growth rate, s, as a function of harmonic degree l. The theoretical growth rate is calculated using Eqs. (3.16) and (3.17) assuming a constant value of $\epsilon = h/R_c \approx h_0/r_1$. Although h changes during evolution, the small variation in h after the onset of convection and the weak dependence of function (3.16) on h allows us to use a constant value $h = h_0$. The numerical results agree reasonably well with the theory.

The onset time of plume formation, t_p, is calculated using equations (3.22)-(3.24). The largest contribution to t_p comes from t_{ss} (it takes much longer for small-scale convection to start than for plume to develop). After the onset of small-scale convection, the temperature profile becomes near isothermal, which roughly doubles the buoyancy of the TBL and the average viscosity of the TBL drops by several orders of magnitude. These changes significantly accelerate the growth of the large-scale instability. Thus, the onset of small-scale is effectively the beginning of the Rayleigh-Taylor instability.

The discrepancy between the theoretical and the numerical curves in Fig. 3.7b may be due to various factors. Perhaps, the most important one is that Eq. (3.6) describes the onset of convection in a layer with non-moving boundaries [*Stengel et al.*, 1982] and thus, can only approximately predict the onset of convection in the TBL. Furthermore, Eq. (3.6) is based on a linear theory. A non-linear theory [*Solomatov and Barr*, 2006], gives noticeably different criteria. Figure 3.7c shows the thickness of the TBL, h_p, at the onset time of plume formation, $t = t_p$. The theoretical curve is calculated using Eq. (3.25).

Table 3.2: Physical parameters

Parameter	Value	Reference
Planetary mass, M	$6.4 \cdot 10^{23}$ kg	1
Gravity, g	3.7 m s^{-2}	1
Planetary radius, R_0	3390 km	1
Mantle density, ρ	4000 kg m^{-3}	1
Core radius, R_c	1700 km	2
Core mass, M_c	$1.4 \cdot 10^{23}$ kg	3
Pressure at CMB, P_c	23 GPa	3
Mantle specific heat, C_p	1200 J kg^{-1} K^{-1}	1
Core specific heat, C_{pc}	800 J kg^{-1} K^{-1}	4
Thermal expansion, α	$2 \cdot 10^{-5}$ K^{-1}	5
Thermal conductivity, k	4 W m^{-1} K^{-1}	6
Viscosity law constant, A	$5.3 \cdot 10^{15}$ s^{-1}	7
Activation energy, E^*	240 kJ mol^{-1}	7
Activation volume, V^*	$5 \cdot 10^{-6}$ m^3 mol^{-1}	7
Grain size, h	10^{-3} m	7
Grain size exponent, m	2.5	7
Burgers vector, b^*	$5 \cdot 10^{-10}$ m	7

(1)*Zharkov* [1986], (2)*Yoder et al.* [2003], (3)*Longhi et al.* [1992],
(4)*Anderson* [1995], (5)*Chopelas* [1996], (6)*Hofmeister* [1999],
(7)*Karato and Wu* [1993].

3.9 Implications for Mars

3.9.1 Initial temperatures of the core and mantle

Whether or not transient superplumes occurred on Mars depends on the rheology and the initial temperatures of the core and mantle. Figure 3.8 summarizes the range of temperatures at which the formation of superplumes occurs for diffusion creep in wet olivine [*Karato and Wu*, 1993] (the values of all physical parameters are given in Table 3.2) and shows how the spherical degree l of the most unstable mode (the number of superplumes) varies with temperature. For the range of mantle temperatures between 1300 and 1800 K, the core-mantle temperature difference required for the formation of one superplume is between 500 and 1500 K.

Are these temperatures realistic? Unfortunately, the initial temperatures of Mars and especially the temperature difference between the core and mantle are poorly constrained. On Earth, the temperature of the lower mantle is around 2800 K and the temperature difference between the core and the lower mantle in the present-day Earth is 1000-2000 K [*Boehler*, 1996, 2000; *Williams*, 1998]. Thermal evolution models indicate that in the past the core-mantle temperature difference is likely to be larger [*Stevenson et al.*, 1983].

The impacts of large differentiated bodies at the end of accretion could have played a key role in generating a large temperature difference between the core and the mantle. Recent simulations of the collision of large differentiated bodies with the proto-Earth during the late stages of accretion [*Canup*, 2004] indicate that the material that is heated the most (to more than 10^4 K) is the iron core of the impactor. The hot iron from the impactor accumulates in the upper part of the Earth's core, where it is gravitationally stable. The temperature of the coldest mantle material is

$\sim$ 2000 K while the temperature of the hottest mantle material $\sim 10^4$ K. Although *Canup*'s [2004] simulations look only at the first days of impact dynamics, it is clear that the coldest mantle material will eventually accumulate at the base of the mantle while the molten parts of the lower mantle will crystallize and cool down to near-solidus temperatures, 4000 – 5000 K [*Holland and Ahrens*, 1997; *Zerr et al.*, 1998] within $\sim 10^3$ years [*Solomatov*, 2000]. This is very fast compared to the growth of the thermal boundary layer (10^8 years). Although detailed models of these processes are yet to be developed, it seems that at the end of accretion and core formation, the Earth's core may be hotter than the base of the mantle by as much as $\sim$ 5000 K.

Mars is a smaller planet and core formation on Mars is less energetic than on Earth [e.g., *Solomon*, 1979]. Thus, one might expect a smaller core-mantle temperature difference. For example, a comparison of the accretion energies of Mars and Earth, which scales as M/R, shows that the accretion energy of Mars is about 1/5 of the accretion energy of Earth. Assuming a linear relationship between the accretion energy and the core-mantle temperature difference (the actual scaling law is unknown) the core-mantle temperature difference on early Mars can still be quite large ($\sim$ 1000 K).

Another simple constraint on the temperature difference between the core and the mantle can be obtained from the assumption that the energy of core formation is retained within the segregated iron [*Stevenson*, 2001]. If all of the energy of core formation [*Solomon*, 1979] goes to the core alone, this can give over 1000 K increase in the temperature of the core.

Numerical simulations of accretion predict a rather cold interior of Mars, about several hundred degrees Kelvin near the center of the planet [*Senshu et al.*, 2002]. In these models, liquid iron forms a layer at some depth and sinks toward the center of the planet as a result of Rayleigh-Taylor instability [*Elsasser*, 1963; *Kaula*, 1979; *Stevenson*, 1981, 1990; *Ida et al.*, 1987; *Honda et al.*, 1993]. The instability of the liquid iron layer may occur relatively late in Mars' history ($\sim$ 500 Myr) because the cold interior needs to be heated up to allow viscous creep [*Senshu et al.*, 2002]. However, the stresses generated by iron blobs can exceed the "ultimate" strength of rocks, in which case the instability can be extremely fast [*Davies*, 1982; *Tonks and Melosh*, 1992]. If very little heat exchange occurs between the hot liquid iron diapirs and the cold surrounding mantle, then the temperature of the core approximately corresponds to the temperature of the impact-generated liquid iron. It is poorly constrained but in any case it must exceed the eutectic temperature of iron-sulfur mixture $\sim$ 1300 K [*Boehler*, 1992; *Poirier*, 1994; *Fei et al.*, 1997]. Since the "lower mantle average" temperature is $\sim$ 900 K the initial core-mantle temperature difference is at least $\sim$ 400 K.

Senshu et al.'s [2002] models do not take into account heating of planetesimals by short-lived isotopes such as ^{26}Al and ^{60}Fe [*Urey*, 1955; *Shukolyukov and Lugmair*, 1993; *Srinivasan et al.*, 1999; *Yoshino et al.*, 2003; *Mostefaoui et al.*, 2005] which can substantially increase the mantle temperature. Also, these models do not consider the role of large differentiated impactors which can deposit a substantial fraction of their energy into the deep parts of the mantle [*Reese et al.*, 2006] and can contribute their hot cores directly to the core of proto-Mars as it was shown for the Earth [*Canup*, 2004]. Besides, a cold mantle is difficult to reconcile with Hf-W isotopic data which indicate that metal-silicate segregation took less than 15 Myr [*Kleine et al.*, 2004]. This requires a partially molten mantle, although *Senshu et al.* [2002] argued that melting of only an upper part of mantle would be consistent with Hf-W systematics. Shallow melting in the Martian mantle is also supported by estimates of metal-silicate equilibrium pressures (about 7.5 GPa) constrained by the abundances of siderophile elements [*Righter*, 2003]. Given the uncertainties, one can consider an end-member model in which early Mars had a global magma ocean [*Elkins-Tanton et al.*, 2005]. In this scenario, crystallization of a Martian magma ocean creates an unstable density stratification which causes mantle overturn. The overturn replaces an initially hot lower mantle material ($\sim$ 2400 K) by a relatively cold material ($\sim$ 1400 K) establishing a core-mantle temperature difference of $\sim$ 1000 K. Thus, even in this case, it is possible that a large core-mantle temperature difference was established at the end of planetary accretion.

It is possible that the initial core-mantle boundary temperature was so high that it exceeded the solidus. In this case, the thermal boundary layer at the base of the mantle would be partially molten. Our model does not take this effect into account. It would be interesting to consider this problem in the future.

3.9.2 Estimates for Martian superplume

Figure 3.9 shows the parameters of the superplume on early Mars, including the characteristic time of plume formation, the thickness of the convecting TBL at the time of plume formation, the heat flux at the core-mantle boundary and the temperature change of the core at the onset time of plume formation as a function of mantle viscosity. For example, if the mantle viscosity is $10^{21} - 10^{23}$ Pa s and the core-mantle temperature difference is $\sim$ 1000 K, the superplume forms within $10 - 1000$ Myr of evolution depending on mantle viscosity.

The enormous size and rapid formation of plumes such as those shown in Fig. 3.5 may cause planetary-scale melting of Mars and produce the crustal dichotomy early in Mars' evolution. The core temperature drop ΔT_c caused by one superplume is on the order of 100 to 1000 K (Fig. 3.9d). Because our models do not take into account the change in the core temperature, it is simply scaled as $\Delta T_c = A_c F t_p / C_{pc} M_c$ where $A_c = 4\pi R_c^2$ is the surface area of the core-mantle boundary, M_c is the mass of the core and C_{pc} is the specific heat of the core. This estimate shows that subsequent plumes (if there will be any) will be much weaker and they will form in a small viscosity contrast regime. Thus, the single transient superplume can be a mechanism for the formation of crustal dichotomy in addition to impacts [*Wilhelms and Squyres*, 1984; *Frey and Schultz*, 1988], mantle convection [*McGill and Dimitrou*, 1990; *Zhong and Zuber*, 2001], mantle overturn upon crystallization of a magma ocean [*Elkins-Tanton et al.*, 2005] and plate tectonics [*Sleep*, 1994; *Lenardic et al.*, 2004].

3.9.3 Comparison with Zhong and Zuber [2001]

Among the other models proposed for the formation of crustal dichotomy, *Zhong and Zuber*'s [2001] model is the most similar to ours. The mechanism they propose involves Rayleigh-Taylor instability of the asthenosphere-mantle two-layer system and they also noticed that at large viscosity contrasts between the layers the number of "plumes" can be as low as one. The major difference between *Zhong and Zuber*'s [2001] model and our model is the origin of the instability – in their model it arises from the density difference between the asthenosphere and the rest of the mantle, while in our case, it arises from a hot bottom thermal boundary layer generated by the initially hot Martian core. Also, from a fluid dynamical point of view, our problem is different from that of *Zhong and Zuber* [2001] and also from the classical Rayleigh-Taylor instability problem because the boundary between the two layers in our model propagates upward. Thus, the growth of large-scale instability has to compete with the propagation of the TBL and is essentially coupled with small-scale convection inside the TBL.

3.9.4 Magnetic field

Observational data suggest that Mars had an early dynamo that is believed to exist in the first ~ 500 Myr of evolution [*Acũna et al.*, 1999]. A temporary episode of plate tectonics [*Nimmo and Stevenson*, 2000] or a mantle overturn [*Elkins-Tanton et al.*, 2005] could generate a high heat flux from the core and maintain the dynamo. An interesting consequence of a transient superplume is a large heat flow at the core-mantle boundary (Fig. 3.9c). It substantially exceeds the adiabatic heat flux $F_a \sim 20$ mW m^{-2} in the liquid outer core [*Stevenson et al.*, 1983; *Nimmo and Stevenson*, 2000; *Williams and Nimmo*, 2004] and thus, allows generation of the magnetic field early in the Martian history.

3.10 Conclusion

We have extended *Ke and Solomatov*'s [2004] theory describing plume formation in the internally convecting thermal boundary layer at the base of the mantle to 3-D spherical shell geometry and supported our scaling laws with the help of numerical simulations. The number of plumes and the rate of their development can vary substantially depending on the values of physical parameters and the temperatures of the core and the mantle. Application of these scaling relationships to Mars shows that if at the end of planetary accretion, the Martian core was ~ 1000 K hotter than the mantle, one large plume ("superplume") may form. Its development can be very fast, on the order of 10 to 1000 Myr depending on the value of mantle viscosity. We suggest that this transient superplume may play a role in the formation of crustal dichotomy and generation of magnetic field early in the history of the planet.

3.11 Acknowledgments

We thank Paul Tackley, Shijie Zhong, and the Associate Editor Francis Nimmo for their thorough and constructive reviews which led to a substantial rewriting of the manuscript. We also thank Amy Barr for her thoughtful comments and help in improving the presentation. This work was supported by the NASA grants NNG05GM17G and NNG05GM51G.

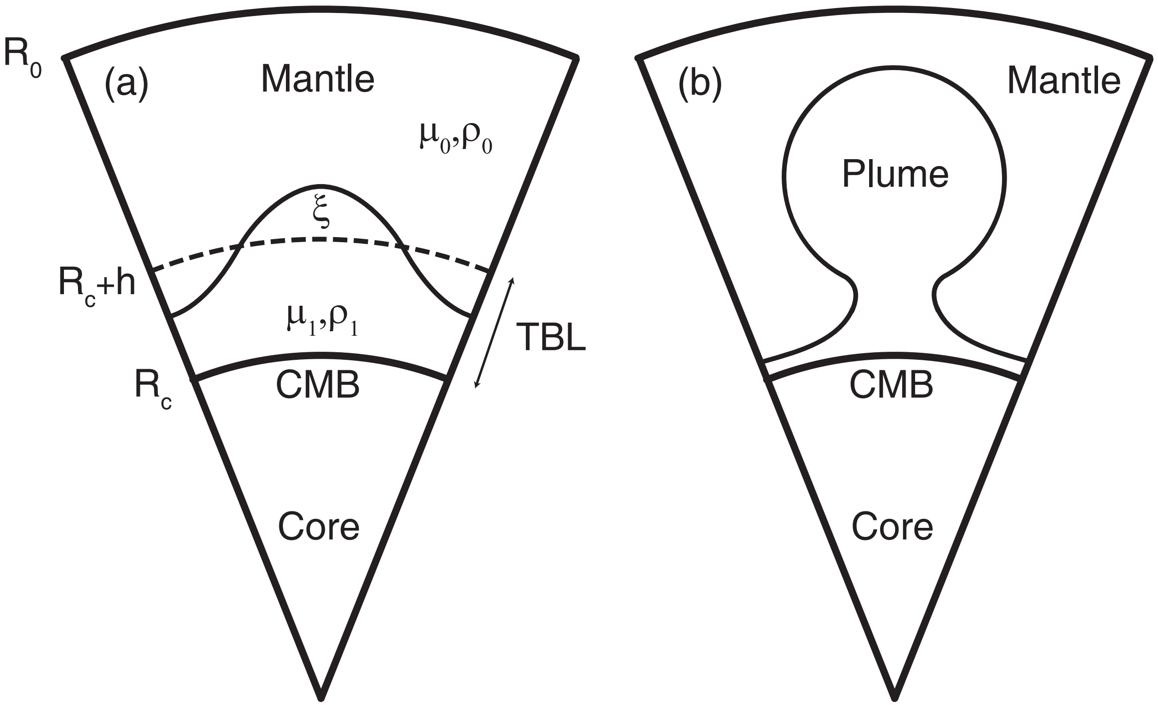

Figure 3.1: (a) The schematics of the model. The top and bottom boundaries of the mantle are stress-free. The inner radius of the spherical shell is R_c and the outer radius is R_0. The thickness of the convecting TBL is h. The amplitude of large-scale perturbation is ξ. The viscosity and density of the mantle are μ_0 and ρ_0. The viscosity and density of the internally convecting TBL are $\mu_1 < \mu_0$ and $\rho_1 < \rho_0$. (b) The plume formed by the large-scale perturbation.

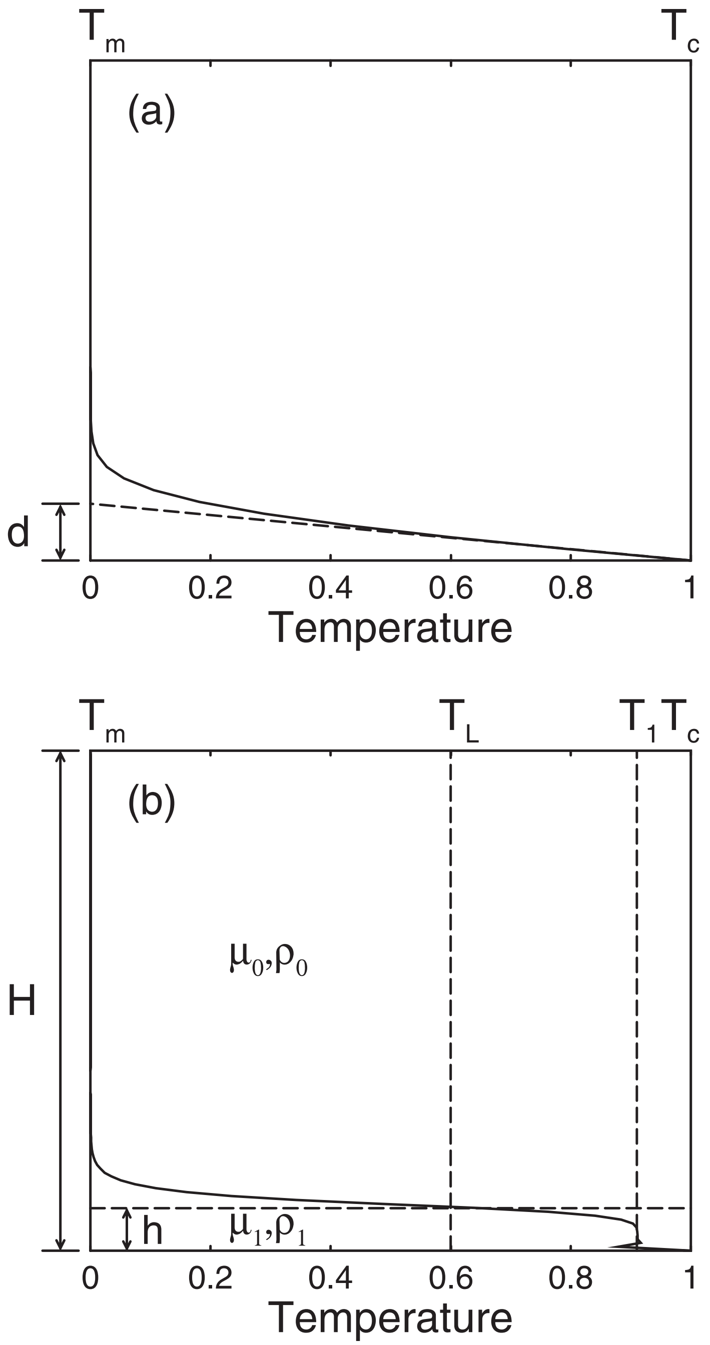

Figure 3.2: (a) The schematics of temperature distribution in the thermal boundary layer before the onset of small-scale convection. (b) The schematics of temperature distribution in the thermal boundary layer after the onset of small-scale convection. The thickness of the entire layer is $H = R_0 - R_c$. The thickness h of the boundary layer is determined by the isotherm $T = T_L = 0.6$ (non-dimensional temperature). The internal temperature of the boundary layer is T_1. The bottom temperature (at the core-mantle boundary) is $T_c = 1$. The mantle temperature is $T_m = 0$.

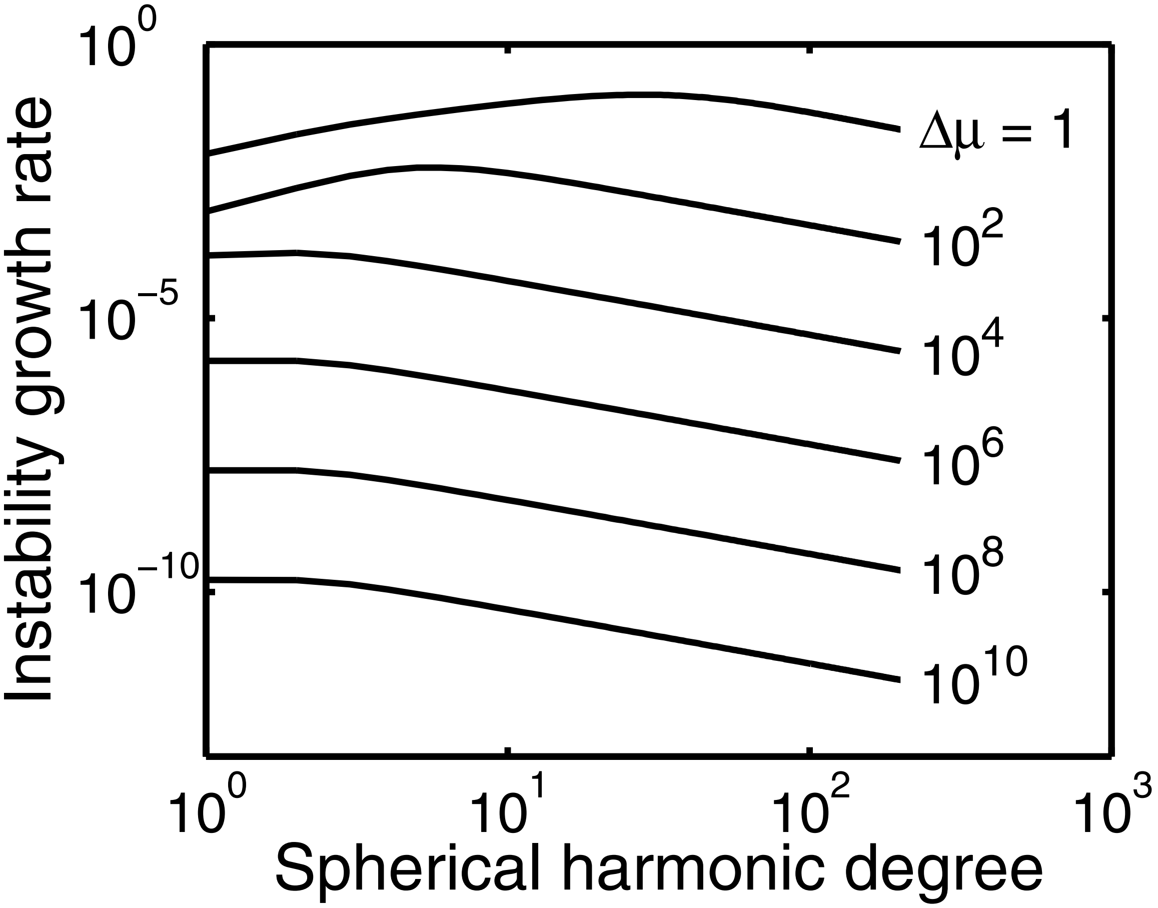

Figure 3.3: The instability growth rate $\tilde{s}$ as a function of spherical harmonic degree l at different viscosity contrasts $\Delta\mu$ for $c = 0.5$ and $\epsilon = 0.05$.

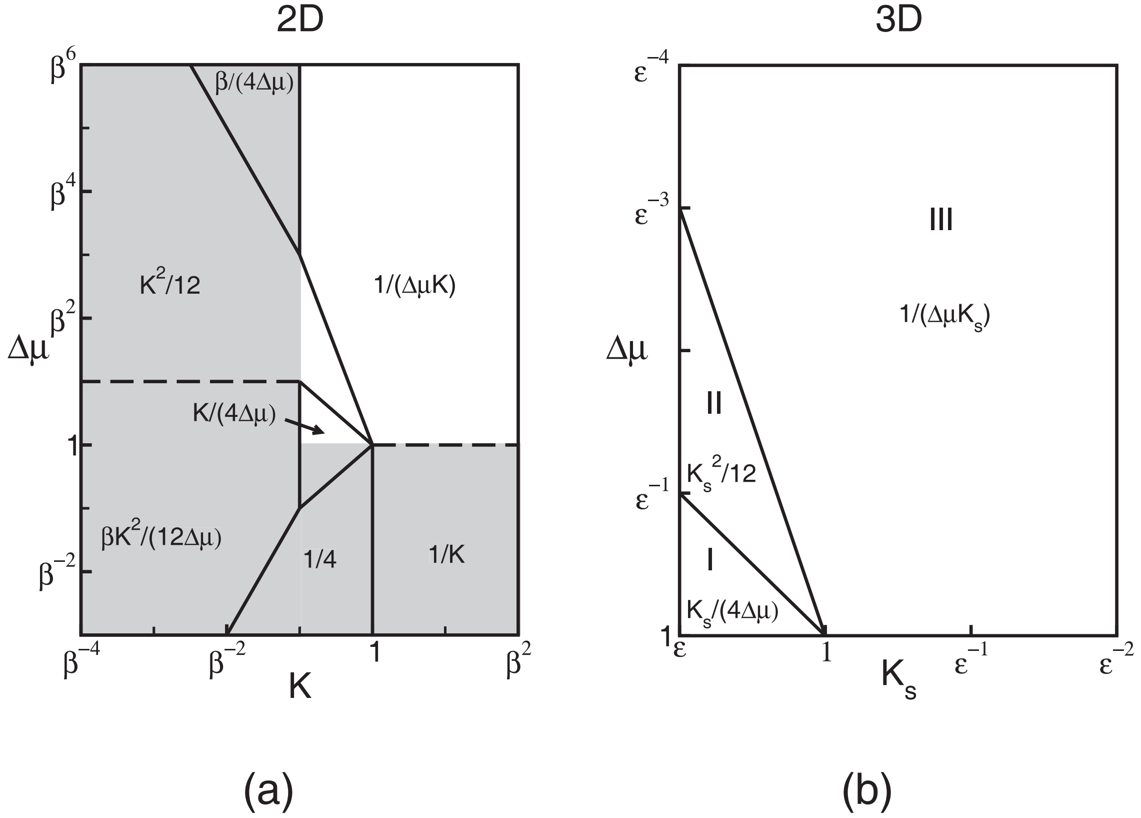

Figure 3.4: (a) The regime diagram for a 2-D Rayleigh-Taylor instability between two horizontal layers with different thicknesses, densities and viscosities (after *Canright and Morris*, 1993). The vertical axis is the viscosity contrast $\Delta\mu = \mu_0/\mu_1$ between the mantle and the TBL. The horizontal axis is the nondimensional wavenumber K of the perturbation. The boundaries between the regimes are shown with solid and dashed lines. The dashed boundaries indicate the change of rate-controlling viscosity (above the dashed line the instability growth rate is controlled by μ_0 and below the dashed line – by μ_1). The ratio of the thickness of the upper layer to the thickness of the lower layer is $\beta = (H - h)/h$. The instability growth rates in each regime are indicated. (b) The regime diagram for a Rayleigh-Taylor instability in a spherical shell geometry for $c = 0.5$. The vertical axis is the same as in 2-D. The horizontal axis is $K_s = 2\epsilon l$ where l is the spherical harmonic degree and $\epsilon = h/R_c$ is the ratio of the boundary layer thickness to the core radius. With these definitions, K_s is equivalent to K, β is equivalent to ϵ^{-1} and the top-right part of the 2-D regime diagram (the white region of the 2-D diagram, $\Delta\mu > 1$ and $K > \beta^{-1}$) is identical to the 3-D diagram.

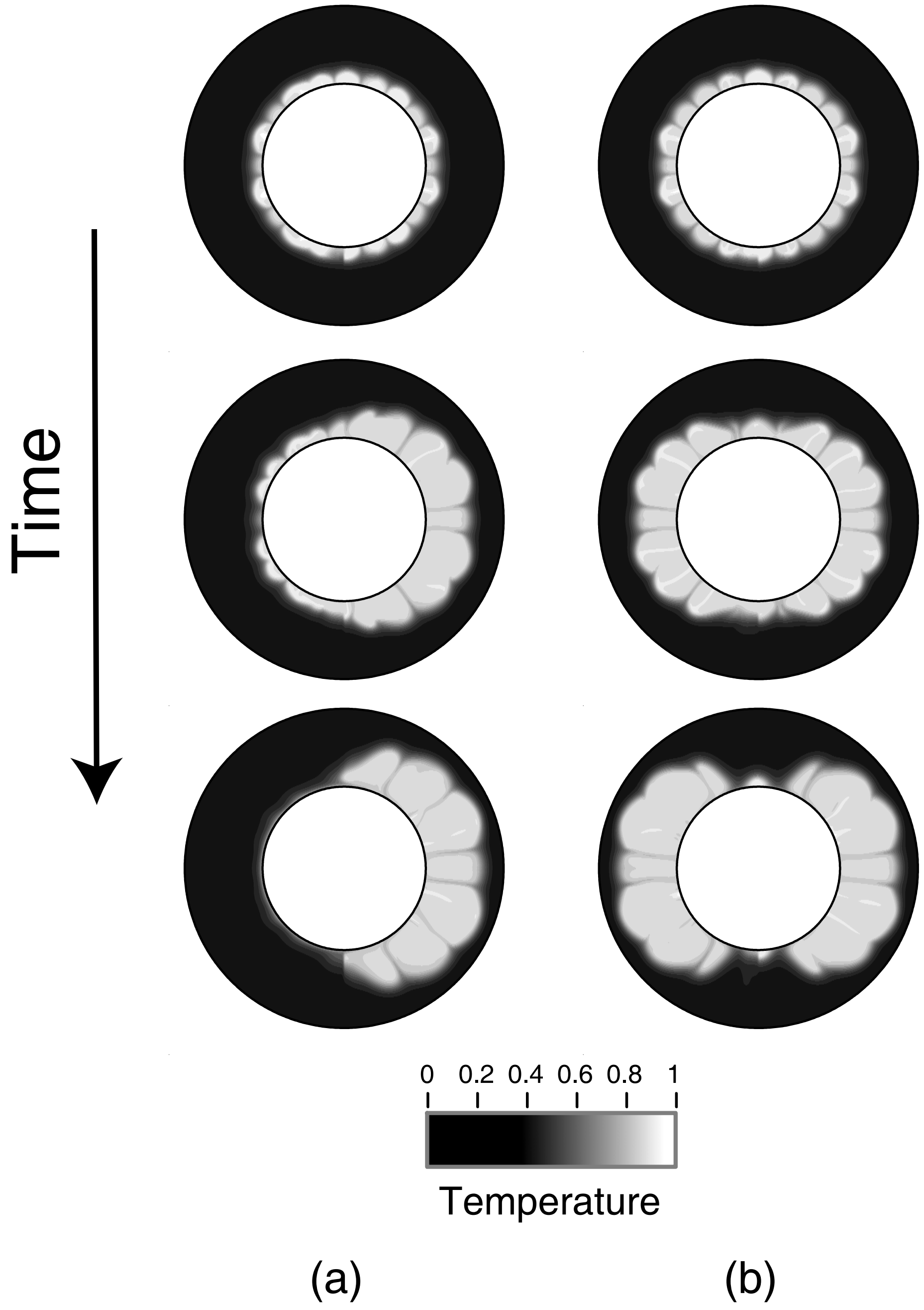

Figure 3.5: A sequence of snapshots (great circle cross-sections of the spherical shell temperature distribution) showing plume formation at large viscosity contrasts for (a) $l = 1$ ($t = 0.0031$, 0.0059 and 0.0067) and (b) $l = 2$ ($t = 0.0035$, 0.0057 and 0.0069). The initial mantle temperature is $T_m = 0$. The core-mantle boundary temperature $T_c = 1$ is constant during the evolution. The surface thermal boundary layer is not important for this study and is not simulated (the surface temperature is $T_s = 0$). The shades of gray highlight hot (light) and cold (dark) plumes of small-scale convection inside the TBL. The mantle temperature above the TBL is close to zero. The regions with $T < 0.6$ are shown with black.

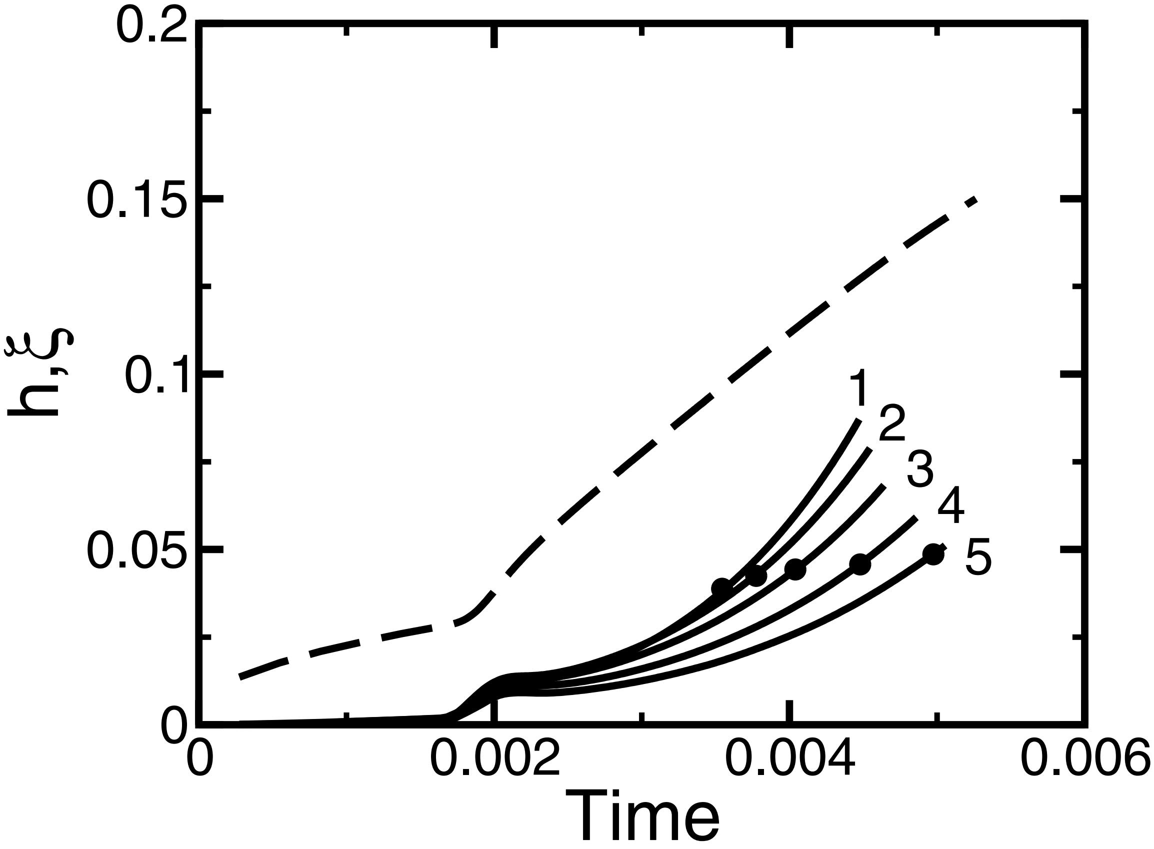

Figure 3.6: The thickness of the thermal boundary layer h (dashed line) and the amplitude of the large-scale instability ξ (solid line) for the spherical harmonic degree $l = 1, 2, 3, 4$ and 5 ($m = l$). The onset time of plume formation (indicated by solid circles) is determined from the condition $\dot{h} = \dot{\xi}$.

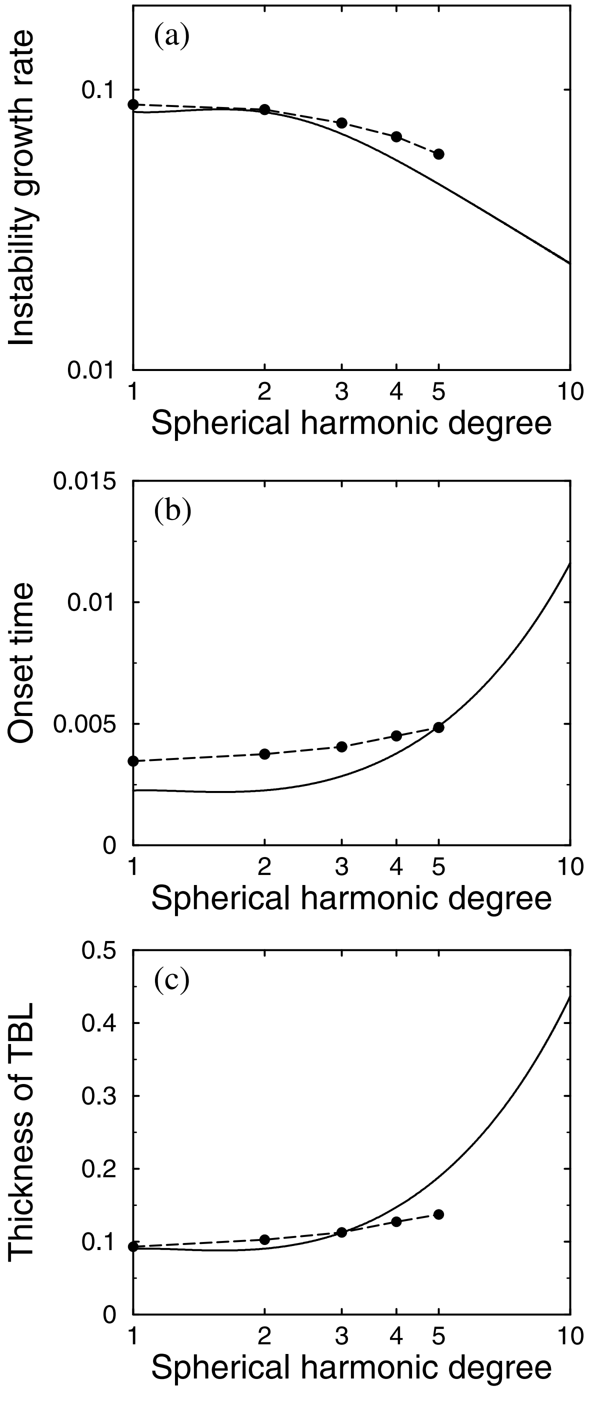

Figure 3.7: (a) Dependence of the growth rate, s, of large-scale instability, (b) the onset time, t_p, of plume formation and (c) the thickness, h_p, of the TBL at $t = t_p$ on the spherical harmonic degree l. The solid lines show the theoretical prediction. The dashed lines show the numerical results. Note that the theory does not use any adjustable parameters.

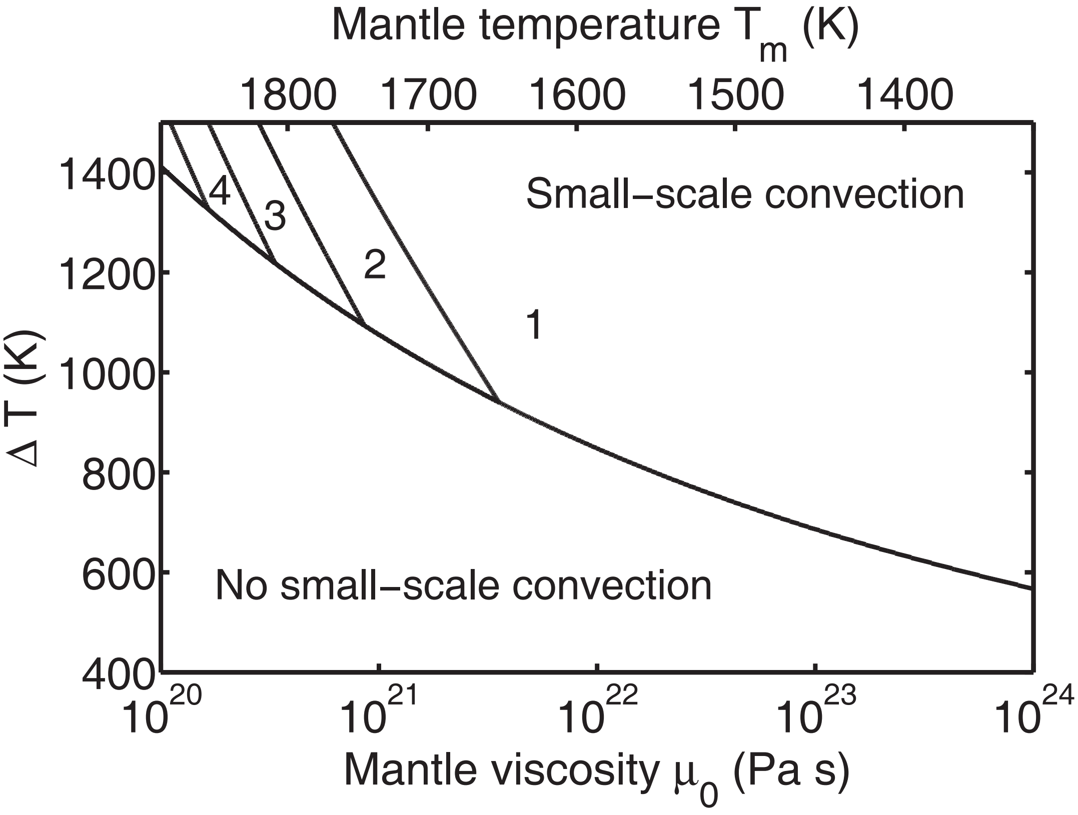

Figure 3.8: The boundary separating the two regimes of plume formation (with or without small-scale convection in the TBL) is shown as a function of mantle temperature and the temperature difference between the core and mantle. The numbers of plumes in the large viscosity contrast regime (with small-scale convection) are indicated. The viscosity law corresponds to diffusion creep in wet olivine.

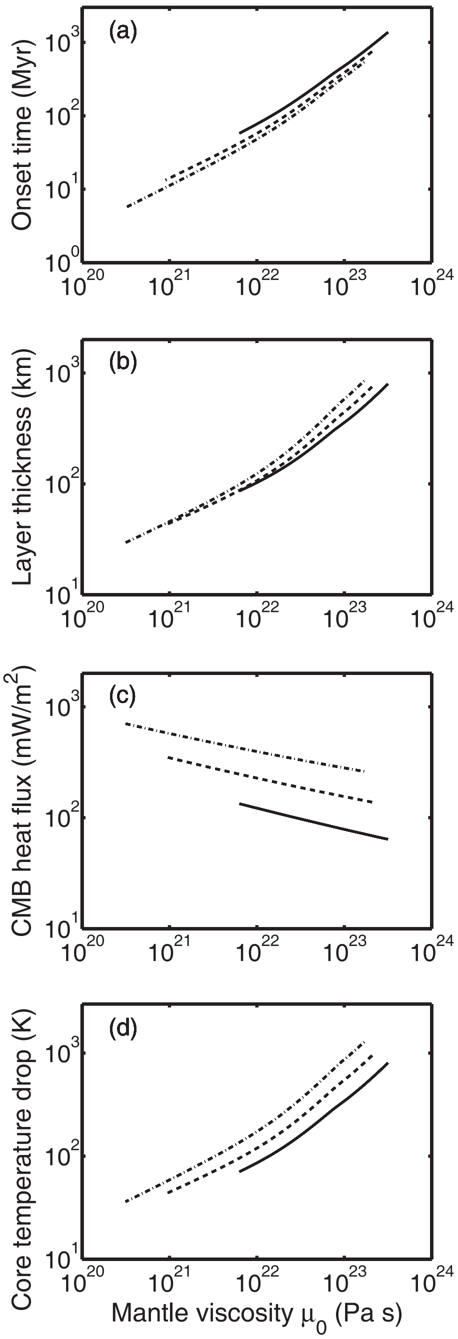

Figure 3.9: (a) The onset time of plume formation, (b) the thickness of the TBL, (c) the heat flux at the CMB and (d) the core temperature drop due to plume formation as functions of mantle viscosity. The variations in mantle viscosity are related to mantle temperature by Eq. (3.2). The temperature difference across the TBL is 900 K (solid line), 1100 K (dashed line) and 1300 K (dotted line). The curves start at the point where the spherical degree l of the most unstable is $l = 1$ (one plume) and end at the point where the convecting layer propagates through the entire mantle without generating plumes.

Chapter 4

Coupled core-mantle thermal evolution of early Mars

Y. Ke and V. S. Solomatov,

Journal of Geophysical Research, 114, E07004, doi:10.1029/2008JE003291.

Several arguments point out that at the end of planetary accretion, the core of Mars was likely to be much hotter than its mantle, resulting in the formation of a completely or partially molten thermal boundary layer at the base of the mantle. Here we address the following questions: How did the superheated core cool and what role did it play in the early mantle dynamics of Mars? We divide the coupled core-mantle evolution of early Mars into two stages. During the first stage, vigorous convection within the molten boundary layer removes the heat from the core so that the boundary layer expands up. As the boundary layer gets thicker, the temperature of the layer decreases. Eventually the temperature of the molten boundary layer drops down to the temperature for the rheological transition (melt fraction ∼40%) within 100 years. This stage is described by a parameterized convection approach. The second stage is modelled in spherical shell geometry using the fully three-dimensional finite element code CitcomS. A single plume ("superplume") forms by the instability of the thermal

boundary layer. The superplume stage lasts much longer, on the scale of millions to hundreds of millions of years, depending on the mantle viscosity. During both stages of evolution the heat flux can easily satisfy the requirements for the dynamo.

4.1 Introduction

Various arguments suggest that the mantles of the terrestrial planets were partially or completely molten during accretion (e.g. [*Elkins-Tanton et al.*, 2003, 2005a, b; *Solomatov*, 2007]). The energy associated with large impacts and core formation are among the most significant factors contributing to heating and melting of the mantle. The cores of the terrestrial planets may have been even hotter than their mantles [*Ke and Solomatov*, 2006]. This possibility is supported by several arguments. On the present-day Earth, the temperature contrast between the lower mantle and the core is estimated to be 1000 to 2000 K [*Boehler*, 1996, 2000; *Williams*, 1998] and was probably even higher in the past as the core temperature must have decreased more than the mantle temperature during planetary evolution [*Stevenson et al.*, 1983]. Another argument comes from numerical simulations of giant impacts, which show that during collisions of large differentiated bodies with the proto-Earth the material that was heated most was the iron core of the impactor [*Canup*, 2004]. After the iron from the impactor's core segregated into the Earth's core, the temperature contrast between the core and the mantle reached several thousand degrees Kelvin. For a smaller planet like Mars the core-mantle temperature difference after a giant impact may be high as well, of the order of $\sim$ 1000 K [*Ke and Solomatov*, 2006].

A different argument for a superheated core was suggested by *Stevenson* [2001]. He pointed out that a substantial fraction of the gravitational potential energy of core formation can, in principle, be retained within the segregated iron. Although there are many factors controlling the energy partitioning between the mantle and the core, how liquid iron moves through the dominantly solid mantle might be the most important one.

If liquid iron moves through the mantle in the form of blobs, the mantle has to deform to allow the motion of the blobs (Fig. 4.1a). Because the strain rates in the liquid iron, $\dot{e}_{\mathrm{Fe}}$, and the mantle, $\dot{e}_{\mathrm{m}}$, are of the same order of magnitude (this is valid when the blob viscosity is smaller than the viscosity of the surrounding fluid, see the solution for the flow around a sphere with finite viscosity [*Landau and Lifshitz*, 1987]), the ratio of viscous dissipation rates between the iron and the mantle is proportional to

$$\frac{\dot{\epsilon}_{\mathrm{Fe}}}{\dot{\epsilon}_{\mathrm{m}}} = \frac{\mu_{\mathrm{Fe}}\dot{e}^2_{\mathrm{Fe}}}{\mu_{\mathrm{m}}\dot{e}^2_{\mathrm{m}}} \propto \frac{\mu_{\mathrm{Fe}}}{\mu_{\mathrm{m}}}, \tag{4.1}$$

where μ_{m} is the mantle viscosity and μ_{Fe} is liquid iron viscosity. This means that most of the gravitational potential energy of core formation dissipates within the mantle (Fig. 4.1a).

Numerical simulations show that magma migration [*Wiggins and Spiegelman*, 1995; *Connolly and Podladchikov*, 2007] as well as segregation of liquid iron [*Golabek et al.*, 2008] results in the formation of melt channels. If liquid iron segregated in channels (Fig. 4.1b), then the viscous stresses in the liquid iron, τ_{Fe}, and in the mantle, τ_{m}, are of the same order of magnitude and thus, the ratio of viscous dissipation rate between the iron and the mantle is

$$\frac{\dot{\epsilon}_{\mathrm{Fe}}}{\dot{\epsilon}_{\mathrm{m}}} = \frac{\tau^2_{\mathrm{Fe}}/\mu_{\mathrm{Fe}}}{\tau^2_{\mathrm{m}}/\mu_{\mathrm{m}}} \propto \frac{\mu_{\mathrm{m}}}{\mu_{\mathrm{Fe}}}. \tag{4.2}$$

This implies that if iron segregated in channels the energy of core formation would largely go into the core ($\mu_{\mathrm{m}} \gg \mu_{\mathrm{Fe}}$).

Assuming that Mars was initially homogeneous, *Solomon* [1979] estimated that the gravitational potential energy released by core formation is $\Delta\Omega \sim 2 \cdot 10^{29}$ J. If all this energy is used to heat up the core, the average core temperature increases by

$$\Delta T_c = \frac{\Delta\Omega}{M_c c_{pc}} \approx 1800 \text{ K} \tag{4.3}$$

where $M_c \approx 1.4 \cdot 10^{23}$ kg is the mass of the core and $c_{pc} \approx 800$ J kg^{-1} K^{-1} is the specific heat of the core (Table 4.1).

If we consider the effect of a single giant impact, then assuming that the impact is about 0.1 of the mass of proto-Mars we obtain that segregation of iron from such an impact raises the core temperature by

$$\Delta T_c' \sim 0.1 \frac{gH}{c_{pc}} \approx 500 \text{ K}. \tag{4.4}$$

where $g = 3.7$ m s^{-2} is the gravity and $H \sim 1000$ km is the thickness of the Martian mantle (Table 4.1). The above estimates should be considered as an upper bound because some fraction of the heat, depending on the channel width and other factors, escapes from the hot channels to the mantle.

In addition to core superheating, an overturn of the Martian mantle would adiabatically cool the lower part of the mantle and increase the core-mantle temperature contrast even further. According to *Elkins-Tanton et al.*'s [2005a] calculations, the core-mantle temperature contrast due to mantle overturn is on the order of $\Delta T_m \sim 1000$ K.

The three effects described above, (i) the shock wave heating of impactor's iron core, (ii) the predominant partitioning of the core formation energy into the core, and (iii) lower mantle cooling due to mantle overturn, together may generate the temperature contrast between the core and the lower part of the Martian mantle from several hundred to several thousand degrees Kelvin.

This raises the following questions: How did the Martian core cool and what role did it play in the early evolution of the mantle? In our previous study we showed that a superheated core is likely to generate a single transient superplume which may be responsible for the formation of the Martian crustal dichotomy [*Ke and Solomatov*, 2006]. Here, we consider a coupled evolution of the core-mantle system and provide some constraints on how rapidly the core cools, what controls the cooling rate, how the decreasing temperature of the core affects the superplume evolution, and whether and for how long this type of dynamics can provide energy for the generation of the magnetic field on early Mars. We should note that while our discussion focuses on Mars, the results are general and can be applied to other planets as well.

4.2 Model

We consider a highly simplified structure of the mantle and the core immediately after the segregation of hot iron. The Martian mantle is assumed to be a spherical shell with uniform density ρ_m, temperature T_m, viscosity μ_m, and thickness $H = R_p - R_c$, where R_c is the core radius and R_p is the planet radius. Any variations in mantle properties are assumed to be negligible compared to the difference between the mantle and the hot thermal boundary layer (TBL) formed at the core-mantle boundary (CMB). If a partially molten shallow layer (a shallow magma ocean) existed at that time, it would mechanically decouple the lithosphere from the deep mantle. In this case the upper boundary of our model mantle corresponds roughly to the depth at which the melt fraction is $\sim 40\%$ (which is roughly the rheological transition between liquid-like and solid-like behavior, see below). The upper and the bottom boundaries of the mantle are stress-free.

The mantle temperature T_m during planetary accretion was probably not far from the mantle solidus. If the mantle was ever significantly molten, vigorous convection would cool the mantle very fast to near-solidus temperatures [*Williams and Nimmo*, 2004]. At the CMB pressure the solidus temperature is around 2450 K [*Zhang and Herzberg*, 1994]. This is an upper bound on the initial mantle temperature T_m. Depending on the mantle composition and the details of the mantle temperature profile, at this temperature the partially molten shallow layer may occupy a substantial portion of the mantle. A lower bound can be obtained by requiring the mantle to be completely solid which gives $T_m \approx 1600$ K. We also assume that radiogenic heating can be ignored due to differentiation of incompatible elements into the crust and/or due to short time scales considered in this study.

The Martian core is assumed to be vigorously convecting and have an adiabatic temperature profile with the CMB temperature higher than the mantle temperature by ΔT, that is $T_{\text{CMB}} = T_m + \Delta T$. For $T_m = 1600 - 2400$ K and $\Delta T = 1000$ K, $T_{\text{CMB}} = 2600 - 3400$ K. This suggests that T_{CMB} can easily exceed both the solidus (~ 2450 K) and the liquidus (~ 2650 K) [*Zhang and Herzberg*, 1994]). Although the uncertainties in these estimates are large, it seems very likely that the mantle was substantially molten and a completely or partially molten layer formed at the base of the mantle.

The processes in the partially molten layer formed near the core-mantle boundary can be quite complicated [*Labrosse et al.*, 2007] and similar to those occurring in magma oceans formed in the upper parts of planetary mantles [*Solomatov and Stevenson*, 1993a, b; *Solomatov*, 2000, 2007]. We assume that only negligible crystal-melt segregation occurs during cooling and crystallization of the molten region near the core-mantle boundary. The validity of this assumption depends on the crystallization time of the molten layer at the Martian core-mantle boundary and the crystal size. We will show the crystallization time is of the order of hundred years. This is sufficiently fast to ignore crystal-melt segregation in the terrestrial magma ocean provided the crystals are less than 1 mm in diameter [*Solomatov*, 2000, 2007]. Similar arguments apply to the Martian partially molten layer at the core-mantle boundary. Given huge uncertainties, both equilibrium crystallization scenario and fractional crystallization scenario of the molten layer seem equally possible. We will be assume the former as the simplest of the two. During plume formation, segregation of melt may become faster than the crystallization time. It would be interesting to consider the effect of melt segregation on plume formation in the future.

Qualitatively the system evolves as follows. Initially, most of the TBL is substantially molten and convection within the TBL is very vigorous. As the TBL thickness increases with time, both the TBL temperature and the core temperature decrease. At melt fraction $\phi = \phi_{cr} = 40\%$ (or crystal fraction 60%) the partially molten system undergoes a rheological transition from a low viscosity crystal suspension (that is the viscosity is controlled by liquid viscosity) to a partially molten solid (that is the viscosity is controlled by the deformation of the solid phase). The dynamic processes become much slower and are dominated by the large-scale instability of the TBL-mantle system.

Because no numerical code can handle the enormous viscosity contrast between the liquid and solid parts of the mantle, we first use a parameterized convection approach to describe the cooling of the TBL and the core before the melt fraction in the TBL drops below the rheological transition. Then we apply a fully three-dimensional finite element code CitcomS [*Zhong et al.*, 2000] to calculate the evolution beyond the rheological transition.

4.3 First stage of evolution: Parameterized convection calculations

4.3.1 Energy balance equation for the core

The energy balance equation for the core is

$$c_{pc} M_c \frac{d\bar{T}_c}{dt} = -A_c F_c \tag{4.5}$$

where $\bar{T}_c$ is the average temperature of the core, F_c is the heat flux at the CMB, $M_c = (4\pi/3)\rho_c R_c^3$ is the mass of the core, ρ_c is the core density, and A_c is the surface area of the core.

Assuming that the core is liquid and is vigorously convecting we can relate its average temperature $\bar{T}_c$ to the temperature T_{CMB} of the core-mantle boundary,

$$\bar{T}_c = \beta T_{\mathrm{CMB}} \tag{4.6}$$

where $\beta \approx 1.1$ [*Stevenson et. al.*, 1983]. We obtain:

$$\frac{dT_{\mathrm{CMB}}}{dt} = -\frac{3F_c}{\beta \rho_c c_{pc} R_c}. \tag{4.7}$$

The above formulae assume that the core is well mixed. Another assumption is that the temperature difference across the thermal boundary layer on the core side of the CMB is negligible. This boundary layer would substantially affect the estimates of the CMB heat flux and the TBL crystallization time only if the viscosity of liquid iron is much larger than the viscosity of liquid silicates, which seems unlikely [*Liebske et al.*, 2005; *Mound and Buffett*, 2007].

4.3.2 Energy balance equation for the TBL

To write the energy balance equation for the TBL we need to take into account the heat flux into the TBL, the heat flux out of the TBL, the temperature change of the TBL, the change in the thickness of the TBL and the latent heat of crystallization if there is any melt present. The heat flux into the TBL is equal to the heat flux F_c from the core. The heat flux out of the TBL (at the upper boundary) is close to zero because the temperature profile above the TBL quickly reaches a steady state profile in the frame of reference associated with the moving upper boundary of the TBL [*Solomatov and Moresi*, 2002]. The amount of heat stored in the TBL changes mainly because of the increase in the thickness of the TBL and the simultaneous decrease of its nearly isothermal convective interior. The latter is caused by the decrease in the core temperature and the fact that the temperature difference between the CMB temperature and the temperature of the nearly isothermal convective interior of the TBL is nearly constant and controlled by the rheological temperature difference [*Solomatov and Moresi*, 2002]. The energy balance for the partially molten TBL with the time-dependent thickness $h(t)$ and the melt fraction $\phi_{\mathrm{TBL}}(t)$ of the interior of the TBL is described by the following energy balance equation:

$$\frac{d}{dt}\left\{M_h\left[c_{pm}(T_{\mathrm{TBL}}-T_m)+\phi_{\mathrm{TBL}}L\right]\right\}=A_cF_c, \tag{4.8}$$

where c_{pm} is the specific heat of the mantle, $M_h=(4\pi/3)\rho_m[(R_c+h)^3-R_c^3]$ is the mass of the TBL, L is the latent heat, and T_{TBL} is the interior temperature of the TBL.

In linear approximation, the melt fraction is

$$\phi_{\mathrm{TBL}} = \frac{T_{\mathrm{TBL}} - T_s}{T_l - T_s}, \tag{4.9}$$

where T_l and T_s are mantle liquidus and solidus temperatures respectively.

4.3.3 Parameterized convection calculations

Equations (4.7) and (4.8) can be integrated to obtain h:

$$h = R_c \left\{ \left[\left(\frac{\rho_c}{\rho_m} \right) \frac{c_{pc}\beta \left(T^0_{\mathrm{CMB}} - T_{\mathrm{CMB}} \right)}{c_{pm}(T_{\mathrm{TBL}} - T_m) + \phi_{\mathrm{TBL}} L} + 1 \right]^{1/3} - 1 \right\}, \tag{4.10}$$

where T^0_{CMB} is the initial CMB temperature. The initial thickness of the TBL is assumed to be zero.

To find h as a function of time and estimate the crystallization time of the TBL we need to integrate Equations (4.7) and (4.8) with respect to time. However, because we already have Eq. (4.10) we only need to integrate Eq. (4.7). This integration requires the function F_c and the relationship between T_{TBL} and T_{CMB}.

For either turbulent or laminar convection and constant viscosity or strongly temperature-dependent viscosity convection, the heat flux F_c can be approximately parameterized as follows [*Kraichnan*, 1962; *Siggia*, 1994; *Schubert et al.*, 2001; *Solomatov*, 1995; *Solomatov and Moresi*, 2000]:

$$F_c \approx a_c k \Delta T_c^{4/3} \left(\frac{\alpha \rho_m g}{\kappa \mu_{\mathrm{TBL}}} \right)^{1/3}, \tag{4.11}$$

where k is the thermal conductivity, κ is the thermal diffusivity, α is the thermal expansivity, and μ_{TBL} is the viscosity of the convective interior of the TBL. The coefficient a_c and the driving temperature ΔT_c depend on the convective regime, heating mode and boundary conditions. The coefficient a_c varies very little and is usually close to ~ 0.1. We will use $a_c = 0.12$ in all our calculations.

The driving temperature difference ΔT_c varies substantially with temperature. When the temperature is very high (several thousand degrees Kelvin), and thus the interior of the TBL is completely molten, the viscosity variations are relatively small (at least in the temperature range from T_l to $T_{\mathrm{CMB}} > T_l$) and convection can be considered as constant viscosity convection with $\Delta T_c \approx T_{\mathrm{CMB}} - T_{cr}$, where T_{cr} is the critical temperature for the rheological transition.

At lower temperatures the viscosity depends strongly on temperature, and the driving temperature difference is proportional to the rheological temperature scale $\Delta T_{rh} = |d \ln \mu / dT|^{-1}$ [*Morris and Canright*, 1984; *Fowler*, 1985; *Davaille and Jaupart*, 1993a; *Solomatov*, 1995; *Moresi and Solomatov*, 1995; *Trompert and Hansen*, 1998]:

$$\Delta T_c \approx 3 \Delta T_{rh}. \tag{4.12}$$

For a partially molten system, the rheological temperature scale is defined as follows [*Davaille and Jaupart*, 1993b; *Reese and Solomatov*, 2006]:

$$\Delta T_{rh} = \left| \frac{d \ln \mu(T, \phi(T))}{dT} \right|^{-1}, \tag{4.13}$$

where $\mu(T, \phi(T))$ is an experimentally determined function of temperature T and melt fraction $\phi(T)$ and the partially molten system is assumed to be in thermodynamic equilibrium (otherwise ϕ would be history-dependent).

The viscosity of concentrated suspensions can be estimated using Roscoe's formula [*Roscoe*, 1952] (for alternative formulae see [*Solomatov and Stevenson*, 1993a]):

$$\mu_{pm, \phi > \phi_{cr}} = \mu_l \left(\frac{1 - \phi_{cr}}{\phi - \phi_{cr}} \right)^{2.5}, \tag{4.14}$$

where the viscosity of pure liquid is

$$\mu_l = \mu_{0,l} \exp\left(\frac{Q_l}{RT}\right) = \mu_{0,l} \exp\left(\frac{E_l + PV_l}{RT}\right), \tag{4.15}$$

where $\mu_{0,l}$ is a constant, Q_l, E_l, and V_l are the activation enthalpy, the activation energy, and the activation volume, respectively (e.g. [*Liebske et al.*, 2005]).

Using Eqs. (4.9), (4.13), (4.14), and (4.15) we obtain

$$\Delta T_{rh} = \left(\frac{Q_l}{RT_{\mathrm{TBL}}^2} + \frac{2.5}{T_{\mathrm{TBL}} - T_{cr}}\right)^{-1}. \tag{4.16}$$

At low melt fractions we can use the solid-state viscosity reduced due to the presence of melt:

$$\mu_{pm,\phi<\phi_{cr}} = \mu_s \exp\left(-\alpha_\mu \phi\right), \tag{4.17}$$

where $\alpha_\mu \sim 25$ for diffusion creep [*Scott and Kohlstedt*, 2004] and μ_s is the viscosity of solid silicates:

$$\mu_s = \mu_{0,s} \exp\left(\frac{Q_s}{RT_{\mathrm{TBL}}}\right) = \mu_{0,s} \exp\left(\frac{E_s + PV_s}{RT_{\mathrm{TBL}}}\right), \tag{4.18}$$

where $\mu_{0,s}$ is constant, Q_s, E_s, and V_s are the activation enthalpy, the activation energy, and the activation volume, respectively [*Karato and Wu*, 1993]. In this case, the rheological temperature scale is

$$\Delta T_{rh} = \left(\frac{Q_s}{RT_{\mathrm{TBL}}^2} + \frac{\alpha_\mu}{T_l - T_s}\right)^{-1}. \tag{4.19}$$

To smooth the transition between the two regimes, $\phi > \phi_{cr}$ and $\phi < \phi_{cr}$, we use the following equation:

$$\frac{1}{\mu_{pm}} = \frac{1}{\mu_{pm,\phi>\phi_{cr}}} + \frac{1}{\mu_{pm,\phi<\phi_{cr}}}. \tag{4.20}$$

Because a secondary thermal boundary layer forms at the bottom of the vigorously convecting TBL, the TBL temperature T_{TBL} is smaller than the CMB temperature T_{CMB}. At high temperatures, when the TBL can be treated as a nearly isoviscous layer, we assume that $T_{\text{CMB}} - T_{\text{TBL}} \approx 0.5\Delta T_c$. At lower temperatures we can use the stagnant lid convection scaling $T_{\text{CMB}} - T_{\text{TBL}} \approx \Delta T_{rh}$. To smooth the transitions between all the regimes we simply require that $T_{\text{CMB}} - T_{\text{TBL}}$ monotonically increases with T_{CMB}.

Figure 4.2 shows variations of the TBL parameters with the CMB temperature. As the CMB temperature decreases from liquidus ($T_l = 2650$ K) to solidus ($T_s = 2450$ K), the driving temperature difference for convection inside the TBL decreases, the viscosity increases and the heat flux decreases. The most drastic changes occur around $\phi \sim \phi_{cr}$ ($T_{cr} \approx 2530$ K).

Figure 4.3 shows the results of parameterized calculations of thermal evolution of the coupled core-mantle system for $T_m = 1600$, 2000 and 2400 K and $T_{\text{CMB}} = T_m + 1000$ K. Cooling and crystallization of the molten TBL to $\phi = \phi_{cr}$ is very fast (~ 100 years) and depends only weakly on the assumed parameters. This fast time scale is due to a low viscosity of the TBL which generates a very high convective heat flux as suggested by Eq. (4.11). After the melt fraction drops to $\sim 40\%$ (the end of the calculations in Fig. 4.3) the viscosity significantly increases and the CMB temperature continues to decrease at a much slower rate.

4.3.4 TBL thickness at the rheological transition

When the TBL undergoes the rheological transition the viscosity contrasts in the mantle drop substantially and can be handled by fully three-dimensional finite element calculations. The TBL thickness and the temperatures of the core and the mantle at this transition can be used as a guide to choose the initial conditions for the three-dimensional calculations.

To estimate $h = h_{cr}$ at the rheological transition, we require that $T_{\mathrm{TBL}} = T_{cr}$ and $\phi_{\mathrm{TBL}} = \phi_{cr}$. The CMB temperature T_{CMB} can be set to $T_{\mathrm{CMB}} \approx T_{cr}$ as well because the temperature difference between T_{CMB} and T_{TBL} becomes very small when T_{TBL} approaches T_{cr} (Fig. 4.2c). The value of h_{cr} at the rheological transition is shown as a function of T^0_{CMB} and T_m in Fig. 4.4.

4.4 Second stage of evolution: Fully three-dimensional calculations

4.4.1 Equations

To non-dimensionalize the equations, we choose $H = R_p - R_c$ as the length scale, $t_0 = H^2/\kappa$ as the time scale, $u_0 = H/t_0$ as the velocity scale, and $\Delta T = T_{\mathrm{CMB}}(0) - T_m$ as the temperature scale, where $\kappa = k/\left(\rho_m c_{pm}\right)$ is the coefficient of thermal diffusion and $T_{\mathrm{CMB}}(0) \approx T_{cr}$ is the initial temperature of the core-mantle boundary (in this section, "initial" refers to the initial conditions for the three-dimensional calculations). The ratio R_c/R_p is set to 0.5.

Numerical simulations are performed using CitcomS [*Zhong et al.*, 2000]. The model is very similar to that studied by *Ke and Solomatov* [2006] except that we modified the code to take into account the effect of core cooling (Eq. 4.7).

The non-dimensional equations of thermal convection in the Boussinesq approximation are

$$\nabla \cdot \mathbf{u} = 0, \tag{4.21}$$

$$0 = -\nabla p + \alpha \rho g T \mathbf{n} + \nabla \cdot [\mu(\nabla \mathbf{u} + \{\nabla \mathbf{u}\}^T)], \tag{4.22}$$

$$\frac{\partial T}{\partial t} + \mathbf{u} \cdot \nabla T = \nabla^2 T. \tag{4.23}$$

where $\mathbf{u}$ is the velocity vector, p and T are the pressure and temperature perturbations, $\mathbf{n}$ is a unit vector in the direction of gravity, and $\{\}^T$ is the transpose operator.

The Rayleigh number is defined as

$$Ra_m = \frac{\alpha \rho_m g \Delta T H^3}{\kappa \mu_m}, \tag{4.24}$$

where α is the thermal expansion coefficient, g is the acceleration due to gravity, and μ_m is the mantle viscosity.

The viscosity law used in the numerical calculations is as follows:

$$\mu = \mu_m \exp[-\gamma(T - T_m)] \tag{4.25}$$

where γ is a constant defining the contrast between the mantle viscosity μ_m and the viscosity μ_{CMB} at the core-mantle boundary

$$\frac{\mu_m}{\mu_{\mathrm{CMB}}} = \exp[\gamma(T_{\mathrm{CMB}} - T_m)]. \tag{4.26}$$

This viscosity law is clearly a simplification of the actual complex rheology of the TBL and the mantle as a whole. Our previous calculations [*Ke and Solomatov*, 2004, 2006] suggest that the details of the viscosity law may not be very important (like in many other cases involving strongly temperature-dependent viscosity [e.g., *Solomatov*, 1995]). In our problem, two properties of the viscosity law matter most. One is the viscosity function of the least viscous region that is the convective region inside the TBL (where the viscosity varies from μ_{CMB} to roughly $10\mu_{\mathrm{CMB}}$). It can be reasonably well approximated by an exponential function (the Frank-Kamenetskii approximation). The other property is the total viscosity contrast between the mantle and the TBL. This controls the instability of the TBL-mantle system.

The initial thermal state of the planet is an isothermal mantle (an isothermal mantle in Boussinesq approximation corresponds to an adiabatic mantle) with a basal boundary layer of thickness h and temperature T_{CMB}. This basal layer represents a partially solidified TBL (with $\phi \sim \phi_{cr}$) after the initial core cooling period.

4.4.2 Parameters

In all our calculations, $Ra_m = 1.25 \cdot 10^3$ and $\eta_m/\eta_{\mathrm{CMB}} = 10^6$. Our choice of the Rayleigh number and the viscosity contrast represents a practical limit that can be achieved at present with the total number of finite elements $64 \times 64 \times 64 \times 12$ (CitcomS divides the 3-D spherical shell into 12 caps; for each cap, the grid is 64x64x64). Note that although the Rayleigh number for the mantle as a whole appears small, the effective Rayleigh number for convection inside the TBL reaches $\sim 10^9$ because the TBL viscosity is much lower than the mantle viscosity. This implies an extremely vigorous convection and very thin thermal boundary layers inside the TBL itself.

For the values of the parameters that we choose in this study a single superplume is the preferred instability mode (i.e., it grows faster than multiple plumes). The number of plumes depends on several parameters. *Ke and Solomatov* [2006] showed that at least in the linear theory of Rayleigh-Taylor instability in spherical geometry a single superplume forms if the viscosity contrast $\mu_m/\mu_{\rm TBL}$ between the mantle and the TBL is larger than $(R_c/h)^3$ (for $R_c/R_p \sim 0.5$) at the time when the superplume development becomes faster than the growth of the TBL. Because of a very short crystallization time of the TBL ($\Delta t \sim 10^2$ years, Section 3.3), plumes do not form until the TBL reaches the rheological transition as long as the mantle viscosity is higher than $\sim \alpha\rho g \Delta T H \Delta t \sim 10^{18}$ Pa s (see Equations (33) and (34) from [*Ke and Solomatov*, 2006]). Thus, a relatively modest viscosity contrast between the TBL (at the rheological transition) and the mantle is required to generate one superplume. For example, for $h \sim 100$ km, $\mu_m/\mu_{\rm TBL}$ has to be larger than $\sim (R_c/h)^3 \sim 5 \times 10^3$. This number is certainly smaller than the viscosity contrast between the near-solidus mantle and the mantle at the rheological transition. Thus, although it is possible to choose viscosity parameters that allow the formation of several plumes, we assume that the viscosity contrast between the TBL and the mantle is sufficiently large so that only a single superplume forms.

Based on the results of parameterized convection calculations we consider a broad range of the initial non-dimensional boundary layer thickness: $h(0) \sim 0$, 0.25, and 0.5.

4.4.3 Results

The results of three-dimensional calculations are shown in Figs. 4.5, 4.6, and 4.7. The coupled core-mantle thermal evolution can be divided into three stages: (i) the growth of the internally convecting thermal boundary layer, (ii) the development of large-scale instability (the superplume formation), and (iii) the spread and decay of the superplume. Depending on the magnitude of mantle viscosity, the dimensional time scale for these stages can be quite broad ranging from millions to hundreds of millions of years [*Ke and Solomatov*, 2006].

The process of superplume formation is discussed in detail by *Ke and Solomatov* [2004, 2006]. Superplumes form as a result of Rayleigh-Taylor-type instability due to the density contrast between the thermal boundary layer and the overlaying mantle. This happens at the time when the instability becomes faster than the expansion of the thermal boundary layer.

Note that during the previous stage of evolution, when the thermal boundary layer at the base of the mantle was significantly molten the expansion of the thermal boundary layer was much faster than the development of the large-scale instability. After the rheological transition, the expansion of the TBL slows down by many orders of magnitude because the behavior of the boundary layer changes from liquid-like to solid-like. It is also worth noting for the initial values $h(0) = 0.25$ and 0.5 (Figs. 4.6 and 4.7) the large-scale instability of the whole boundary layer is faster than the propagation of the boundary layer already at the beginning of simulations.

Figure 4.8 shows the CMB temperature and the CMB heat flux (Eq. 4.11) as functions of time for the three cases presented in Figs. 4.5, 4.6, and 4.7. For comparison, we modeled this stage of evolution using parameterized convection approach based on Eq. (4.11). The parameterized convection calculations agree reasonably well with the three-dimensional finite element calculations despite the fact that the boundary layer is being swept away by the superplume. We interpret this agreement as an indication that the heat flux at the core-mantle boundary continues to be largely controlled by the rheological temperature scale ΔT_{rh}. Fluid dynamics of this regime is an important problem which would be interesting to address analytically. A mismatch in the beginning of evolution is due to a transient stage associated with the onset of convection. In the case of a negligibly small initial boundary layer thickness (Fig. 4.8a), the parameterized convection calculations take into account the initial conductive cooling. In this case, convection starts after the critical conditions for the onset of convection are satisfied [*Solomatov and Moresi*, 2002; *Ke and Solomatov*, 2004, 2006]. For the two other cases (Figs. 4.8b and 4.8c), the initial thickness of the boundary layer ($h(0) = 0.25$ and 0.5 correspondingly) is sufficiently large so that convection starts at the beginning of evolution.

Table 4.1: Physical parameters

Parameter	Value	Reference
Gravity, g	3.7 m s^{-2}	1
Planetary radius, R_p	3390 km	1
Mantle density, ρ	4000 kg m^{-3}	1
Core radius, R_c	1700 km	2
Core mass, M_c	$1.4 \cdot 10^{23}$ kg	3
Pressure at CMB, P_{CMB}	23 GPa	3
Mantle specific heat, C_{pm}	1200 J kg^{-1} K^{-1}	1
Core specific heat, C_{pc}	800 J kg^{-1} K^{-1}	4
Latent heat, L	$5 \cdot 10^5$ J kg^{-1}	4
Thermal expansion, α	$2 \cdot 10^{-5}$ K^{-1}	5
Thermal conductivity, k	4 W m^{-1} K^{-1}	6
Reference viscosity (solid), $\mu_{0,s}$	$4.27 \cdot 10^{10}$ Pa s	7
Activation energy (solid), E_s	240 kJ mol^{-1}	7
Activation volume (solid) V_s	$5 \cdot 10^{-6}$ m^3 mol^{-1}	7
Reference viscosity (liquid), $\mu_{0,l}$	10^{-5} Pa s	8
Activation energy (liquid), E_l	195 kJ mol^{-1}	8
Activation volume (liquid), V_l	$-3.65 \cdot 10^{-6}$ m^3 mol^{-1}	8

(1)*Zharkov* [1986], (2)*Yoder et al.* [2003], (3)*Longhi et al.* [1992], (4)*Anderson* [1995], (5)*Chopelas* [1996], (6)*Hofmeister* [1999], (7)*Karato and Wu* [1993], (8)*Liebske et al.* [2005].

4.5 Implications for the early Martian magnetism

Present-day Mars has no global intrinsic magnetic field. However, strong crustal remnant magnetism discovered by Mars Global Surveyor suggests that Mars once possessed a dynamo early in its history (∼4 Gyr ago) [*Acũna, et al.*, 1999; *Connerney, et al.*, 1999]. The cessation time of dynamo is inferred from the absence of magnetic field at several large impact basins, which suggests that Mars did not have its magnetic field when these impacts happened [*Acũna, et al.*, 1999]. Recent studies of giant buried basins [*Lillis, et al.*, 2006, 2007a, 2007b] further constrain the cessation time of the dynamo to be 4.15-4.40 Gyr ago if the cessation only happened once in the planetary history.

Several models have been proposed that explain operation of dynamo in the early history of Mars [*Nimmo and Stevenson, 2000*; *Breuer and Spohn*, 2003; *Williams and Nimmo*, 2004]. Our model can generate a dynamo as well. During the first 10^2 years, when the bottom boundary layer is molten, the heat flux (Fig. 4.2d) is many orders of magnitude higher than the critical heat flux $F_c \sim 5 - 20$ mW m^{-2} required for the dynamo [*Stevenson et al.*, 1983; *Nimmo and Stevenson*, 2000; *Williams and Nimmo*, 2004]. After the boundary layer crystallizes below the rheological transition, the heat flux drops significantly, yet it is sufficiently high to generate the dynamo for several hundred million years depending on model parameters (Figure 4.9). Note that small-scale convection in the boundary layer stops after 100-150 Myr and the subsequent evolution continues in the conductive regime. The long-term evolution (beyond 100-1000 Myr) can be affected by factors that are not considered in our model. In particular, if significant amounts of radiogenic isotopes are left in the mantle, the radiogenic heating would reduce the temperature contrast between the core and the mantle and decrease the duration time of the dynamo [*Nimmo and*

Stevenson, 2000].

4.6 Conclusion

We suggest a model of a coupled core-mantle evolution of early Mars assuming that the core was much hotter than the mantle. The evolution is divided into two stages. During the first stage, the thermal boundary layer at the base of the mantle is molten and convection within the boundary layer is controlled by liquid-state viscosity. This stage is calculated using a parameterized convection approach. The time scale for the crystallization of the boundary layer from a completely molten state to melt fraction ∼40% is of the order of hundred years. During this time, the mantle above the boundary layer is effectively stagnant. The boundary layer quickly expands upward, while its temperature and the temperature of the core decrease. The second stage of evolution, during which the bottom boundary layer crystallizes completely, is modelled using the three-dimensional finite element code CitcomS. Because the expansion of the thermal boundary layer becomes very slow, a large-scale instability of the boundary layer develops that eventually produces a superplume. This superplume continues to cool the core and generates sufficiently high heat flux that allows operation of the dynamo for at least several hundred million years.

4.7 Acknowledgments

The authors would like to thank two anonymous reviewers and the Associate Editor for their thoughtful and constructive comments that helped to improve the manuscript. This work was supported by NASA grants NNX06AB05G and NNX07AQ74G.

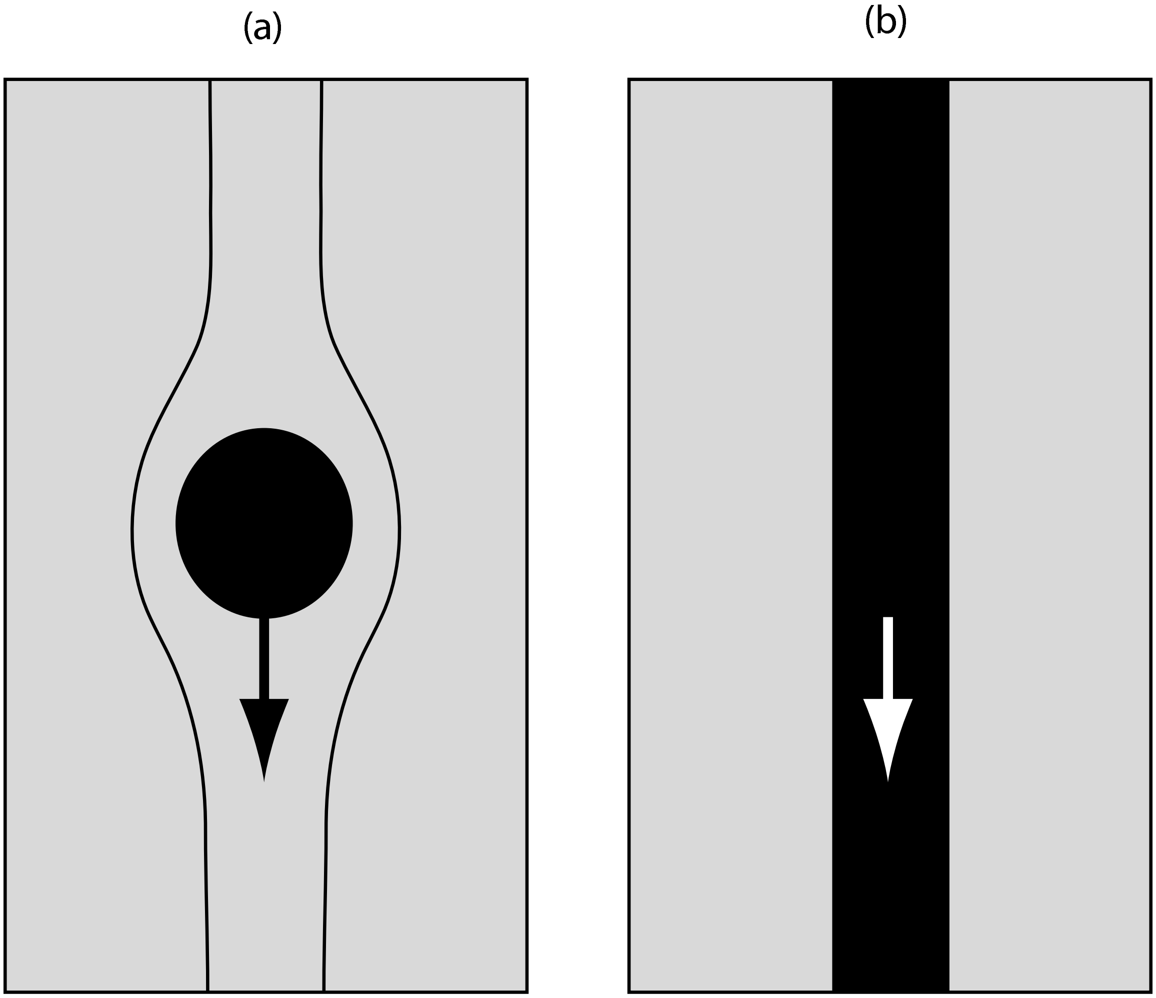

Figure 4.1: Two end-member cases of iron segregation in the Martian mantle: (a) low viscosity liquid iron blobs sink through a viscous mantle (the streamlines of the mantle flow around the blob are shown schematically) and (b) liquid iron flows down in cracks or channels. In case (a), viscous dissipation is largest in the mantle. In case (b), viscous dissipation is largest in the channel.

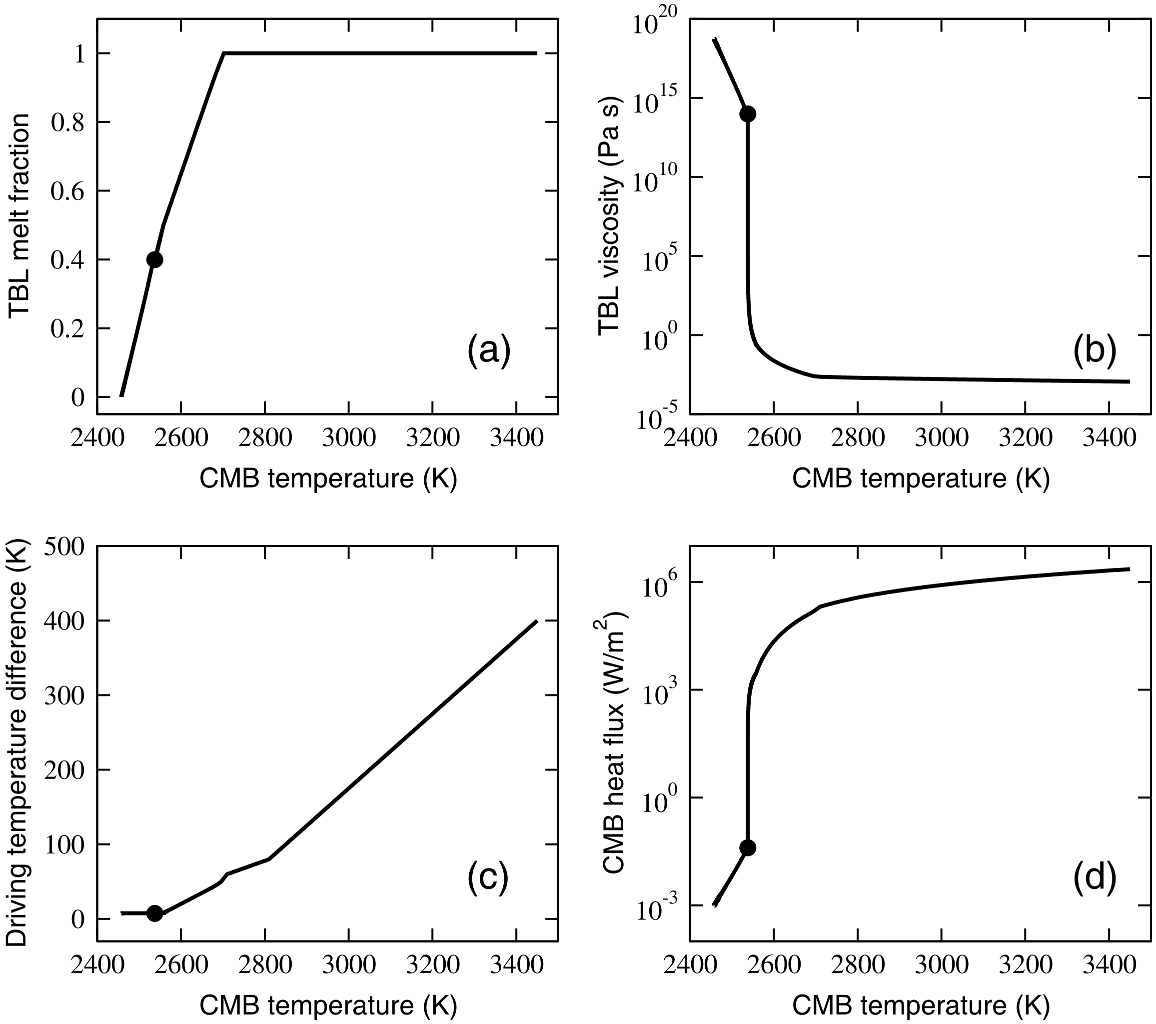

Figure 4.2: (a) Melt fraction in the TBL (at $T = T_{\mathrm{TBL}}$), (b) the viscosity of the TBL, (c) the temperature difference between the CMB and the TBL, and (d) the heat flux at the CMB as functions of the CMB temperature. As the temperature increases the deformation mechanism changes from a purely solid state creep to solid state creep softened by the presence of small amounts of melt (at $\phi < \phi_{cr}$) to viscosity of partial melts at high melt fractions ($\phi > \phi_{cr}$) and finally to purely liquid viscosity. The rheological transition at $\phi = \phi_{cr} = 40\%$ is shown with a black circle.

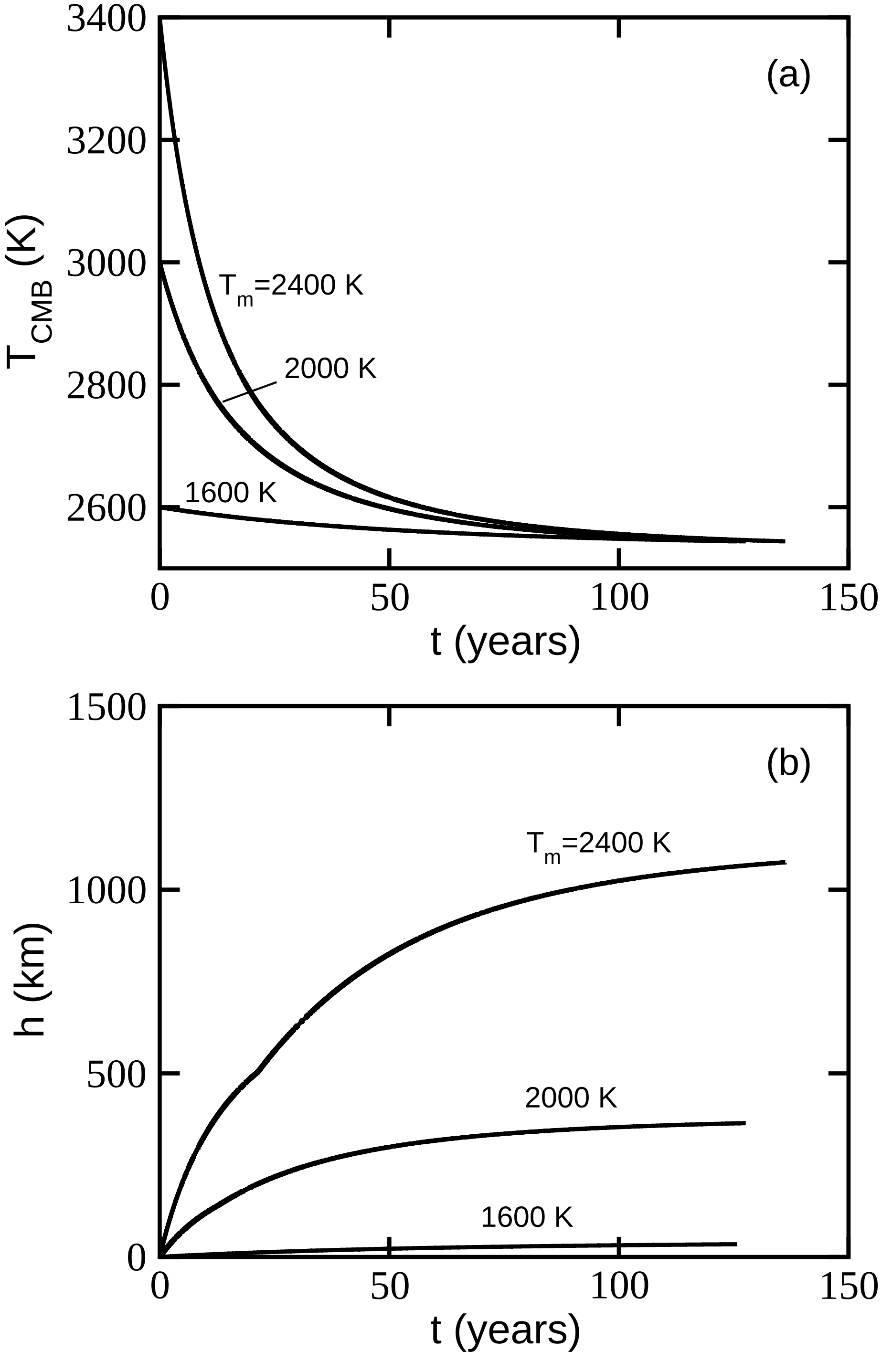

Figure 4.3: (a) Variation of the CMB temperature and (b) the thickness of the boundary layer during the first evolution stage when the behavior of the system is largely controlled by the viscosity of pure melt. The calculations end when the melt fraction drops to $\phi_{cr} = 40\%$. The labels show the mantle temperature. In all cases, the initial temperature of the CMB is higher than the mantle temperature by 1000 K.

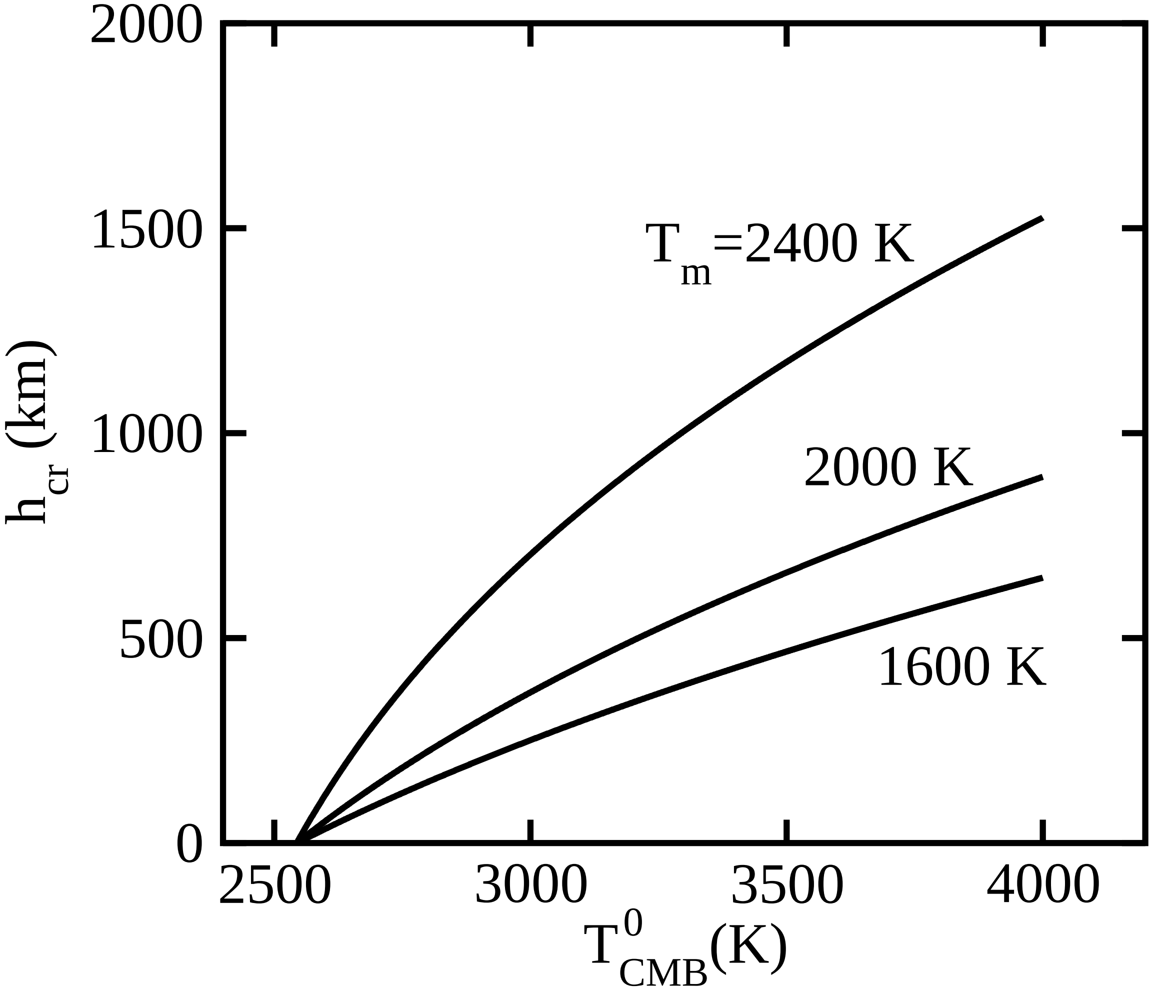

Figure 4.4: The thickness h_{cr} of the TBL by the time when the melt fraction in the TBL drops to $\phi_{cr} = 40\%$ as a function of the initial CMB temperature T^0_{CMB}. The temperature difference between the CMB and the TBL is assumed to be negligible at $\phi \sim \phi_{cr}$.

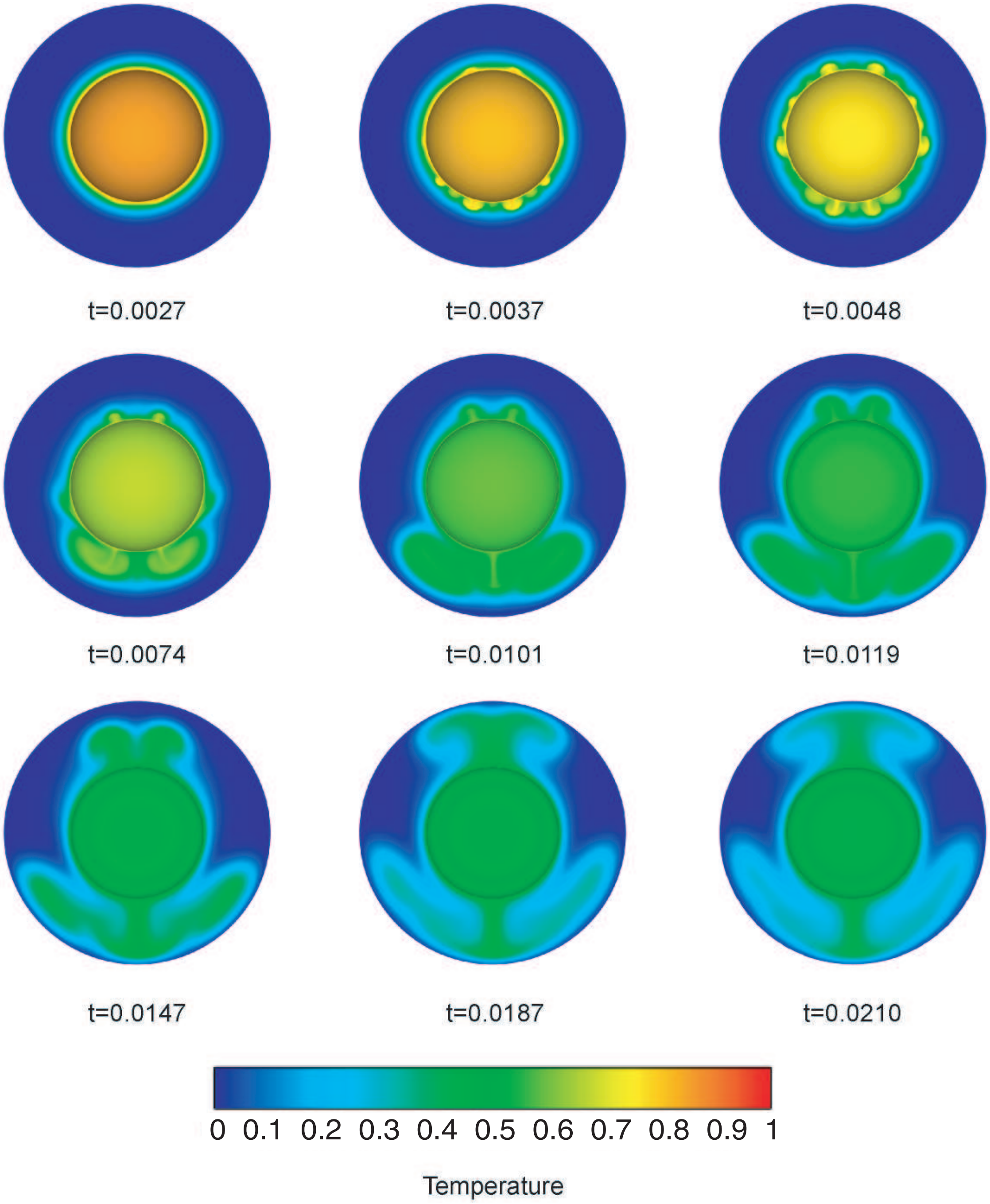

t=0.0027 t=0.0037 t=0.0048

t=0.0074 t=0.0101 t=0.0119

t=0.0147 t=0.0187 t=0.0210

Figure 4.5: A sequence of snapshots (cross-sections of the spherical shell temperature distribution) from fully three-dimensional simulations of superplume formation with core cooling. The central sphere shows the CMB surface. The initial boundary layer thickness is negligibly small, $h(0) \sim 0$. The non-dimensional initial CMB temperature is $T_{\text{CMB}} = 1$. It gradually decreases during superplume formation.

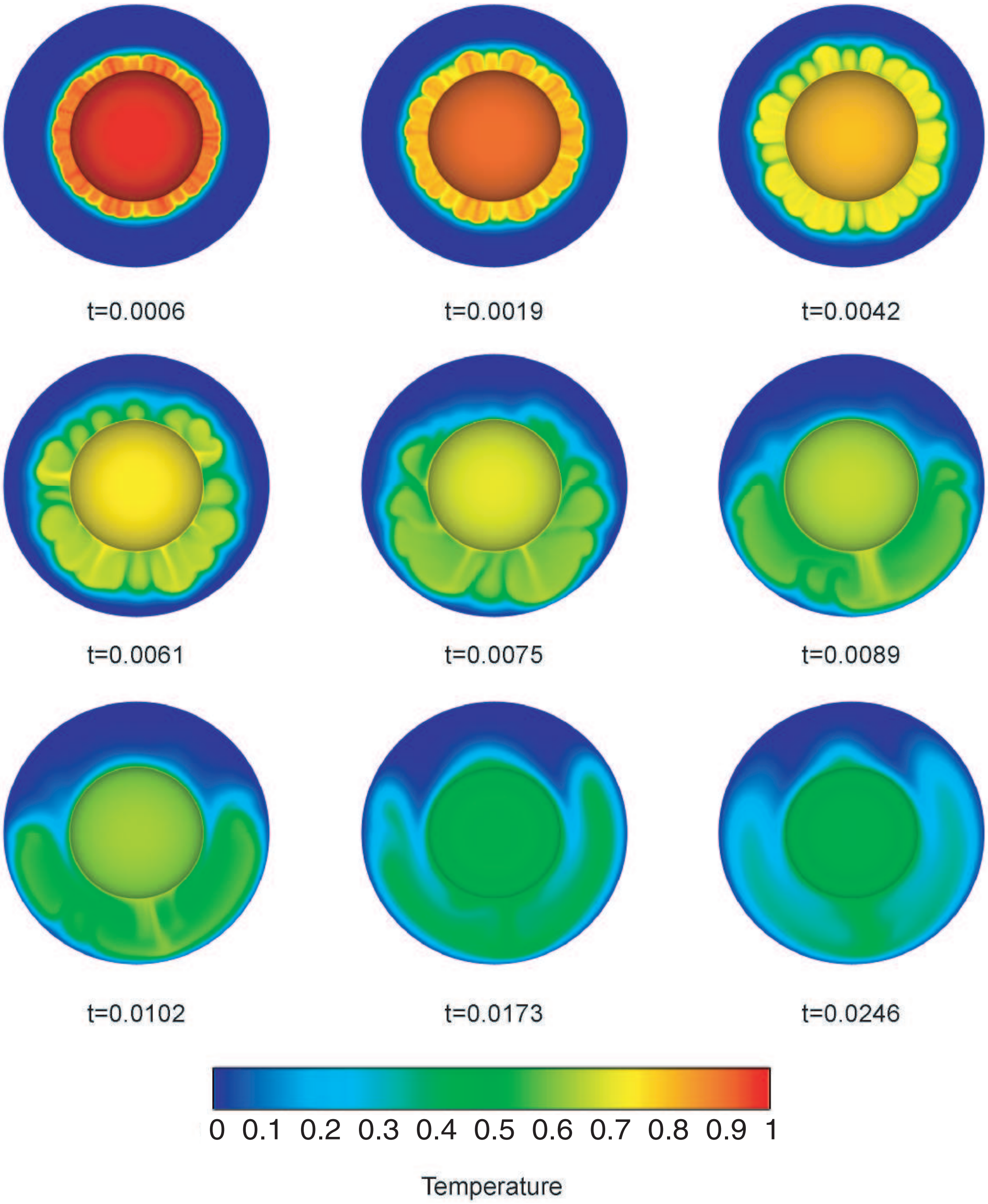

Figure 4.6: Same as Fig. 4.5 but the initial boundary layer thickness is $h(0) = 0.25$.

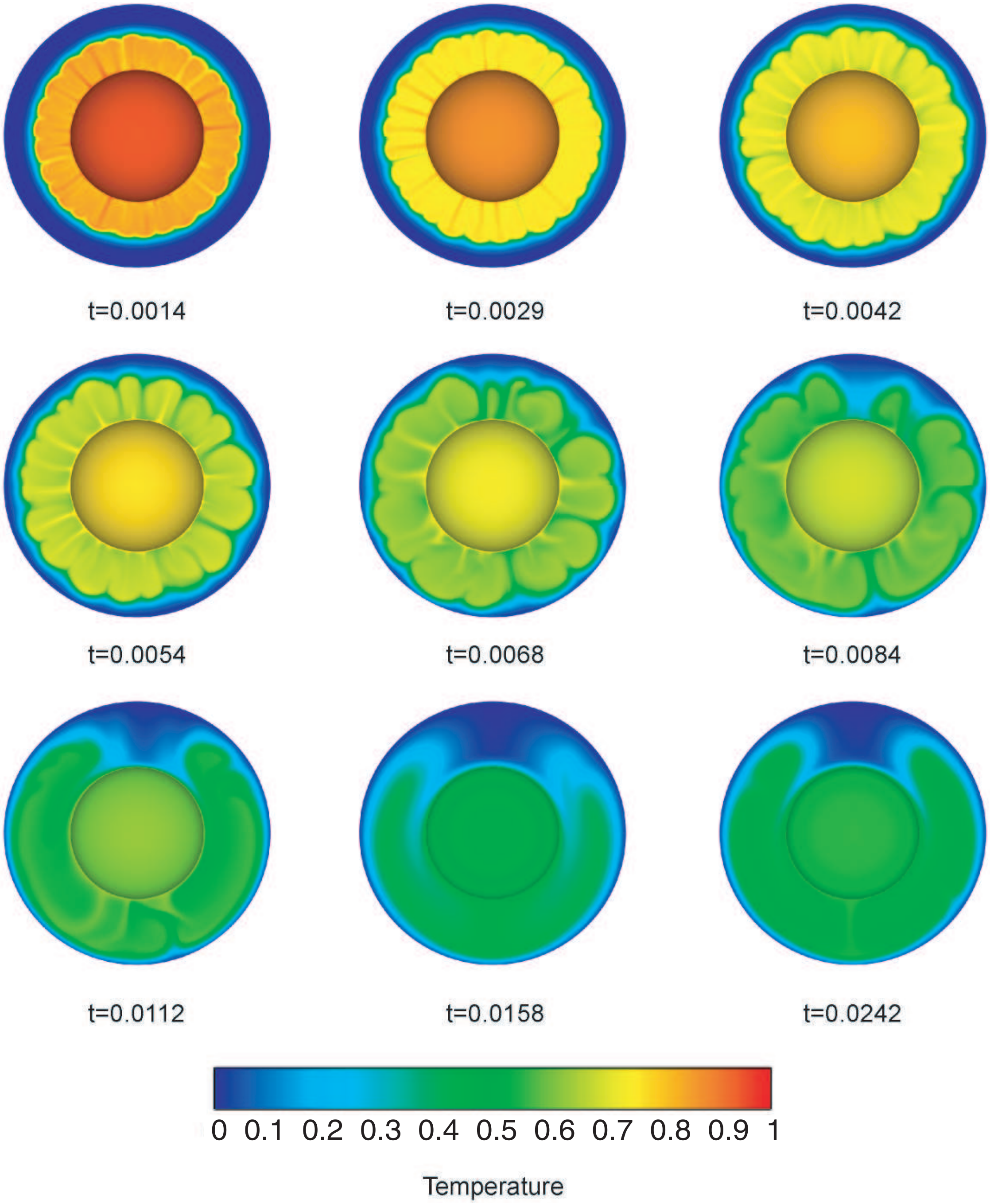

Figure 4.7: Same as Fig. 4.5 but the initial boundary layer thickness is $h(0) = 0.5$.

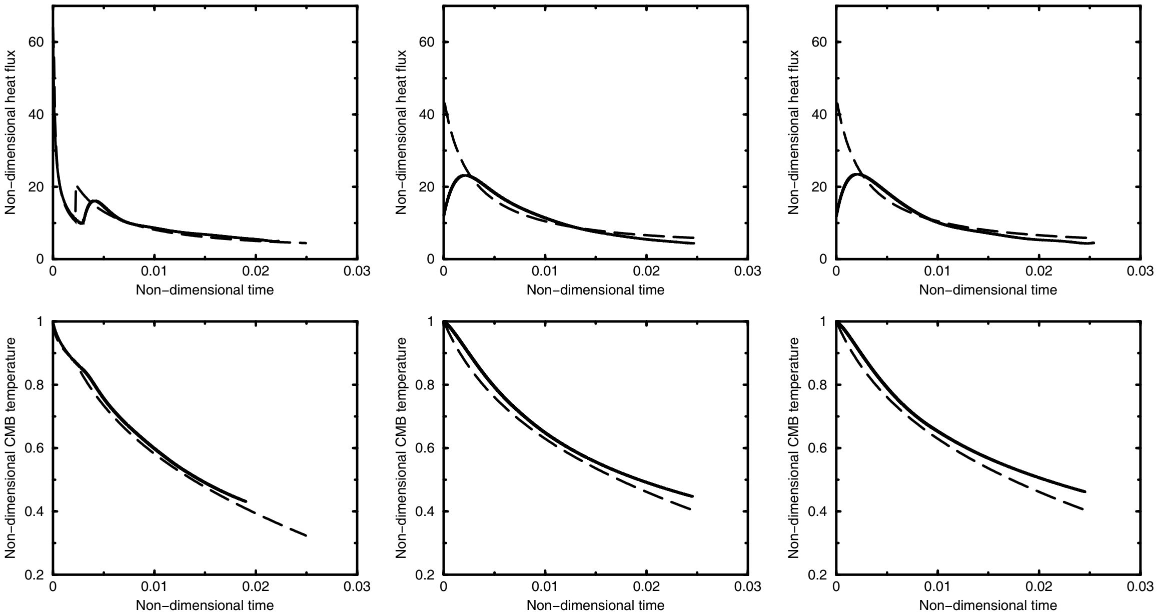

(a) (b) (c)

Figure 4.8: The CMB heat flux and CMB temperature as functions of time for the three cases shown in Figs 5, 6 and 7 (all parameters are non-dimensional): (a) $h(0) \approx 0$, (b) 0.25, and (c) 0.5. The solid lines correspond to the 3-D numerical simulations. The dashed lines are parameterized convection calculations based on the stagnant lid convection scaling laws. An abrupt increase in the heat flux in case (a) is due to the onset of convection. In cases (b) and (c) convection starts at $t = 0$. The difference between the 3-D simulations and parameterized convection calculations is due to a transient behavior which is not captured by the parameterized convection model.

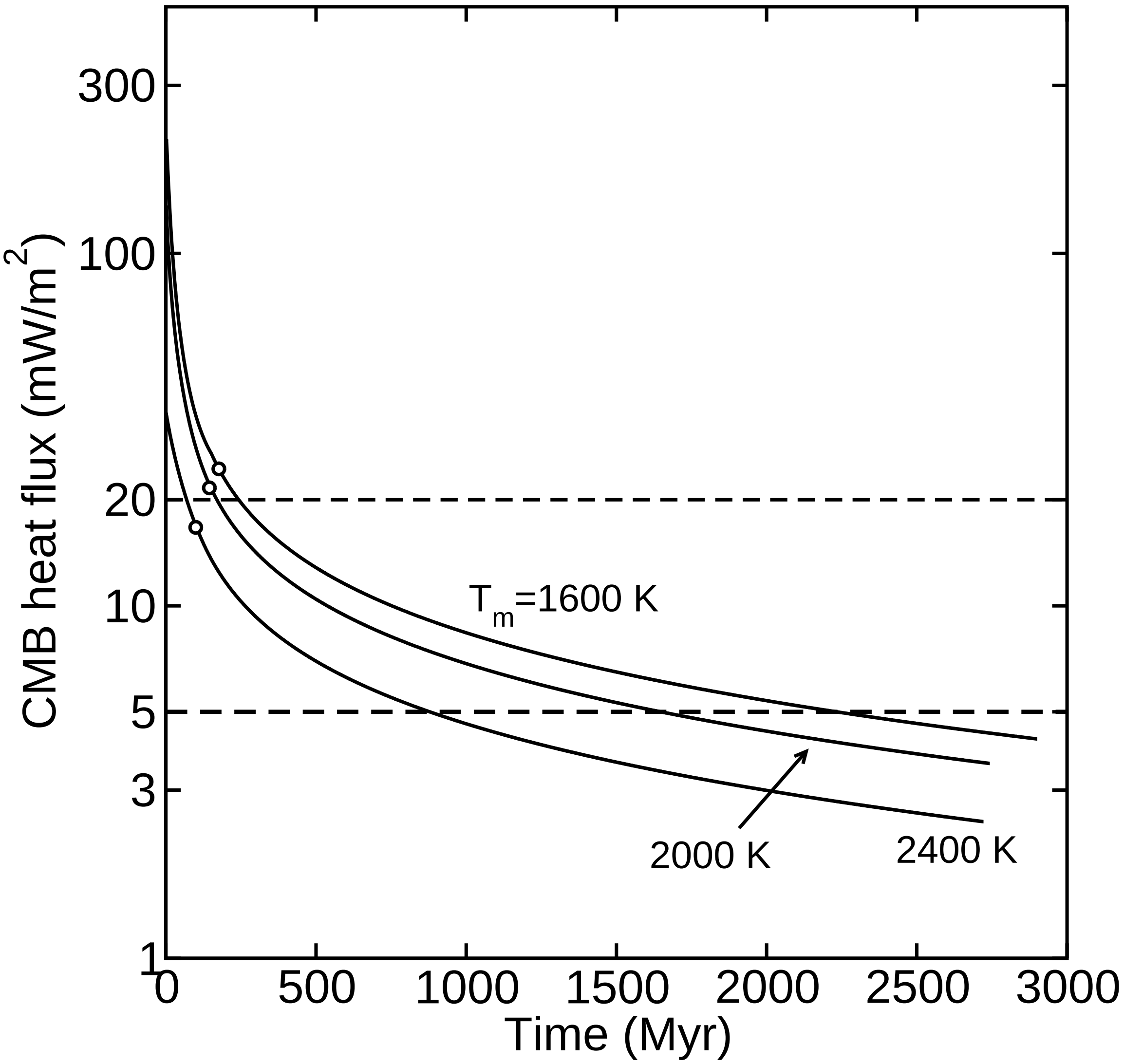

Figure 4.9: The CMB heat flux as a function of time during the superplume formation. Depending on the initial mantle temperature, small-scale convection in the partial melting boundary layer ceases around 100-150 million years (indicated by solid black circles) and after this the heat is transported across the boundary layer by conduction. The dashed lines show the range of the critical heat flux values for the cessation of the dynamo.

Chapter 5

Conclusions and future work

In the regime of very large viscosity contrasts, plumes form after an extended period of small-scale convection in the thermal boundary layer. A simple analysis based on the stagnant lid convection theory [*Solomatov and Moresi*, 2002] and the Rayleigh-Taylor instability theory [*Canright and Morris*, 1993] suggests that plume formation can approximately be described as a Rayleigh-Taylor instability of the two-layer system consisting of the vigorously convecting thermal boundary layer and a nearly isothermal layer above it. Plumes form when the growth rate of the large-scale instability of this two-layer system exceeds the growth rate of the convective thermal boundary layer. We developed a 2-D model of plume formation and suggested simple scaling laws that describe this process.

We then extended the 2-D model to 3-D spherical shell geometry and supported our scaling laws with the help of numerical simulations. The number of plumes and the rate of their development can vary substantially depending on the values of physical parameters and the temperatures of the core and the mantle when the model is applied to the terrestrial planets. Application of these scaling relationships to Mars shows that if at the end of planetary accretion, the Martian core was ~ 1000 K hotter than the mantle, one large plume ("superplume") may form. Its development can be very fast, on the order of 10 to 1000 Myr depending on the value of mantle viscosity. We propose that this transient superplume may play a role in the formation of crustal dichotomy and generation of magnetic field early in the history of the planet.

We developed a model of a coupled core-mantle evolution of early Mars assuming that the core was much hotter than the mantle. The evolution is divided into two stages. During the first stage, the thermal boundary layer at the base of the mantle is molten and convection within the boundary layer is controlled by liquid-state viscosity. This stage is calculated using a parameterized convection approach. The time scale for the crystallization of the boundary layer from a completely molten state to melt fraction ∼40% is of the order of hundred years. During this time, the mantle above the boundary layer is effectively stagnant. The boundary layer quickly expands upward, while its temperature and the temperature of the core decrease. The second stage of evolution, during which the bottom boundary layer crystallizes completely, is modelled using the three-dimensional finite element code CitcomS. Because the expansion of the thermal boundary layer becomes very slow, a large-scale instability of the boundary layer develops that eventually produces a superplume. This superplume continues to cool the core and generates sufficiently high heat flux that allows operation of the dynamo for at least several hundred million years. The application of our plume formation model can be extended to other planets. On the Earth, the model may explain the generation of superplumes in the past history.

In the future it would be important to include pressure-dependent viscosity, dislocation creep and grain size variations, investigate the role of melting on plume formation, and consider compositional differentiation. These studies would help understand better the differences among the planets. In particular, they may shed light on the origin of two large-scale seismic velocity anomalies in the deep mantle of the

Earth, under South Pacific and Africa (could these anomalies be superplumes suppressed by compositional density?), and on the mechanisms of global resurfacing of Venus (could the resurfacing be caused by the propagation of the TBL all the way up to the surface?). It would also be interesting to verify the superplume theory with laboratory experiments, at least in the Cartesian geometry.

Bibliography

Bibliography

[1] Acũna, M. H., et al. (1999), Global distribution of crustal magnetization discovered by the Mars Global Surveyor MAG/ER experiment, *Science, 284*, 790-793.

[2] Anderson, O. L. (1995), Mineral physics of iron and of the core, *Rev. Geophys. Suppl., 33*, 429-441.

[3] Andrews-Hanna, J. C., M. T. Zuber, and W. B. Banerdt (2008), The Borealis basin and the origin of the martian crustal dichotomy, *Nature, 453*, 1212-1215.

[4] Bertka, C. M, and Y. Fei (1997), Mineralogy of the Martian interior up to core-mantle boundary pressures, *J. Geophys. Res., 102*, 5251-5264.

[5] Bills, B. G., and R. S. Nerem (1995), A harmonic analysis of Martian topography, *J. Geophys. Res., 100*, 26317-26326.

[6] Boehler, R. (1992), Melting of the Fe-FeO and the Fe-FeS systems at high pressure, Constraints on core temperatures, *Earth Planet. Sci. Lett., 111*, 217-227.

[7] Boehler, R. (1996), Melting temperature of the Earth's mantle and core: Earth's thermal structure, *Annu. Rev. Earth Planet. Sci., 24*, 15-40.

[8] Boehler, R. (2000), High-pressure experiments and the phase diagram of lower mantle and core materials, *Rev. Geophys., 38*, 221-245.

[9] Breuer, D., and T. Spohn (2003), Early plate tectonics versus single-plate tectonics on Mars: Evidence from magnetic field history and crust evolution, *J. Geophys. Res., 108*, DOI 10.1029/2002JE001999.

[10] Breuer, D., D. A. Yuen, T. Spohn, and S. Zhang (1998), Three dimensional models of Martian mantle convection with phase transitions, *Geophys. Res. Lett., 25*, 229-232.

[11] Campbell, I. H., R. Griffiths, and R. I. Hill (1990), Melting in the Archaean mantle plume: heads its basalts, tails its komatiites, *Nature, 339*, 697-699.

[12] Canright, D., and S. Morris (1993), Buoyant instability of a viscous film over a passive fluid, *J. Fluid Mech., 255*, 349-372.

[13] Canup, R. M. (2004), Simulations of a late lunar-forming impact, *Icarus, 168*, 433-456.

[14] Chopelas, A. (1996), Thermal expansivity of lower mantle phases MgO and $MgSiO_3$ perovskite at high pressure derived from vibrational spectroscopy, *Phys. Earth Planet. Inter., 98*, 3-15.

[15] Christensen, U. (1984), Instability of a hot boundary layer and initiation of thermo-chemical plumes, *Ann. Geophys., 2*, 311-320.

[16] Condie, K. C. (2004), Supercontinents and superplume events: distinguishing signals in the geologic record *Phys. Earth Planet. Inter., 146*, 319-332.

[17] Connerney, J. E. P., et al. (1999), Magnetic lineations in the ancient crust of Mars, *Science, 284*, 794-798.

[18] Connerney, J. E. P., et al. (2005), Tectonic implications of Mars crustal magnetism, *PNAS, 102*, 14970-14975.

[19] Connolly, J. A. D., and Y. Y. Podladchikov (2007), Decompaction weakening and channeling instability in ductile porous media: Implications for asthenospheric melt segregation, *J. Geophys. Res., 112*, doi:10.1029/2005JB004213.

[20] Davaille, A., and C. Jaupart (1993a), Transient high Rayleigh number thermal convection with large viscosity variations, *J. Fluid Mech., 253*, 141166.

[21] Davaille, A., and C. Jaupart (1993b), Thermal convection in lava lakes, *Geophys. Res. Lett., 20*, 18271830.

[22] Davies, G. F. (1982), Ultimate strength of solids and formation of planetary cores, *Geophys. Res. Lett., 9*, 1267-1270

[23] Dreibus, G., and H. Wänke (1985), Mars, a volatile-rich planet, *Meteoritics, 20*, 367-381.

[24] Elkins-Tanton, L. T., E. M. Parmentier, and P. C. Hess (2003), Magma ocean fractional crystallization and cumulate overturn in terrestrial planets: Implications for Mars, *Meteorit. Planet. Sci., 38*, 1753-1771.

[25] Elkins-Tanton, L. T., P. C. Hess, and E. M. Parmentier (2005a), Possible formation of ancient crust on Mars through magma ocean processes, *J. Geoph. Res., 110*, doi:10.1029/2005JE002480.

[26] Elkins-Tanton, L. T., S. E. Zaranek, E. M. Parmentier, P. C. Hess (2005b), Early magnetic field and magmatic activity on Mars from magma ocean cumulate overturn, *Earth Planet. Sci. Lett., 236*, 1-12.

[27] Elsasser, W. M. (1963), Early history of the Earth; dedicated to F. G. Houtermans on his sixtieth birthday, in: J. Geiss and E. Goldberg (eds.) *Earth Science and Meteoritics*, North-Holland, Amsterdam, pp. 1-30.

[28] Ernst, R. E., K. L. Buchan, and D. W. Desnoyers (2007), Plumes and plume clusters on Earth and Venus: Evidence from Large Igneous Provinces (LIPs) in: D. A. Yuen et al. (eds.) *Superplumes: Beyond Plate Tectonics*, Springer Netherlands, pp. 537-562.

[29] Fei, Y., C. M. Bertka, and L. W. Finger (1997), High-pressure iron-sulfur compound, Fe_3S_2, and melting relations in the Fe-FeS system, *Science, 275*, 1621-1623.

[30] Fei, Y., and C. M. Bertka (2005), The interior of Mars, *Science, 308*, 1120-1121.

[31] Fowler, A. C. (1985), Fast thermoviscous convection, *Stud. Appl. Math.,* 72, 1-34.

[32] Frey, H. V. (2006), Impact constraints on, and a chronology for, major events in early Mars history, *J. Geophys. Res., 111*, E08S91, doi:10.1029/2005JE002449.

[33] Frey, H. V., and R. A. Schultz (1988), Large impact basins and the mega-impact origin for the crustal dichotomy on Mars, *Geophys. Res. Lett., 15*, 229-232.

[34] Frey, H. V., J. H. Roark, K. M. Shockey, E. L. Frey, and S. E. H. Sakimoto (2002), Ancient lowlands on Mars, *Geophys. Res. Lett., 29*(10), 1384, doi:10.1029/2001GL013832.

[35] Golabek, G. J., H. Schmeling, and P. J. Tackley (2008), Earth's core formation aided by flow channelling instabilities induced by iron diapirs, *Earth Planet. Sci. Lett., 271*, 348-358.

[36] Griffiths, R. W. (1986), Thermals in extremely viscous fluids, including the effects of temperature-dependent viscosity, *J. Fluid Mech. 166*, 115-138.

[37] Hansen, U., D. Yuen and S. E. Kroening (1990), Transition to hard turbulence in thermal convection at infinite Prandtl number, *Phys. Fluids A, 2*, 2157-2163.

[38] Harder, H. (1998), Phase transitions and the three-dimensional platform of thermal convection in the Martian mantle, *J. Geophys. Res., 103*, 16775-16797.

[39] Harder, H. (2000), Mantle convection and the dynamic geoid of Mars, *Geophys. Res. Lett., 27*, 301-304.

[40] Harder, H., and U. R. Christensen (1996), A one-plume model of Martian mantle convection, *Nature, 380*, 507-509.

[41] Hartmann, W. K., and G. Neukum (2001), Cratering chronology and the evolution of Mars, *Space Sci. Rev., 96*, 165-194.

[42] Hofmeister, A. M. (1999), Mantle values of thermal conductivity and the geotherm for phonon lifetimes, *Science, 283*, 1699-1706.

[43] Holland, K. G., and T. J. Ahrens (1997), Melting of Mg,Fe $_2$SiO$_4$ at the core-mantle boundary of the Earth, *Science, 275*, 1623-1625.

[44] Honda, R., H. Mizutani, and T. Yamamoto (1993), Numerical simulations of Earth's core formation, *J. Geophys. Res., 98*, 2075-2089.

[45] Ida, S. Y., Y. Nakagawa, and K. Nakazawa (1987), The Earth's core formation due to Rayleigh-Taylor instability, *Icarus, 69*, 239-248.

[46] Karato, S.-I., and P. Wu (1993), Rheology of the upper mantle: A synthesis, *Science, 260*, 771-778.

[47] Kaula, W. M. (1979), Thermal evolution of Earth and Moon growing by planetesimal impacts, *J. Geophys. Res., 84*, 999-1008.

[48] Ke, Y., and V. S. Solomatov (2004), Plume formation in strongly temperature-dependent viscosity fluids over a very hot surface, *Phys. Fluids, 16*, 1059-1063.

[49] Ke, Y., and V. S. Solomatov (2006), Early transient superplumes and the origin of the Martian crustal dichotomy, *J. Geophys. Res., 111*, DOI 10.1029/2005JE002631.

[50] Ke, Y., and V. S. Solomatov (2009), Coupled core-mantle thermal evolution of early Mars, *J. Geophys. Res.*, DOI 10.1029/2008JE003291, in press.

[51] Kellogg, L. H., and S. D. King (1997), The effects of temperature dependent viscosity on the structure of new plumes in the mantle: Results of a finite element model in a spherical, axisymmetric shell, *Earth Planet. Sci. Lett., 148*, 13-26.

[52] Khan, A., and J. A. D. Connolly (2008), Constraining the composition and thermal state of Mars from inversion of geophysical data, *J. Geophys. Res., 113*, E07003, doi:10.1029/2007JE002996.

[53] Kleine, T., K. Mezger, H. Palme, and C. Muenker (2004), The W isotope evolution of the bulk silicate Earth; constraints on the timing and mechanisms of core formation and accretion, *Earth Planet. Sci. Lett., 228*, 109-123.

[54] Kraichnan, R. H. (1962), Turbulent thermal convection at arbitrary Prandtl number, *Phys. Fluids, 5*, 1374-1389.

[55] Labrosse, S., J. W. Hernlund, and N. Coltice (2007), A crystallizing dense magma ocean at the base of the Earths mantle, *Nature, 450*, 866-869.

[56] Landau, L. D., and E. M. Lifshitz (1987), *Fluid Mechanics*, Pergamon Press.

[57] Lemoine, F. G., and others (2001), An improved solution of the gravity field of Mars (GMM-2B) from Mars Global Surveyor, *J. Geophys. Res., 106*, 23359-23376.

[58] Lenardic, A., F. Nimmo, and L. Moresi (2004), Growth of the hemispheric dichotomy and the cessation of plate tectonics on Mars, *J. Geophys. Res., 109*, doi:10.1029/2003JE002172.

[59] Liebske, C., B. Schmickler, H. Terasaki, B. T. Poe, A. Suzuki, K.-I. Funakoshi, R. Ando, and D. C. Rubie (2005), Viscosity of peridotite liquid up to 13 GPa: Implications for magma ocean viscosities, *Earth Planet. Sci. Lett., 240*, 589-604.

[60] Lillis, R. J., H. V. Frey, M. Manga, D. L. Mitchell, R. P. Lin, and M. H. Acuna, (2006), Bracketing the end of the martian dynamo: the ages and magnetic signatures of Hellas and Ladon basins, *Lunar Planet. Sci. XXXVII*, abstract 2183.

[61] Lillis, R. J., H. V. Frey, M. Manga, D. L. Mitchell, R. P. Lin, and M. H. Acuna, (2007a), Basin magnetic signatures and crater retention ages: Evidence for a rapid shutdown of the martian dynamo, *Lunar Planet. Sci. XXXVIII*, abstract 1515.

[62] Lillis, R. J., H. V. Frey, M. Manga, D. L. Mitchell, R. P. Lin, and M. H. Acuna, (2007b), Magnetic signatures and crater retention ages of giant buried basins on Mars; new constraints on the timing of the ancient dynamo, *Seventh Int. Conf. on Mars,* abstract 3090.

[63] Lithgow-Bertelloni, C., M. A. Richards, C. P. Conrad, and R. W. Griffiths (2001), Plume generation in natural thermal convection at high Rayleigh and Prandtl numbers, *J. Fluid Mech., 434*, 1-21.

[64] Longhi, J., E. Knittle, J. R. Holloway, and H. Wanke (1992), The bulk composition, mineralogy and internal structure of Mars, in *Mars*, edited by H. H. Kieffer, B. M. Jakovsky, C. W. Snyder, and M. S. Matthews, pp. 184-208, Univ. of Ariz. Press, Tucson.

[65] Loper, D. E. (1998), Mantle plumes and their effect on the Earth's surface: a review and synthesis, *Dyn. Atm. Oceans, 27*, 35-54.

[66] Loper, D. E., and F. D. Stacey (1983), The dynamical and thermal structure of deep mantle plumes, *Phys. Earth Planet. Inter., 33*, 304-317.

[67] Manga, M. and D. Weeraratne (1999), Experimental study of non-Boussinesq Rayleigh-Benard convection at high Rayleigh and Prandtl numbers, *Phys. Fluids, 11*, 2969-2976.

[68] Manga, M., D. Weeraratne, and S. J. S. Morris (2001), Boundary-layer thickness and instabilities in Benard convection, *Phys. Fluids, 13*, 802-805.

[69] Marinova, M. M., O. Aharonson, and E. Asphaug (2008), Mega-impact formation of the Mars hemispheric dichotomy, *Nature, 453*, 1216-1219.

[70] McGill, G. E., and A. M. Dimitriou (1990), Origin of the Martian global dichotomy by crustal thinning in the late Noachian or early Hesperian, *J. Geophys. Res., 95*, 12595-12605.

[71] McGovern P. J., S. C. Solomon, D. E. Smith, M. T. Zuber, M. Simons, M. A. Wieczorek, R. J. Phillips, G. A. Neumann, O. Aharonson, and J. W. Head

(2002), Localized gravity/topography admittance and correlation spectra on Mars: Implications for regional and global evolution, *J. Geophys. Res., 107*, E12, 5136, doi:10.1029/2002JE001854.

[72] McKenzie, D., D. N. Barnett, and D.-N. Yuan (2002), The relationship between Martian gravity and topography, *Earth Planet. Sci. Lett., 195*, 1-16.

[73] McLennan, S. M. (2001), Crustal heat production and the thermal evolution of Mars, *Geophys. Res. Lett., 28*, 4019-4022.

[74] Moresi, L.-N., and V. S. Solomatov (1995), Numerical investigation of 2D convection with extremely large viscosity variations, *Phys. Fluids, 7*, 2154-2162.

[75] Morgan, W. J. (1971), Convection plumes in the lower mantle, *Nature, 230*, 42-43.

[76] Morris, S., and D. Canright (1984), A boundary layer analysis of Bénard convection in a fluid of strongly temperature dependent viscosity, *Phys. Earth Planet. Inter., 36*, 355-373.

[77] Mostefaoui, S., G. W. Lugmair, and P. Hoppe (2005), Fe-60: A heat source for planetary differentiation from a nearby supernova explosion, *Astrophys. J., 625*, 271-277.

[78] Mound, J., and B. Buffett (2007), Viscosity of the Earth's fluid core and torsional oscillations, *J. Geophys. Res., 112*, doi:10.1029/2006JB004426.

[79] Nimmo, F., and D. J. Stevenson (2000), Influence of early plate tectonics on the thermal evolution and magnetic field of Mars, *J. Geophys. Res., 105*, 11969-11979.

[80] Nimmo, F., and D. J. Stevenson (2001), Estimates of Martian crustal thickness from viscous relaxation of topography, *J. Geophys. Res., 106*, 5085-5098.

[81] Olson, P., G. Schubert, and C. Anderson (1987), Plume formation in the D”-layer and the roughness of the core-mantle boundary, *Nature*, *327*, 409-413.

[82] Poirier, J.-P. (1994) Light elements in the Earth’s outer core: A critical review, *Phys. Earth Planet. Inter., 85*, 319-337.

[83] Reese, C. C., and V. S. Solomatov (2006), Fluid dynamics of local martian magma oceans, *Icarus, 184*, 102-120.

[84] Reese, C. C., V. S. Solomatov, and J. R. Baumgardner (2005), Scaling laws for time-dependent stagnant lid convection in a spherical shell, *Phys. Earth Planet. Inter., 149*, 361-370.

[85] Renne, P. R., Z. C. Zhang, M. A. Richards, M. T. Black, and A. R. Basu (1995), Synchrony and causal relations between Permian-Triassic boundary crises and Siberian flood volcanism, *Science 269*, 1413-1416.

[86] Ribe, N. M., and D. P. de Valpine (1994), The global hotspot distribution and instability of D”, *Geophys. Res. Lett., 21*, 1507-1510.

[87] Richards, M. A., R. A. Duncan, and V. E. Courtillot (1989), Flood basalts and hot-spot tracks-plume heads and tails, *Science, 246*, 103-107.

[88] Righter, K. (2003), Metal-silicate partitioning of siderophile elements and core formation in the early Earth, *Ann. Rev. Earth Planet. Sci., 31*, 135-174.

[89] Roberts, J. H. ,and S. Zhong (2006), Degree-1 convection in the Martian mantle

and the origin of the hemispheric dichotomy, *J. Geophys. Res., 111*, E06013, doi:10.1029/2005JE002668.

[90] Roberts, J. H., and S. Zhong (2007), The cause for the north-south orientation of the crustal dichotomy and the equatorial location of Tharsis on Mars, *Icarus. 190*, 24-31, doi:10.1016/j.icarus.2007.03.002.

[91] Roscoe, R. (1952), The viscosity of suspensions of rigid spheres. *Br. J. Appl. Phys., 3*, 267-269.

[92] Schaeffer, N., and M. Manga (2001), Interaction of rising and sinking mantle plumes, *Geophys. Res. Lett., 28*, 455-458.

[93] Schubert, G., D. Bercovici, and G. A. Glatzmaier (1990), Mantle dynamics in Mars and Venus - Influence on an immobile lithosphere on 3-Dimensional mantle convection, *J. Geophys. Res., 95*, 14105-14129.

[94] Schubert, G., S. C. Solomon, D. L. Turcotte, M. J. Drake, and N. H. Sleep (1992), Origin and thermal evolution of Mars, in *Mars*, edited by H. H. Kieffer, B. M. Jakovsky, C. W. Snyder, and M. S. Matthews, pp. 147-183.

[95] Schubert, G., D. L. Turcotte, and P. Olson (2001), *Mantle convection in the Earth and planets*, Cambridge Univ. Press, New York, 940 pp.

[96] Scott, T. J., and D. L. Kohlstedt (2004), The effect of large melt fraction on the deformation behavior of peridotite: Implications for the viscosity of IO's mantle and the rheologically critical melt fraction, *Eos Trans. AGU 85*, Abstract 4582.

[97] Senshu, H., K. Kuramoto, T. Matsui (2002), Thermal evolution of a growing Mars, *J. Geophys. Res., 107*, doi:10.1029/2001JE001819.

[98] Shukolyukov, A., and G. W. Lugmair (1993), Live iron-60 in the early Solar System, *Science, 259*, 1138-1142.

[99] Siggia, E. D. (1994), High Rayleigh number convection, *Annu. Rev. Fluid Mech., 26,* 137-168.

[100] Sleep, N. H. (1994), Martian plate tectonics, *J. Geophys. Res., 99*, 5639-5655.

[101] Smith, D. E., M. T. Zuber, S. C. Solomon, R. J. Phillips, J. W. Head, J. B. Garvin, W. B. Banerdt, D. O. Muhleman, G. H. Pettengill, G. A. Neumann, F. G. Lemoine, J. B. Abshire, O. Aharonson, C. D. Brown, S. A. Hauck, A. B. Ivanov, P. J. McGovern, H. J. Zwally, and T. C. Duxbury (1999), The global topography of Mars and implications for surface evolution, *Science, 284*, 1495-1503.

[102] Smith, D. E., and others (2001), Mars Orbiter Laser Altimeter: Experiment summary after the first year of global mapping of Mars, *J. Geophys. Res., 106*, 23689-23722.

[103] Solomatov, V. S. (1995), Scaling of temperature- and stress-dependent viscosity convection, *Phys. Fluids, 7*, 266-274.

[104] Solomatov, V. S. (2000), Fluid dynamics of a terrestrial magma ocean, in *Origin of the Earth and Moon*, eds. R. Canup and K. Righter, University of Arizona Press, Tucson, Arizona, pp. 323-338.

[105] Solomatov, V. S., and A. C. Barr (2006), Onset of convection in fluids with strongly temperature-dependent, power-law viscosity, *Phys. Earth Planet. Inter., 155*, 140-145.

[106] Solomatov, V. S., and L.-N. Moresi (2000), Scaling of time-dependent stagnant lid convection: Application to small-scale convection on the Earth and other terrestrial planets, *J. Geophys. Res., 105*, 21795-21818.

[107] Solomatov, V. S., and L.-N. Moresi (2002), Small-scale convection in the D" layer, *J. Geophys. Res., 107*, doi:10.1029/2000JB000063.

[108] Solomatov, V. S. (2007), Magma oceans and primordial mantle differentiation, in *Treatise on Geophysics*, ed. G. Schubert, Elsevier, v. 9, pp. 91-120.

[109] Solomatov, V. S., and D. J. Stevenson (1993a), Nonfractional crystallization of a terrestrial magma ocean, *J. Geophys. Res., 98*, 5391-5406.

[110] Solomatov, V. S., and D. J. Stevenson (1993b), Kinetics of crystal growth in a terrestrial magma ocean, *J. Geophys. Res., 98*, 5407-5418.

[111] Solomon, S. (1979), Formation, history and energetics of cores in the terrestrial planets, *Phys. Earth Planet. Inter., 19*, 168-182.

[112] Solomon, S. C. , and others (2005), New perspectives on ancient Mars, *Science 25*, 1214-1220.

[113] Spohn, T. S., F. Sohl, and D. Breuer (1998), Mars, *The Astron Astrophys Rev. 8*, 181-236.

[114] Srinivasan, G., J. N. Goswami, and N. Bhandari (1999), ^{26}Al in eucrite Piplia Kalan: Plausible heat source and formation chronology, *Science, 284*, 1348-1350

[115] Stengel, K. C., D. C. Oliver, and J. R. Booker (1982), Onset of convection in a variable viscosity fluid, *J. Fluid. Mech., 120*, 411-431.

[116] Stevenson, D. J. (1981), Models of the Earth's core, *Science, 214*, 611-619.

[117] Stevenson, D. J. (1990), Fluid dynamics of core formation, in: N. E. Newsom, and J. H. Jones (eds.) *Origin of the Earth*, Oxford University Press, New York, pp. 231-249.

[118] Stevenson, D. J. (2001), Mars' core and magnetism, *Nature, 412*, 214-219.

[119] Stevenson, D. J., T. Spohn, and G. Schubert (1983), Magnetism and thermal evolution of the terrestrial planets, *Icarus, 54*, 466-489.

[120] Taylor, G. J., and others (2007), Bulk composition and early differentiation of Mars, *J. Geophys. Res., 111*, E03S10, doi:10.1029/2005JE002645.

[121] Thompson, P. E., and P. J. Tackley (1998), Generation of mega-plumes from the core-mantle boundary in a compressible mantle with temperature-dependent viscosity, *Geophys. Res. Lett., 25*, 1999-2002.

[122] Tonks, W. B., and H. J. Melosh (1992), Core formation by giant impacts, *Icarus, 100,* 326-346.

[123] Trompert, R. A., and U. Hansen (1998), On the Rayleigh number dependence of convection with a strongly temperature-dependent viscosity, *Phys. Fluids, 10*, 351-360.

[124] Turcotte, D. L., and G. Schubert (2002), Geodynamics, Cambridge Univ., New York, 456 pp.

[125] Urey, H. C. (1955), The cosmic abundances of potassium, uranium, and thorium and the heat balances of the Earth, the Moon, and Mars, *Natl Acad. Sci. USA, 41*, 127144.

[126] van Keken, P. E. (1997), Evolution of starting mantle plumes – A comparison between numerical and laboratory models, *Earth Planet. Sci. Lett., 148*, 1-11.

[127] Weinberg, R. F. (1997), Rise of starting plumes through mantle of temperature-, pressure-, and stress-dependent viscosity, *J. Geophys. Res., 102*, 7613-7623.

[128] Wenzel, M. J., M. Manga, and A.M. Jellinek (2004), Tharsis: A consequence of Mars' dichotomy and layered mantle, *Geophys. Res. Lett., 31*, doi:10.1029/2003GL019306.

[129] Whitehead, J. A., and D. S. Luther (1975), Dynamics of laboratory diapir and plume models, *J. Geophys. Res., 80*, 705-717.

[130] Wieczorek, M. A., and M. T. Zuber (2004), Thickness of the Martian crust: Improved constraints from geoid-to-topography ratios, *J. Geophys. Res., 109*, E01009, doi:10.1029/2003JE002153.

[131] Wiggins, C., and M. Spiegelman (1995), Magma migration and magmatic solitary waves in 3-D, *Geophys. Res. Lett., 22*, 1289-1292.

[132] Wilhelms, D. E., and S. W. Squyres (1984), The Martian hemispheric dichotomy may be due to a giant impact, *Nature, 309*, 138-140.

[133] Williams, J-P. and F. Nimmo (2004), Thermal evolution of the Martian core; implications for an early dynamo, *Geology, 37*, 97-100.

[134] Williams, Q. (1998), The temperature contrast across D", in *The Core-Mantle Boundary Region, Geodyn. Ser.,* Vol. 28, edited by M. Gurnis et al., pp. 73-81, AGU, Washington, D. C.

[135] Wise, D. U., M. P. Golombek, and G. E. McGill (1979), Tectonic evolution of Mars, *J. Geophys. Res., 84*, B14, 7934-7939.

[136] Yamazaki, D. and S.-I. Karato (2001), Some mineral physics constraints on the rheology and geothermal structure of Earth's lower mantle, *Am. Mineral. 86*, 385-391.

[137] Yoder, C. F., A. S. Konopliv, D. N. Yuan, E. M. Standish, and W. M. Folkner (2003), Fluid core size of Mars from detection of the solar tide, *Science, 300*, 299-303.

[138] Yoshino, T., M. J. Walter, and T. Katsura (2003), Core formation in planetesimals triggered by permeable flow, *Nature 422*, 154-157

[139] Yuan, D. N., W. L. Sjogren, A. S. Konopliv, and A. B. Kucinskas (2001), Gravity field of Mars: A 75th degree and order model, *J. Geophys. Res., 106*, 23377-23401.

[140] Yuen, D. A., and W. R. Peltier (1980), Mantle plumes and the thermal stability of the D" layer, *Geophys. Res. Lett., 7*, 625-628.

[141] Zerr, A., A. Diegeler, and R. Boehler (1998), Solidus of Earth's deep mantle, *Science, 281,* 243-246.

[142] Zhang, J., and C. Herzberg (1994), Melting experiments on anhydrous peridotite KLB-1 from 5.0 to 22.5 GPa, *J. Geophys. Res., 99(B9)*, 17729-17742.

[143] Zharkov, V. N., *Interior structure of the earth and planets*, Harwood, New York, 1986.

[144] Zharkov, V. N., and T. V. Godkova (2000), Interior structure models, Fe/Si ratio and parameters of figure for Mars, *Phys. Earth Planet. Inter., 117*, 407-420.

[145] Zhong, S., and M. T. Zuber (2001), Degree-1 mantle convection and the crustal dichotomy on Mars, *Earth Planet. Sci. Lett., 189*, 75-84.

[146] Zhong, S., M. T. Zuber, L. N. Moresi, and M. Gurnis (2000), The role of temperature-dependent viscosity and surface plates in spherical shell models of mantle convection, *J. Geophys. Res., 105*, 11063-11082.

[147] Zuber, M. T., S. C. Solomon, R. J. Phillips, D. E. Smith, G. L. Tyler, O. Aharonson, G. Balmino, W. B. Banerdt, J. W. Head, C. L. Johnson, F. G. Lemoine, P. J. McGovern, G. A. Neumann, D. D. Rowlands, S. Zhong (2000), Internal structure and early thermal evolution of Mars from Mars Global Surveyor topography and gravity, *Science, 287*, 1788-1793.